

# JOURNAL OF TELECOMMUNICATIONS AND INFORMATION TECHNOLOGY

1/2021

## Studying and Modeling the Performance of the TCM-STBC Systems in the Rayleigh Channel

*M. S. Bendelhoum, M. R. Lahcene, F. Menezla, and A. Elarbi*

*Paper*

1

## High-resolution Direction of Arrival Estimation Method Based on Sparse Arrays with Minimum Number of Elements

*J. R. Mohammed*

*Paper*

8

## Location Estimation of Nodes in Underwater Acoustic Sensor Networks

*B. S. Halakarnimath and A. V. Sutagundar*

*Paper*

15

## Suboptimal Approach to Distributed Detection in Cognitive Radio Networks

*S. Kumari and S. Praveena*

*Paper*

32

## Evaluation of Reliability of Mobile ICT Services

*M. Kowalewski, R. Kobus, and T. Sędek*

*Paper*

37

## Optimal Voting Rule and Minimization of Total Error Rate in Cooperative Spectrum Sensing for Cognitive Radio Networks

*S. K. Ghosh, S. R. Trankatwar, and P. Bachan*

*Paper*

43

## FANET Drone's 4K Data Applications, Mobility Models and Wi-Fi IEEE802.11n Standards

*G. A. QasMarrogy*

*Paper*

51

## Artificial Magnetic Conductor-based Millimeter Wave Microstrip Patch Antenna for Gain Enhancement

*K. Belabbas, D. Khedrouche, and A. Hocini*

*Paper*

56

*(Contents Continued on Back Cover)*

## ***Editor-in-Chief***

**Adrian Kliks**, *Poznan University of Technology, Poland*

## ***Steering Editor***

**Jordi Mongay Batalla**, *National Institute of Telecommunications, Poland*

## ***Editorial Advisory Board***

**Hovik Baghdasaryan**, *National Polytechnic University of Armenia, Armenia*

**Naveen Chilamkurti**, *LaTrobe University, Australia*

**Luis M. Correia**, *Instituto Superior Técnico, Universidade de Lisboa, Portugal*

**Luca De Nardis**, *DIET Department, University of Rome La Sapienza, Italy*

**Nikolaos Dimitriou**, *NCSR "Demokritos", Greece*

**Ciprian Dobre**, *Politechnic University of Bucharest, Romania*

**Filip Idzikowski**, *Poznan University of Technology, Poland*

**Andrzej Jajszczyk**, *AGH University of Science and Technology, Poland*

**Albert Levi**, *Sabancı University, Turkey*

**Marian Marciniak**, *National Institute of Telecommunications, Poland*

**George Mastorakis**, *Technological Educational Institute of Crete, Greece*

**Constandinos Mavromoustakis**, *University of Nicosia, Cyprus*

**Klaus Mößner**, *Technische Universität Chemnitz, Germany*

**Imran Muhammad**, *King Saud University, Saudi Arabia*

**Mjumo Mzyece**, *University of the Witwatersrand, South Africa*

**Daniel Negru**, *University of Bordeaux, France*

**Ewa Orłowska**, *National Institute of Telecommunications, Poland*

**Jordi Perez-Romero**, *UPC, Spain*

**Michał Pióro**, *Warsaw University of Technology, Poland*

**Konstantinos Psannis**, *University of Macedonia, Greece*

**Salvatore Signorello**, *University of Lisboa, Portugal*

**Adam Wolisz**, *Technische Universität Berlin, Germany*

**Tadeusz A. Wysocki**, *University of Nebraska, USA*

## ***Publications Staff***

Content Editor: **Robert Magdziak**

Managing Editor: **Ewa Kapuściarek**

Technical Editor: **Grażyna Woźnica**

ISSN 1509-4553      on-line: ISSN 1899-8852

© Copyright by National Institute of Telecommunications, Warsaw 2021



# Studying and Modeling the Performance of the TCM-STBC Systems in the Rayleigh Channel

Mohammed Sofiane Bendelhoum<sup>1,2</sup>, Mohamed Rida Lahcene<sup>3,4</sup>, Fayssal Menezla<sup>2,5</sup>,  
and Abderraouf Elarbi<sup>3</sup>

<sup>1</sup> Instrumentation Laboratory and Advanced Materials (ILAM), University Center Nour Bachir of El-Bayadh, Algeria

<sup>2</sup> Department of Electrical Engineering, University Center Nour Bachir of El-Bayadh, Algeria

<sup>3</sup> Information Processing and Telecommunication Laboratory (LTIT), Tahri Mohammed Bechar University, Algeria

<sup>4</sup> Department of Technology, University Center Salhi Ahmed of Naama, Algeria

<sup>5</sup> Laboratory (LEPO), Djillali Liabes University, Sidi Bel-Abbes, Algeria

<https://doi.org/10.26636/jtit.2021.147020>

**Abstract**— Multiple-input multiple-output (MIMO) systems will play an important role in future generations of wireless networks. Space-time block code (STBC) and space-time trellis code (STTC) are two techniques that may be used in multi-antenna radio systems. This paper aims, most importantly, to study the performance of STBC systems at different values of such parameters as spectral efficiency, matrix codes and constellations. A performance comparison between STBC and STTC schemes is performed. In order to show the efficiency of the system's ability to communicate with uncoded and coded transmission structures over AWGN and Rayleigh channels, the trellis-coded modulation (TCM) is introduced. The results obtained show that the proposed TCM-STBC system model, using one and two receiving antennas, improves the performance of Rayleigh channel communication systems at 9.5 dB and 11.5 dB for a BER of  $10^{-5}$ .

**Keywords**—BER, MIMO, SNR, STBC, STTC, TCM, TCM-STBC.

## 1. Introduction

The major challenge faced by advanced communications and wireless multimedia technologies consists in achieving high performance levels with reliable communication and flexible data rates. Such outcomes are offered within a limited spectrum of bandwidths and energy consumptions rates. The MIMO technology improves spectrum efficiency and boosts channel capacity. The space-time coding (STC) technique introduces space redundancy, thanks to the addition of multiple antennas, and time redundancy thanks to channel coding. To achieve this, two prevailing space-time coding techniques are used, namely Space time block codes (STBC) and space time trellis codes (STTC). The STBC approach offers diversity gains with very low decoding complexity levels, while STTC provides both diversity and coding gains at the cost of higher decoding complexity [1].

Trellis coded modulation (TCM) is a bandwidth-efficient transmission scheme that may achieve high encoding gains

by integrating encoding and modulation. A more efficient approach consists in designing trellis encoded modulation solutions in long sequences of messages [2], [3]. The permitted sequences should differ considerably from each other. The receiver may then make a decision concerning the sequences based on statistical analysis, rather than by relying on the symbol-by-symbol based computation decoding method [2].

In the literature, various studies describe the performance of such systems relying on space time coding (STC) [4], [5], STBC [6], STTC [7] and TCM [8] techniques. Other studies focused on combining STBC and STTC [9] with different systems, such as MC-CDMA [10] or OFDM [11]. In [4], a new generalized concatenated signal code construction whose inner codes are golden codes and outer codes are products of Reed-Solomon codes is proposed.

In [6], the authors proposed a new approach to decode STBC-MIMO using the Kurtosis-based blind source separation (BSS) algorithm under a quasistatic flat fading channel. The performance of a space time trellis code-based solution with the beamforming concept and relying on various modulation techniques is analyzed in [7]. Hashem Ali Khan *et al.* [8] analyzed signal constellations based on orthogonal space-time codes (OSTCs), which are theoretically suited for MIMO systems. BER performance of STBC and STTC in the MIMO satellite channel is studied by Jing and Wu [9]. In [10], balanced STTC (B-STTC)-based STBC site diversity is proposed to improve the performance of MC-CDMA systems by mitigating multi-cell interference and is extended to the STBC-based B-STTC site diversity technique. STBC-OFDM techniques are studied in [11] for wireless channels using BPSK modulation and maximum likelihood detection for two transmit and two receive antennas.

Our contribution consists in proposing a combination of two systems: trellis coded modulation (TCM) and the space-time block code (STBC) for improving performance

of transmission. The remaining part of the paper is organized as follows.

In Section 2, space time block coding is introduced. Section 3 presents a comparison between STBC and STTC schemes. Section 4 describes performance of communication with uncoded and coded transmission systems, using the TCM structure. Section 5 discusses the results of simulations of the proposed scheme, using TCM code modulation concatenated with the STBC. Finally, the paper concludes by presenting certain insights into the prospects concerning our present work.

## 2. Space Time Block Coding

STBC stipulates that each block is coded using predetermined rules, independently of the other blocks. A decoding error occurring in one block does not affect other blocks. This space-time diversity method has been proposed by Alamouti [12] using transmit and receive antennas. This method was then generalized by Tarokhet for  $n$  transmit antennas and  $m$  receive antennas in [13], [14]. Figure 1 illustrates the communication system of the original Alamouti STBC solution using two transmit and two receive antennas. The idea is to send a block of symbols via several transmit antennas. The symbols sent during the duration of a block via all the antennas are orthogonal. Real or complex symbols may be used for the transmission. The transmit and receive antennas are positioned in such a way that there is no correlation between them. The channels between each pair of transmit and receive antennas are independent and uncorrelated under these conditions. Due to the orthogonality of symbols, it is possible to use a simple linear recombination algorithm at the reception side to recover the symbols transmitted by all the antennas.

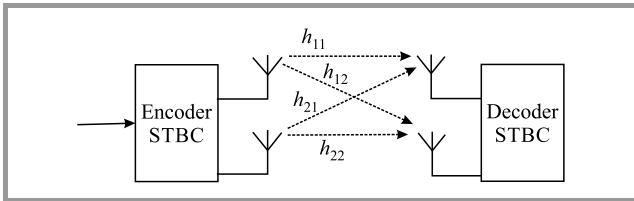


Fig. 1. Alamouti's STBC communication system.

Information symbols will be processed in pairs while generating four other symbols, two per each antenna [12]. Two signals are transmitted simultaneously from both antennas at time  $t$ . The signal transmitted by antenna one is defined by  $x_0$  and the one transmitted by antenna two is defined

by  $x_1$ . At time  $t + T$ , the signal  $(-x_1^*)$  is transmitted by antenna one and signal  $x_0^*$  is transmitted by antenna two, according to Table 1.

At time  $t$ , the signal received at antenna  $j$  is given by:

$$r_t^j = \sum_{i=1}^2 h_{ij} x_t^i + n_t^j. \quad (1)$$

The diversity matrixes  $G_M$  and  $H_M$ , are given by [12], [15]:

$$G_2 = \begin{bmatrix} x_1 & -x_2^* \\ x_2 & x_1^* \end{bmatrix}, \quad (2)$$

$$G_3 = \begin{bmatrix} x_1 & -x_2 & -x_3 & -x_4 & x_1^* & -x_2^* & -x_3^* & -x_4^* \\ x_2 & x_1^* & x_4 & -x_3 & x_2^* & x_1^* & x_4^* & -x_3^* \\ x_3 & -x_4 & x_1 & x_2 & x_3^* & -x_4^* & x_1^* & x_2^* \end{bmatrix}^T, \quad (3)$$

$$G_4 = \begin{bmatrix} x_1 & -x_2 & -x_3 & -x_4 & x_1^* & -x_2^* & -x_3^* & -x_4^* \\ x_2 & x_1^* & x_4 & -x_3 & x_2^* & x_1^* & x_4^* & -x_3^* \\ x_3 & -x_4 & x_1 & x_2 & x_3^* & -x_4^* & x_1^* & x_2^* \\ x_4 & x_3 & -x_2 & x_1 & x_4^* & x_3^* & -x_2^* & x_1^* \end{bmatrix}^T, \quad (4)$$

$$H_4 = \begin{bmatrix} x_1 & -x_2^* & \frac{x_3^*}{\sqrt{2}} & \frac{x_4^*}{\sqrt{2}} \\ x_2 & x_1^* & \frac{x_3^*}{\sqrt{2}} & \frac{x_4^*}{\sqrt{2}} \\ \frac{x_3}{\sqrt{2}} & \frac{x_3}{\sqrt{2}} & \frac{-x_1 - x_1^* + x_2 - x_2^*}{2} & \frac{-x_1 - x_1^* + x_2 + x_2^*}{2} \\ \frac{x_3}{\sqrt{2}} & \frac{-x_3}{\sqrt{2}} & \frac{-x_1 - x_1^* + x_2 - x_2^*}{2} & \frac{-x_1 - x_1^* + x_2 + x_2^*}{2} \end{bmatrix}^T. \quad (5)$$

The maximum likelihood decoder chooses a pair of signals. For two transmit G2 codes (Alamouti), the technique for combining  $x_0$  and  $x_1$  is [12]:

$$\begin{cases} \tilde{x}_0 = \sum_{j=1}^m [r_1^j h_{1j}^* + (r_2^j)^* h_{2j}] \\ \tilde{x}_1 = \sum_{j=1}^m [r_1^j h_{2j}^* - (r_2^j)^* h_{1j}] \end{cases}. \quad (6)$$

For two receive antennas:

$$\begin{cases} \tilde{x}_0 = r_1^1 h_{11}^* + (r_2^1)^* h_{21} + r_1^2 h_{12}^* + (r_2^2)^* h_{22} \\ \tilde{x}_1 = r_1^1 h_{21}^* - (r_2^1)^* h_{11} + r_1^2 h_{22}^* - (r_2^2)^* h_{12} \end{cases}, \quad (7)$$

where  $h_{11}$ ,  $h_{12}$ ,  $h_{21}$  and  $h_{22}$  represent the corresponding complex time domain channel transfer factors.

Figure 2 shows simulation results obtained based on the STBC scheme at 1 bps, using one, two, three, and four transmitting antennas and one receiving antenna. The output signal power is transmitted in whole when using one antenna. Otherwise, it will be equally divided when using multiple antennas [15]. The transmission performed while using one, two transmitting antennas relies on a BPSK constellation, as well as on the G1 (SISO model) and code G2. For three and four transmit antennas, the constellation used is QPSK with codes G3 and G4, for a spectral efficiency of 1 bps. For a BER of  $10^{-5}$  a significant

Table 1

Transmission sequence for two antennas

Temps	Antenna 1	Antenna 2
$t$	$x_0$	$x_1$
$t + T$	$-x_1^*$	$x_0^*$

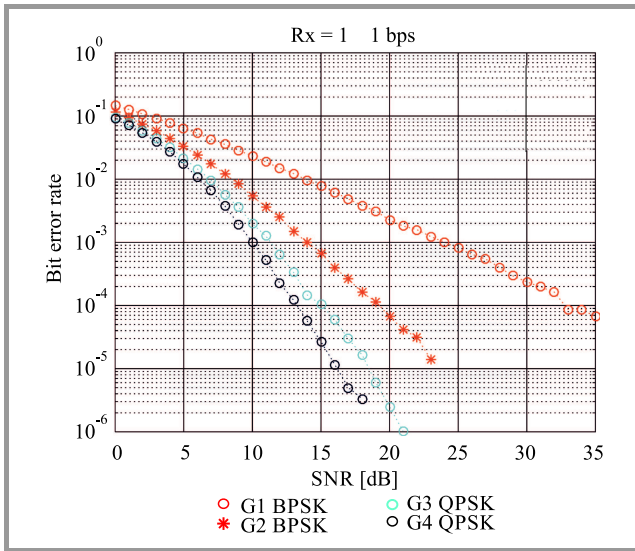


Fig. 2. BER versus SNR for different STBC codes for 1 bps with only one receiving antenna.

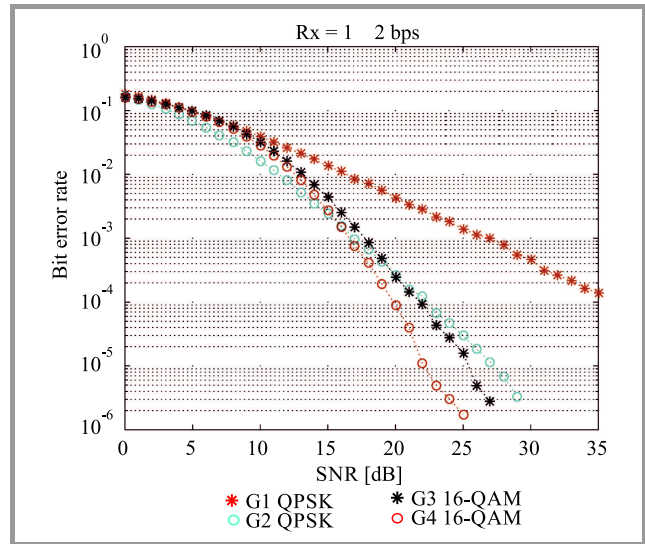


Fig. 4. BER versus SNR for different STBC codes for 2 bps with a single receiving antenna.

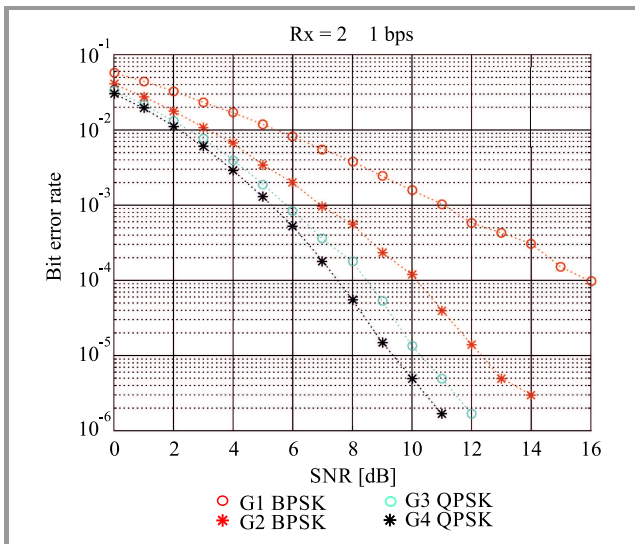


Fig. 3. BER versus SNR for different STBC codes for 1 bps with two receiving antennas.

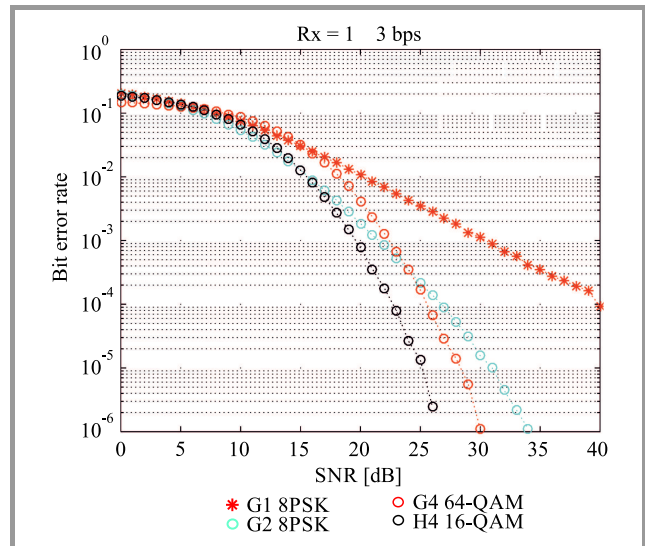


Fig. 5. BER versus SNR for different STBC codes for 3 bps with only one receiving antenna.

improvement in performance is observed, equaling approx. 7.5 dB for code G4, compared to code G2 for a single receiving antenna. If the number of receiving antennas is increased, this gain equals 3 dB, as shown in Fig. 3, with spectral efficiency amounting to 2 bps. In Fig. 3, the G1 variant is called SIMO.

Figure 4 depicts the simulation results obtained for 2 bps using one, two, three, and four transmit antennas. The transmission is performed using one, two transmit antennas with the QPSK constellation, as well as code G1 and G2. For three and four transmit antennas, the 16-QAM constellation is used with codes G3 and G4, respectively. It is obvious that code G4 offers a gain of approx. 5 dB, compared to code G2 for a BER of  $10^{-5}$  and one receiving antenna.

BER results versus SNR for 3 bps are shown in Fig. 5. For the 8-PSK modulation, codes G1 and G2 are used. Code G4 is used for the 64-QAM modulation. The 16-QAM modulation is used with code H4. Figure 4 clearly illustrates that the use of spatial diversity improves performance of the transmission system. Thus, there is an improvement of about 6 dB using code H4, compared to code G2 for BER of  $10^{-5}$  for one receiving antenna.

### 3. Space Time Trellis Codes

STTCs combine modulation and trellis coding for transmissions across multiple transmit antennas [16], [17]. The number of antennas may be increased without much complexity. Two symbols are simultaneously emitted from

these two antennas for each path in the trellis accordingly. Indices corresponding to the emitted symbols are represented in front of each line, indicating the state in the elementary lattice. These indices are ordered from left to right, considering the disposition of the segments, clockwise for each state. The number of the grouped indices is equal to the number of antennas.

The space time trellis encoder transmits symbols  $x_{k,1}$  and  $x_{k,2}$  over two transmitter antennas  $T_{x1}$  and  $T_{x2}$ . For each instant  $k$ , in a 4-state scenario with 4PSK constellation, the output symbols are given by [15], [17]:

$$x_{k,1} = 0.d_{k,1} + 0.d_{k,2} + 1.d_{k-1,1} + 2.d_{k-1,2}, \quad (8)$$

$$x_{k,2} = 1.d_{k,1} + 2.d_{k,2} + 0.d_{k-1,1} + 0.d_{k-1,2}, \quad (9)$$

where  $d_{k,i}$  represents current input bits and  $d_{k-1,i}$  represents previous input bits and  $i = 1, 2$ .

For each transmission time, the space time trellis decoder uses two 4-state receiver antennas with 4PSK. Symbols  $x_1$  and  $x_2$  are transmitted by antennas  $T_{x1}$  and  $T_{x2}$ . At the reception antennas  $R_{x1}$  and  $R_{x2}$ , we have:

$$y_1 = h_{11}x_1 + h_{12}x_2 + n_1, \quad (10)$$

$$y_2 = h_{21}x_1 + h_{22}x_2 + n_2. \quad (11)$$

The corresponding complex time-domain channel transfer factors are represented by  $h_{11}$ ,  $h_{12}$ ,  $h_{21}$  and  $h_{22}$ . The  $n_1$  and  $n_2$  are independent complex valued AWGNs having a zero mean and a power spectral density of  $N_0/2$  per dimension at time  $k$  and  $k + 1$ , respectively.

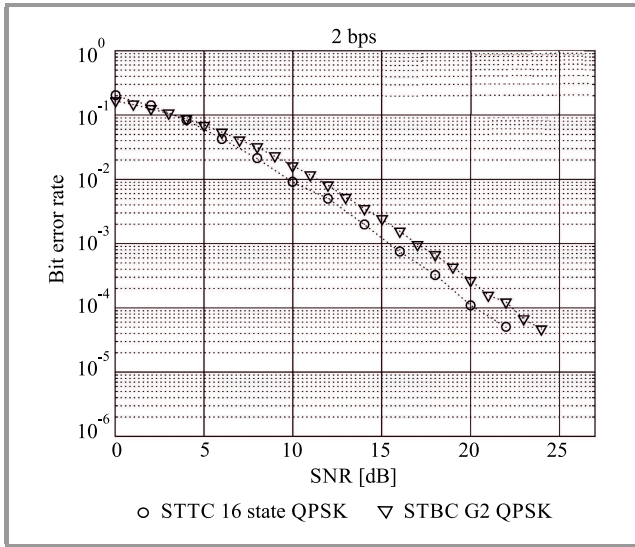


Fig. 6. BER versus SNR for 2 bps with one receiving antenna.

Figure 6 illustrates a comparison between STBC and STTC schemes for 2 bps, using one receive antenna. In STBC (code G2) and STTC (16-state codes), we use two transmit antennas with the QPSK constellation. The output signal power is transmitted fully when using one antenna. Otherwise, it will be equally divided when using multiple antennas.

Figure 6 clearly depicts that space-time trellis codes generate better results than the block space-time coding. For

a BER of  $5 \cdot 10^{-5}$ , the STTC provides a gain of 2 dB over the STBC scheme.

Figure 7 shows the simulation results for 3 bps using one receiving antenna for the STBC scheme (code G2) and STTC scheme (16 states). Two transmit antennas with the 8-PSK constellation are used. For a BER of  $3 \cdot 10^{-5}$ , STTC provides a 3.4 dB gain over the STBC scheme.

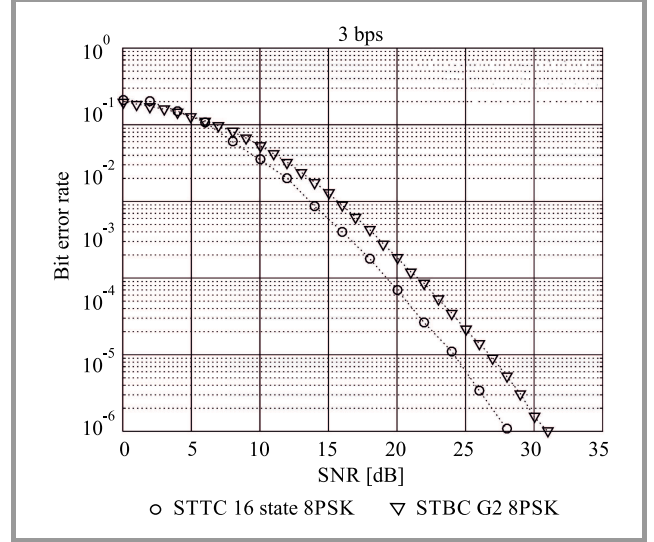


Fig. 7. BER versus SNR for spectral efficiency of 3 bps with only one receiving antenna.

Both block space time codes and space time trellis codes are characterized by broadcast diversity. Space-time codes in blocks are constructed from orthogonal matrixes and may all exploit diversity. They are easily decodable by a maximum likelihood decoder and linear processing at the reception, but they suffer from a lack of coding gain. On the other hand, the lattice space-time code has both diversity and coding gain, but it is complex to decode.

## 4. Trellis Coded Modulation

Trellis coded modulation (TCM) is one of the coded modulation techniques [18] used in MIMO systems. It combines the choice of a modulation scheme with that of a convolutional code, in order to obtain immunity against noise. More specifically, transmission is performed without increasing the bandwidth of the transmitted signal [19]. TCM is used in many modern transmission systems, such as modems.

For the 8-state TCM encoder with a spectral efficiency of 2 bps, the generating matrixes are [20]:

$$G = \begin{pmatrix} 0 & 0 & 1 \\ 1 & 0 & 0 \\ 0 & 1 & 0 \end{pmatrix}, \quad T = \begin{pmatrix} 0 & 0 \\ 1 & 0 \\ 0 & 1 \end{pmatrix}. \quad (12)$$

Matrix  $G$  is obtained by the dependence between each memory of the convolutional coder and the other memories. Matrix  $T$  is based on the dependence of the coder memory on coder inputs. The generator polynomial is:



$$P = (11, 02, 04)_8 \quad (13)$$

In Fig. 8, performance of the TCM scheme for 8-PSK modulation over the AWGN channel and Rayleigh channel is shown. The rate of this code is  $R = 2/3$ . It is clear from this figure that for a Gaussian channel, the gain provided by the TCM scheme is about 2 dB for a BER of  $10^{-5}$  and that this gain is 9 dB for a BER of  $10^{-3}$  over a Rayleigh channel.

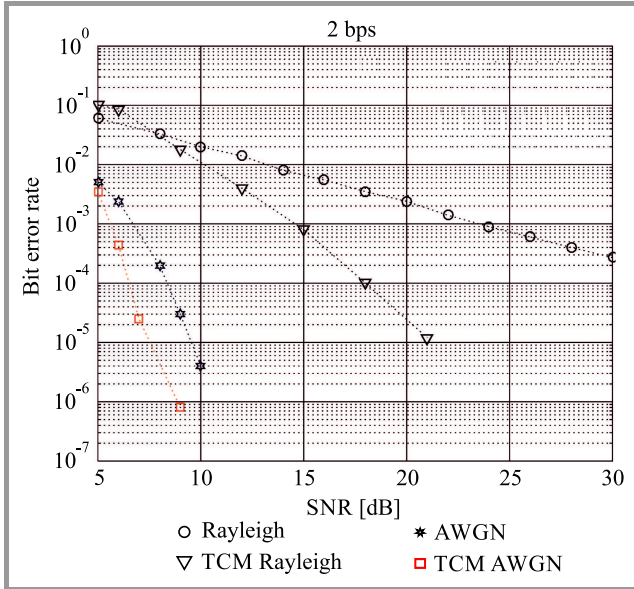


Fig. 8. Performance of TCM code in AWGN and Rayleigh channel.

Figure 8 illustrates that the use of TCM code modulation offers considerable gains in coding compared to an uncoded transmission system.

### 5. Association between TCM and STBC

In this section, the proposed scheme, named TCM-STBC, is presented. Figure 9 presents a block diagram of the scheme using TCM code modulation concatenated with STBC. The following are the different steps needed to transmit  $K$  bits (data source) using TCM-STBC:

1. In the TCM block, we choose  $N$ -states and the type of generator polynomial  $P$ , where the rate is:  $rate_{TCM} = \frac{K}{(K+1)}$ .

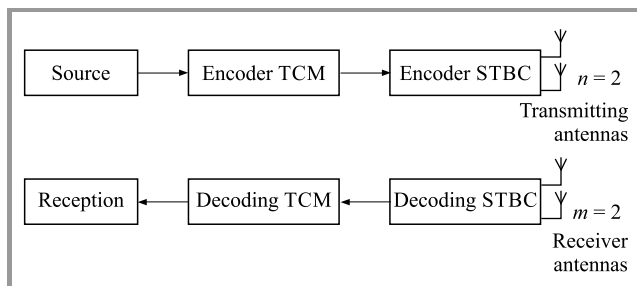


Fig. 9. Transmission system for STBC associated with TCM.

2. The number of bits at the output of the TCM block is equal to  $K + 1$  bits.
3. The resulting  $K + 1$  bits of step 2 are injected in the STBC block. Then, the STBC block rate will be  $rate_{STBC}$ , depending on  $G_M$  or  $H_M$  matrixes and the constellation type.
4. The resulting rate of the entire TCM-STBC system will be:  $rate_{TCM-STBC} = rate_{TCM} \times rate_{STBC}$ .
5. The output signal power is totally transmitted in whole when using one antenna. Otherwise, it will be equally divided when using multiple antennas.
6. At the receiver part, we applied the STBC and TCM decoding method.

Finally, we receive the transmitted data.

To enable a performance analysis of the proposed TCM-STBC scheme, Fig. 10 illustrates the impact of memory size (number of states) after the concatenation of the TCM with the STBC for 8-PSK modulation and the generator polynomial is  $P = (11, 02, 04)_8$  with spectral efficiency of 2 bps and  $2/3$ . We can notice that when increasing the number of states for the TCM coder, performance of BER, as a function of the SNR performance, improves. For example, for a BER of  $10^{-4}$ , the 16-state TCM-STBC provides a gain of about 1 dB over the 8-state TCM-STBC.

Comparison between TCM-STBC and STTC is performed for the same memory size. Since STTC offers comparable results for 16 and 32 states, the comparison is performed for 16 states. For spectral efficiency of 2 bps, TCM-STBC uses the 8-PSK modulation and the generator polynomial is  $P = (11, 02, 04)_8$  with a rate of  $2/3$ . For STTC, QPSK modulation in the Rayleigh channel is used.

Figure 11 shows a comparison between the performance of TCM-STBC (code G2) and STTC for one receiving antenna. It is clear that the gain generated by the use of TCM-STBC is considerable. For a BER of  $10^{-4}$  gain associated with STBC is 10.5 dB relative to STTC in the Rayleigh channel.

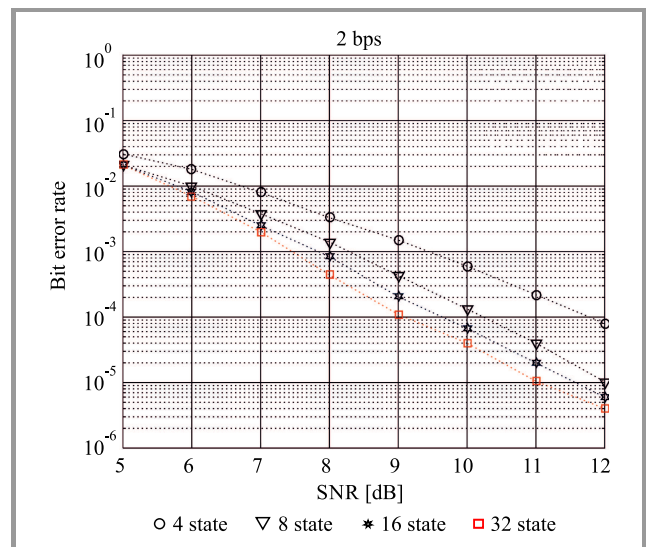


Fig. 10. Performance of TCM-STBC with 4, 8, 16 and 32 states.

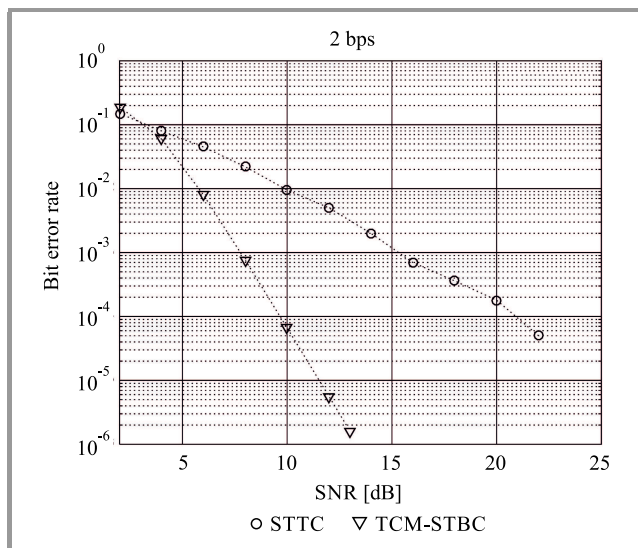


Fig. 11. Comparison between STTC and TCM-STBC proposed.

The results obtained illustrate the effectiveness of using TCM coding, as it offers a gain compared to STTC, thus leading to a diversity gains, unlike in the case of STTC which uses both coding and diversity gains.

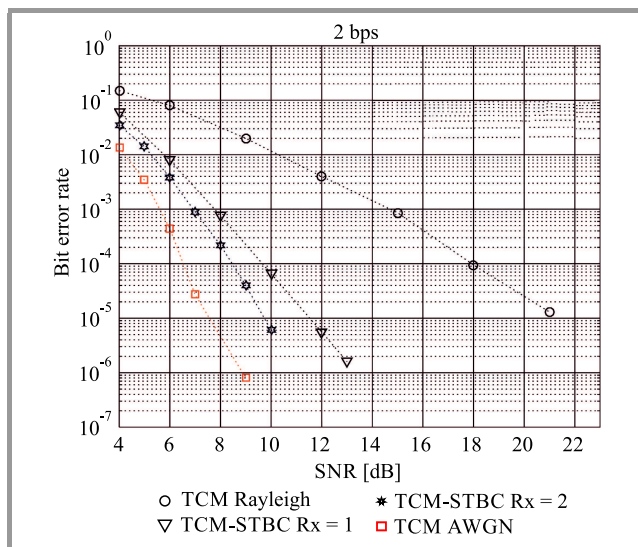


Fig. 12. Performance of TCM-STBC for one and two receiving antennas.

Figure 12 presents the effect of using two receive antennas for the TCM-STBC model (code G2) with 8-PSK modulation, spectral efficiency of 2 bps and a 2/3 rate in the Rayleigh channel. It is very clear that the curves showing BER versus SNR obtained with the use of TCM-STBC are well below the TCM curve in the Rayleigh channel. The gain is 9.5 dB for a single receiving antenna and 11.5 dB for two receiving antennas, for BER of 10<sup>-5</sup>. These curves are much closer to the curve obtained with the use of the TCM system in the AWGN channel. Indeed, the addition of a receiving antenna to the proposed TCM-STBC model improves the performance parameters concerned.

## 6. Conclusion

This paper focuses on multi-antenna radio systems that may be implemented in future generations of wireless networks. Space time block codes (STBC) with different antenna systems are presented and evaluated. BER performance of STBC and space time trellis code (STTC) solutions is compared using different configurations. The authors prove that the TCM scheme implemented over AWGN and Rayleigh channels may significantly improve performance of the transmission system.

Simulation results clearly show that the scheme we have proposed, relying on TCM code modulation and concatenated with the STBC system, significantly increases transmission performances. An increase in the number of encoder states generates additional gains, but significantly increases the calculation lead time during decoding. Moreover, addition of receiving antennas makes it possible to increase the efficiency of TCM associated with the STBC structure. This leads to a gain of 9.5 dB with one receiver antenna and 11.5 dB with two receiver antennas in the Rayleigh channel, and reduces SNR.

## References

- [1] J. K. Daksh, R. Mohan, and S. Sharma, "Performance analysis with space-time coding in MIMO-OFDM Systems with multiple antennas", *Int. J. of Adv. Comp. Res.*, vol. 3, no. 2, issue 10, 2013 [Online]. Available: <https://www.accentjournals.org/PaperDirectory/Journal/IJACR/2013/6/17.pdf>
- [2] R. Vithiya, V. Karthika, P. Samundeeswari, and S. Mohanraj, "Trellis coded modulation for MIMO wireless communication system", *Int. J. of Engin. Res. and Technol.*, vol. 2, no. 12, pp. 2577–2583, 2013 [Online]. Available: <https://www.ijert.org/research/trellis-coded-modulation-for-mimo-wireless-communication-system-IJERTV2IS120927.pdf>
- [3] Y. Wu, Y. Liu, H.-C. Chang, Y.-C. Liao, and H.-C. Chang, "Early-pruned k-best sphere decoding algorithm based on radius constraints", in *Proc. IEEE Int. Conf. on Commun. ICC 2008*, Beijing, China, 2008, pp. 4496–4500 (DOI: 10.1109/ICC.2008.843).
- [4] A. A. Kreshchuk and V. V. Zyablov, "Generalized concatenated system with embedded space-time codes for MIMO systems", *J. of Commun. Technol. and Electron.*, vol. 59, no. 12, pp. 1489–1500, 2014 (DOI: 10.1134/S1064226914120109).
- [5] E. Telatar, "Capacity of multi-antenna Gaussian channels", *Eur. Trans. on Telecommun.*, vol. 10, no. 6, pp. 585–595, 1999 (DOI: 10.1002/ett.4460100604).
- [6] S. A. K. Alrufaiaat and A. Q. J. Althahab, "Robust decoding strategy of MIMO-STBC using one source Kurtosis based GPSO algorithm", *J. of Ambient Intell. and Human. Comput.*, 2020 (DOI: 10.1007/s12652-020-02288-1).
- [7] S. R. Chopra, A. Gupta, and H. Monga, "Performance analysis of space time trellis codes in Rayleigh fading channel", in *Harmony Search and Nature Inspired Optimization Algorithms*, N. Yadav et al., Eds. Advances in Intelligent Systems and Computing, vol. 741, pp. 957–967. Springer, 2019 (DOI: 10.1007/978-981-13-0761-4\_90).
- [8] M. Hashem Ali Khan, T. Shin, M. H. Lee, and J.-G. Chung, "Signal constellations of quasi-orthogonal space-time codes for MIMO systems", *Wirel. Pers. Commun.*, vol. 85, no. 4, pp. 2003–2019, 2015 (DOI: 10.1007/s11277-015-2887-z).
- [9] Q. Jing and J. Wu, "Performance comparison of space-time block and trellis codes in the MIMO land mobile satellite channels", *Radioelectron. and Commun. Syst.*, vol. 60, no. 1, pp. 3–17, 2017 (DOI: 10.3103/S0735272717010010).

[10] M. Pushpakodi and N. Kumaratharan, "BER enhancement of MC-CDMA through B-STTC based STBC and STBC based B-STTC site diversity techniques", *Universal J. of Commun. and Netw.*, vol. 1, no. 3, pp. 81–87, 2013 (DOI: 10.13189/ujcn.2013.010301).

[11] H. A. Bakir, F. Debbat, and F. T. Bendimerad, "Performance comparison of STBC-OFDM with maximum likelihood detection for Rayleigh fading channel", *Int. J. of Engin. Res. in Africa*, vol. 26, pp. 111–121, 2016 (DOI: 10.4028/www.scientific.net/JERA.26.111).

[12] S. M. Alamouti, "A simple transmitter diversity technique for wireless communications", *IEEE J. on Sel. Areas in Commun.*, vol. 16, no. 8, pp. 1451–1458, 1998 (DOI: 10.1109/49.730453).

[13] V. Tarokh, H. Jafarkhani, and A. R. Calderbank, "Space-time block codes from orthogonal designs", *IEEE Trans. on Inform. Theory*, vol. 45, no. 5, pp. 1456–1467, 1999 (DOI: 10.1109/18.771146).

[14] V. Tarokh, H. Jafarkhani, and A. R. Calderbank, "Space-time block coding for wireless communications: Performance results", *IEEE J. on Sel. Areas in Commun.*, vol. 17, no. 3, pp. 451–460, 1999 (DOI: 10.1109/49.753730).

[15] L. L. Hanzo, T. H. Liew, B. L. Yeap, R. Y. S. Tee, and S. X. Ng, *Turbo Coding, Turbo Equalisation and Space-Time Coding*, 2nd ed. Wiley, 2011 (ISBN: 9780470978337).

[16] A. Wittneben, "Base station modulation diversity for digital simulcast", in *Proc. 41st IEEE Veh. Technol. Conf. VTC*, St. Louis, MO, USA, 1991, pp. 848–853 (DOI: 10.1109/VETEC.1991.140615).

[17] V. Tarokh, N. Seshadri, and A. R. Calderbank, "Space-time codes for high data rate wireless communication: Performance criterion and code construction", *IEEE Trans. on Inform. Theory*, vol. 44, no. 2, pp. 744–765, 1998 (DOI: 10.1109/18.661517).

[18] G. Ungerboeck, "Channel coding with multilevel/phase signals", *IEEE Trans. on Inform. Theory*, vol. 28, no. 1, pp. 55–67, 1982 (DOI: 10.1109/TIT.1982.1056454).

[19] L. F. Wei, "Trellis-coded modulation with multidimensional constellations", *IEEE Trans. on Inform. Theory*, vol. 33, no. 4, pp. 483–501, 1987 (DOI: 10.1109/TIT.1987.1057329).

[20] P. Robertson and T. Woz, "Bandwidth-efficient turbo trellis-coded modulation using punctured component codes", *IEEE J. on Sel. Areas in Commun.*, vol. 16, no. 2, pp. 206–218, 1998 (DOI: 10.1109/49.661109).



**Mohammed Sofiane Bendelhoum** obtained his B.Eng. degree in Biomedical Electronics and M.Sc. in Signals and Systems from Tlemcen University. He also earned his Ph.D. from Sidi Bel Abbes University, Algeria. Since 2014, he has been an Associate Professor at the University Center of El-Bayadh and performs his research at the

Instrumentation Laboratory and Advanced Materials University Center. His research interests are in image processing, medical image compression, wavelets transform, turbo encoding, turbo equalization, wireless communication systems and signal processing.

E-mail: Bendelhoum\_med@yahoo.fr

Instrumentation Laboratory and Advanced Materials (ILAM)  
University Center Nour Bachir of El-Bayadh  
El-Bayadh, Algeria

Department of Electrical Engineering  
University Center Nour Bachir of El-Bayadh  
El-Bayadh, Algeria



**Mohamed Rida Lahcene** received his B.Eng. degree in 2009, M.Sc. in 2012, and Ph.D. in 2018 – all from the University of Bechar Algeria. Since 2020, he has been working as an Associate Professor at the University Center Salhi Ahmed of Naama, Algeria. His main interests are in turbo encoding schemes, iterative decoding

over fading channels, and complexity of encoders.

E-mail: lahcenredal@gmail.com

Information Processing and Telecommunication  
Laboratory (LTIT)

Tahri Mohammed Bechar University

Bechar, Algeria

Department of Technology

University Center Salhi Ahmed of Naama

Naama, Algeria



**Fayssal Menezla** obtained his B.Eng. degree in Telecommunications, M.Sc. in Electronics and Ph.D. in Electronics, all from University of Djillali Liabes of Sidi Bel Abbes, Algeria. His research interests are in image processing, source coding, channel codes, joint coding, wireless communication systems and optimal encoders.

E-mail: menezla@yahoo.fr

Department of Electrical Engineering

University Center Nour Bachir of El-Bayadh

El-Bayadh, Algeria

Laboratory (LEPO)

Djillali Liabes University

Sidi Bel-Abbes, Algeria



**Elarbi Abderraouf** received the B.Eng. degree from the University of Molay Taher Saida, Algeria in 2008, and his M.Sc. from the University of Bechar, Algeria in 2013, and the Ph.D. degree, in 2020, from University of Bechar, Algeria. His main interests are turbo encoding schemes, multicarrier-CDMA transmission techniques

for integrated broadband cellular systems, iterative decoding over fading channels.

E-mail: elarbiabderraouf12@gmail.com

Information Processing and Telecommunication  
Laboratory (LTIT)

Tahri Mohammed Bechar University

Bechar, Algeria



# High-resolution Direction of Arrival Estimation Method Based on Sparse Arrays with Minimum Number of Elements

Jafar Ramadhan Mohammed

*College of Electronics Engineering, Ninevah University, Mosul, Iraq*

<https://doi.org/10.26636/jtit.2021.143720>

**Abstract**—Regular fully filled antenna arrays have been widely used in direction of arrival (DOA) estimation. However, practical implementation of these arrays is rather complex and their resolutions are limited to the beamwidth of the array pattern. Therefore, higher resolution and simpler methods are desirable. In this paper, the compressed sensing method is first applied to an initial fully filled array to randomly select the most prominent and effective elements which are used to form the sparse array. To keep the dimension of the sparse array equal to that of the fully filled array, the first and the last elements were excluded from the sparseness process. In addition, some constraints on the sparse spectrum are applied to increase estimation accuracy. The optimization problem is then solved iteratively using the iterative reweighted  $l_1$  norm. Finally, a simple searching algorithm is used to detect peaks in the spectrum solution that correspond to the directions of the arriving signals. Compared with the existing scanned beam methods, such as the minimum variance distortionless response (MVDR) technique, and with subspace approaches, such as multiple signal classification (MUSIC) and ESPRIT algorithms, the proposed sparse array method offers better performance even with a lower number of array elements and in severely noisy environments. Effectiveness of the proposed sparse array method is verified via computer simulations.

**Keywords**—compressed sensing, direction of arrival (DOA) estimation, sparse array.

## 1. Introduction

The performance of many modern communication systems depends directly on the precision of estimating the direction of arrival of the signals that impinge on the antenna arrays used [1]–[2]. High directional beamforming that is a feature of antenna arrays is important not only for good performance but also for achieving high-resolution direction of arrival (DOA) estimates. It is known that the angular resolution (i.e. the angular distance between the two closely spaced sources) of an aerial array is limited by its beamwidth which, in turn, is reversely proportional to the

array dimension or aperture size. This means higher resolutions may be obtained by increasing array dimensions (i.e. using a larger number of array elements) – an approach relied upon by current massive MIMO systems. However, high cost of implementation and fault diagnosis associated with such large arrays continues to remain the key practical constraint. To obtain high resolution DOA estimators, many methods have been proposed in the literature [2]–[6]. These methods may be divided into three basic categories, according to their mathematical formulations. The first category is based on the array beam scanning (or beamforming) concept, such as delay-and-sum (DS) beamformer [7] and the minimum variance distortionless response (MVDR) beamformer [8], where array elements may either be distributed uniformly along linear or planar forms, or may be non-uniformly spaced arrays. The second category is based on the subspace approach, such as MUSIC [9], ESPRIT [10] and their variants, where the observation space is decomposed into signal and noise subspaces. The third category is based on stochastic optimization algorithms, such as genetic algorithm (GA) [11], particle swarm optimization (PSO) [12] or maximum likelihood methods [13].

The second and the third types usually perform well, but their computational complexity is generally high, especially when dealing with a large number of array elements. Less attention has been attached to the first category, due to the main beam limitation. However, among these three types of DOA estimations, the array beamforming method enjoys many implementation-related advantages, such as simplicity, versatility, effectiveness and low costs when controlling only a part of array elements, instead of all of them, i.e. when optimizing only the most effective and prominent array elements, instead of optimizing all of them [14]–[17]. Thus, the array beamforming methods may be relied upon to achieve good and competitive solutions. However, their angular resolutions are limited by the arrays' physical apertures, meaning they are unable to distinguish between two spatial sources within beam widths of the array's radiation



patterns. Therefore, overcoming this limitation is currently an important research direction. In papers [18]–[20], the authors presented different methods based on compressed sparse arrays for DOA estimation.

In this paper, an antenna array-based beamforming method that utilizes a compressive sensing approach for DOA estimation is presented. The proposed method is applicable to both linear and planar array configurations. An initial regular antenna array with full density is first considered, and then only the most effective and prominent elements are chosen randomly to reconstruct the sparse array. To keep the array dimension fixed, the first and the last elements of the initial regular array were excluded from the sparseness process. Next, the problem is optimized iteratively to find the optimum sparse elements, which are used to reconstruct the required signals and to estimate their directions. The effect of the SNR and of the minimized number of the sparse elements on estimation performance of the proposed method is also presented and is compared with other existing methods. Furthermore, the resolution and the maximum allowable number of estimated directions are analyzed as well.

## 2. Sparse Array Method

Consider a fully filled linear array consisting of  $N$  elements that are distributed uniformly with a separation distance of  $d$ , receiving  $P$  signals from a far field region. For simplicity, mutual couplings between the array elements are ignored. The output signal  $x(k) \in C^{N \times 1}$  is:

$$\mathbf{x}(k) = \mathbf{A}(\theta)\mathbf{s}(k) + \mathbf{n}(k), \quad (1)$$

where:

$k$  is the discrete time which is equal to  $k = 1, 2, \dots, L$ , and  $L$  is the total number of snapshots,

$\mathbf{s}(k) \in C^{P \times 1}$  is the complex amplitude of signal  $\mathbf{s}(k) = [s_1(k) \ s_2(k) \ \dots \ s_P(k)]^T$  which is a vector representing signals with size  $P \times 1$ ,

$P$  is the total number of signal sources that impinge on the array,

$\mathbf{n}(k) \in C^{N \times 1}$  is the complex vector of noise,

$\mathbf{A}(\theta) = [\mathbf{a}_1(\theta_1) \ \mathbf{a}_2(\theta_2) \ \dots \ \mathbf{a}_P(\theta_P)]$  is an  $N \times P$  matrix of steering vectors with  $\mathbf{a}(\theta) = \frac{1}{\sqrt{N}} [1 \ e^{-j\frac{2\pi d}{\lambda} \sin(\theta)} \ \dots \ e^{-j(N-1)\frac{2\pi d}{\lambda} \sin(\theta)}]^T$ .

Here, the values of  $\theta$  are between  $-\pi/2$  and  $\pi/2$ . In general, the directions of the received signals, i.e.  $\mathbf{s}(k)$ , are unknown and need to be determined. In the array beamforming methods, the scanned beams are used to estimate the signals' DOA. This may be done simply by dividing the total scanning region into a certain number of grids or angles, e.g.  $G$ . By using steering vector  $\mathbf{a}(\theta)$  for  $N$  values of  $\theta$ , the discrete grid (or scan angle) matrix  $\Psi$  can be given by  $\Psi(\theta) = [\mathbf{a}_1(\theta_1) \ \mathbf{a}_2(\theta_2) \ \dots \ \mathbf{a}_N(\theta_N)]$  with  $N \times N$  dimension. The  $\theta_1, \theta_2, \dots, \theta_N$  are the set of discrete points within

the scan region (or angles to be scanned). Let the signal received by the array elements be  $\mathbf{r}_s(k) = [r_{s1} \ \dots \ r_{sN}]^T$ . The received signal is now multiplied with the scan angle matrix  $\Psi$  as:

$$\mathbf{x}(k) = \Psi(\theta) \mathbf{r}_s(k) + \mathbf{n}(k). \quad (2)$$

As a result, the scanned beam can be obtained in which the DOAs of the source signals are visible. Then, the array beam is scanned for each angle within the spatial spectrum. The peak values indicate the DOAs of the received signals. Figure 1a shows the result of applying classic two dimensional DS beamformer array with  $5 \times 5$  elements distributed uniformly at a distance  $\lambda/2$  on a rectangular grid to estimate both azimuth and elevation angles of two signals that impinged on the array from directions  $0, 0$  and  $-10^\circ, 10^\circ$ , while Fig. 1b shows the result of applying the two dimensional standard MVDR beamformer array for the same scenario as above. One may observe that the DS method fails to estimate the two closely-spaced signals due to its widened beamwidth pattern which is larger than the angular separation between the two impinged signals. On the other hand, the MVDR method offers better resolution and is capable of accurately estimating both signals provided that the positions of the array elements are perfectly determined and there no imperfection errors are present.

To increase the resolution of the arrays under consideration, the results shown in Fig. 1 are recalculated, as presented in Fig. 2, with an increased array dimension (i.e. an array with  $10 \times 10$  elements instead of  $5 \times 5$  elements). From these results, as expected, a general improvement in the resolution is observed, at the cost of higher computational complexity which is undesirable and may limit the range of practical implementations. This problem may be solved by compressing sparse arrays, as shown below.

The mathematical formulation of compressive sensing that takes into consideration signal  $\mathbf{x}(k) \in C^{N \times 1}$ , sparseness matrix  $\Psi_s(\theta)$  with dimension  $N \times N$ , and  $P$ -sparse signal vector  $\mathbf{z}$  with dimension  $N \times 1$ , may be expressed as  $\mathbf{x} = \Psi_s \mathbf{z}$ , where  $P$ -sparse means that only  $P < N$  entries in the vector are non-zero. The goal of the compressed sensing method is to recover the output signal  $\mathbf{x}(k) \in C^{N \times 1}$  using a smaller set of measurements, say  $M \times 1$  instead of  $N \times 1$ , where  $M$  is less than  $N$ . Thus,  $\mathbf{x}(k) \in C^{N \times 1}$  will be changed to a new vector called measurement vector  $\mathbf{y}(k) \in C^{M \times 1}$ . Then, the system becomes underdetermined, as it consists of linear equations with numerous solutions, i.e. it does not have a unique solution as long as  $M < N$ . Measurement vector  $\mathbf{y}$  may be related to sensing matrix  $\Phi$  of dimension  $M \times N$  as  $\mathbf{y} = \Phi \mathbf{x}$ . In light of the above, the output of the sparse array  $\mathbf{y}(k) \in C^{M \times 1}$  may be given by:

$$\mathbf{y}(k) = \Phi(\theta) \mathbf{x}(k) = \Phi(\theta) \Psi_s(\theta) \mathbf{z}(k) = \Theta(\theta) \mathbf{z}(k), \quad (3)$$

where  $\Theta(\theta)$  is the observation matrix with dimension  $M \times N$ .  $P$  sources from only  $M$  measurements of  $\mathbf{y}(k)$  are then found by applying compressed sensing. It should be

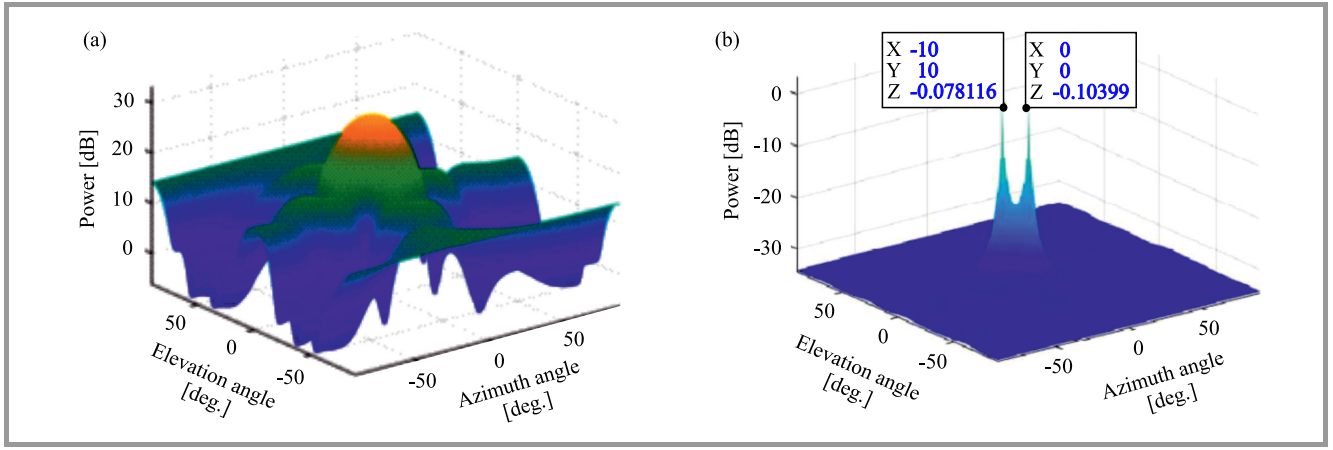


**Fig. 1.** Results for a  $5 \times 5$  uniform planar array, classical DS method (a) and for standard MVDR method (b). (For color pictures see the digital version of the paper).

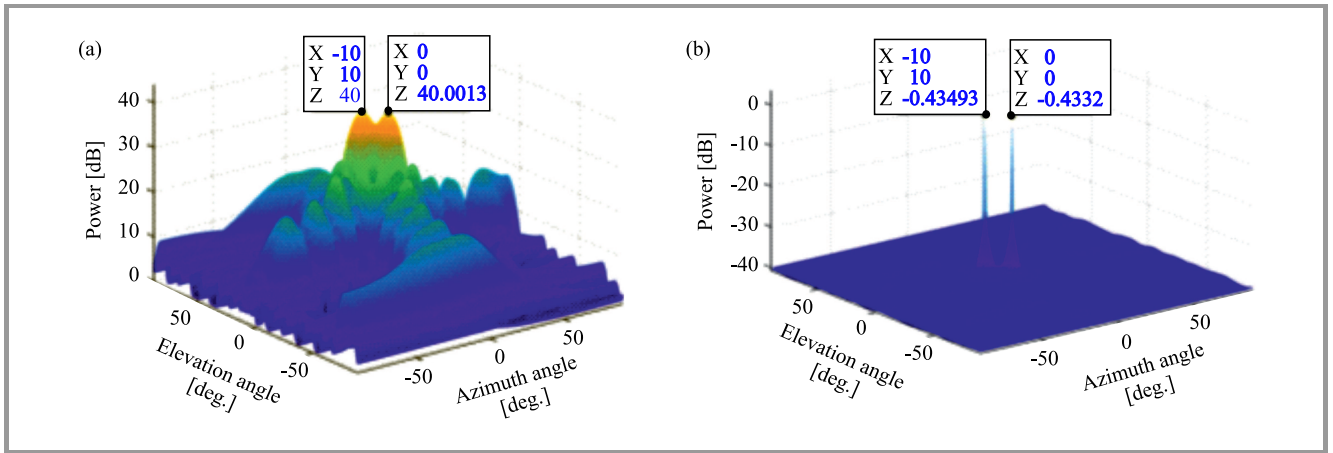


**Fig. 2.** Results for a  $10 \times 10$  uniform planar array, classical DS method (a) and for standard MVDR method (b).

mentioned that the system in Eq. (1) may be solved by means of the least squares method:

$$\min \|\mathbf{s}\|_2 \text{ subject to } \mathbf{A}\mathbf{s} = \mathbf{x} , \quad (4)$$

and its solution is:

$$\mathbf{s}_{ls} = \mathbf{A}^T (\mathbf{A}\mathbf{A}^T)^{-1} \mathbf{x} . \quad (5)$$

In this paper, the author expects to find the sparse solution rather than the full solution using an iterative reweighted optimization algorithm. Therefore,  $\mathbf{s}$  is represented by  $\mathbf{s} = \mathbf{W}\mathbf{q}$ , where  $\mathbf{s}$  is the unknown source vector,  $\mathbf{W}$  is the weighting matrix with dimension  $N \times N$ , and  $\mathbf{q}$  may be found from:

$$\min \|\mathbf{q}\|_2^2 \text{ subject to } \mathbf{A}\mathbf{W}\mathbf{q} = \mathbf{x} . \quad (6)$$

Equation (6) is solved iteratively using the reweighted  $l_1$  norm in conjunction with the algorithm that was presented in [21]. To detect the peaks in the spectrum solution that correspond to the directions of the arrived signals, a simple searching algorithm is applied to the final optimization solution. Note that only  $M$  out of  $N$  array elements are used

to reconstruct the signals and estimate their DOAs. Thus, computational complexity is greatly reduced.

### 3. Simulation Results

In this section, extensive simulation results are demonstrated to illustrate the effectiveness of the proposed method. First, performance in terms of mean squared errors (MSE), signal-to-noise ratio (SNR), resolution and computational complexity of such conventional methods as DS, MVDR, MUSIC, ESPRIT, and the proposed method are demonstrated to verify the superiority of the proposed method.

In all scenarios, a full dense (filled) antenna array with  $N = 30$  identical elements is considered, and all received signals are of the narrow-band variety. For regular full dense arrays, the separation distance between their elements is set to  $d = \lambda/2$ . The number of snapshots is set to  $L = 1$ . The power of each signal source is set to 0 dBm and the power of noises is specified. To evaluate the estimation performance of the tested methods, MSE – representing

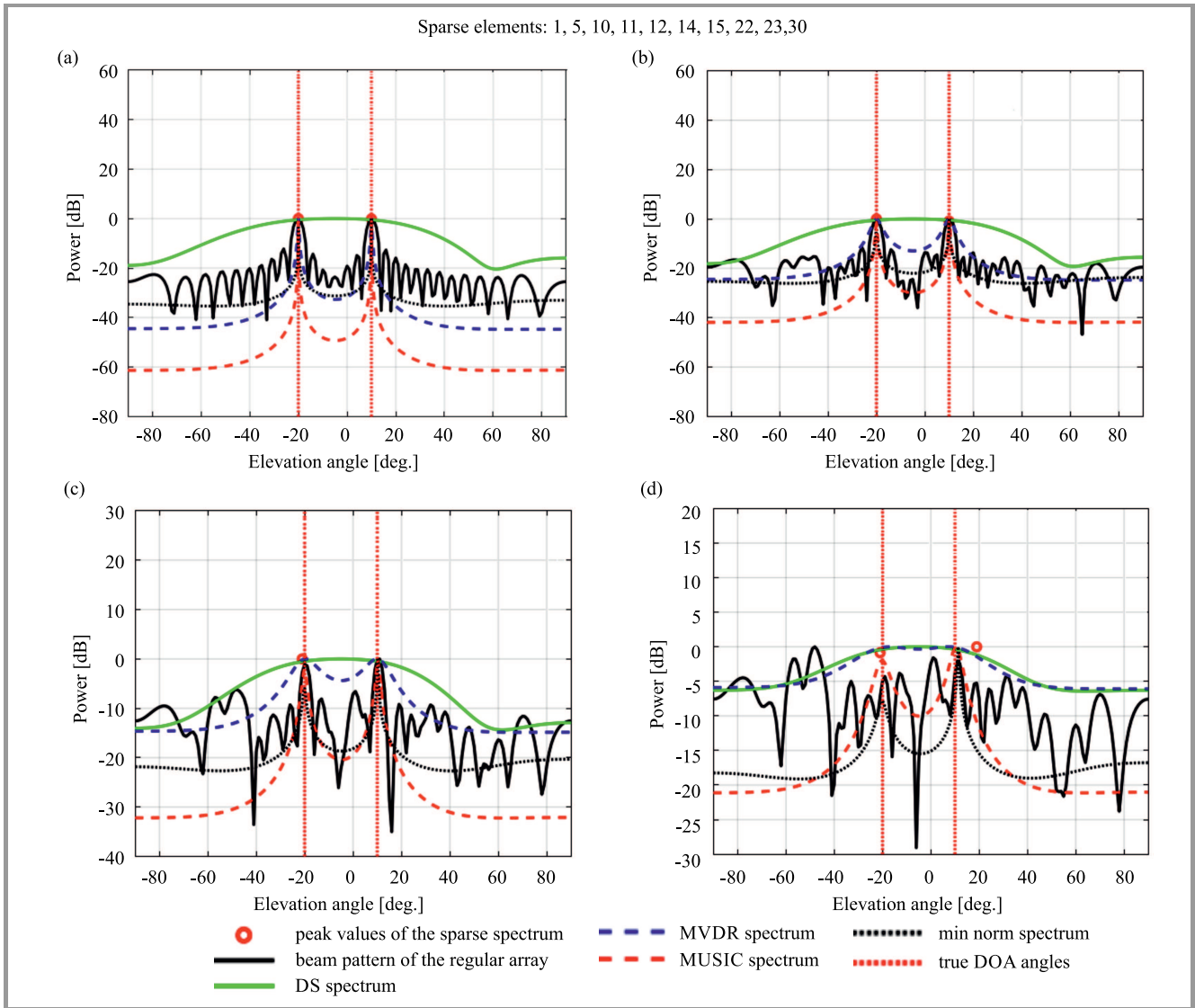


**Fig. 3.** Results for the tested methods for  $N = 30$ ,  $M = 10$  for two sources at  $(-20^\circ, 10^\circ)$  and SNR: (a) 30 dB, (b) 10 dB, (c) 0 dB, (d)  $-10$  dB.

the deviation between the estimated  $\check{\mathbf{x}}$  and the actual  $\mathbf{x}_0$  DOA values – was calculated as:

$$\text{MSE} = E \frac{\|\check{\mathbf{x}} - \mathbf{x}_0\|_F^2}{\|\mathbf{x}_0\|_F^2}, \quad (7)$$

where  $\|\cdot\|_F$  represents the Frobenius norm. A lower MSE value means better estimation accuracy. To construct the sparse array, we assume that only 8 randomly elements out of  $N = 30$  regular elements will remain in the resulting compressed array. As mentioned earlier, to maintain the array dimension unchanged, rows number 1 and 30 of the measurement matrix will always remain. Thus, the total number of the compressed array elements including the two end elements will be  $M = 10$ . Then, the beam width of the initial full dense array with  $N = 30$  is equal to  $3.38^\circ$  and is same as that of the compressed array with  $M = 10$ , since the overall array dimension remained unchanged. The range

of the scanning region is chosen to be from  $-90^\circ$  to  $90^\circ$ . Then, the total number of the angles that need to be scanned is equal to 181 and the angular separation between any two tested angles is set to be  $1^\circ$ , i.e. is lower than the beamwidth value, thus enabling to attain maximum resolution levels.

For the proposed method, first the sparse spectrum of the reconstructed signals is found by using the algorithm that was presented in [22]–[23]. Then, the peak values that correspond to the estimated DOAs are calculated by using a simple searching algorithm. Finally, the peak values are plotted and compared with other tested methods, as shown in the following scenarios.

In the first scenario, two uncorrelated sources located at  $\theta_1 = -20^\circ$  and  $\theta_2 = 10^\circ$  with four different SNRs: 30, 10, 0, and  $-10$  dB, are considered. Figure 3 shows the results of applying the proposed sparse array and compares them with those of the regular fully filled array: DS, MVDR, MUSIC, and min norm methods. For the proposed sparse

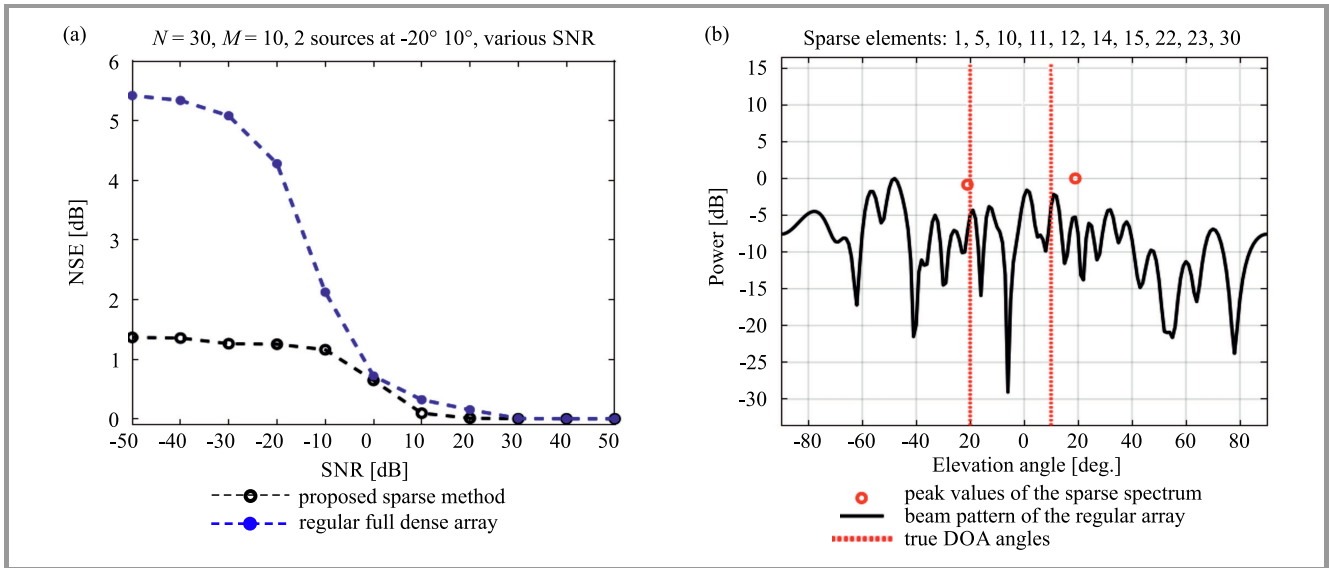


Fig. 4. MSE vs. SNR (a) and one sample result for SNR = -10 dB (b).

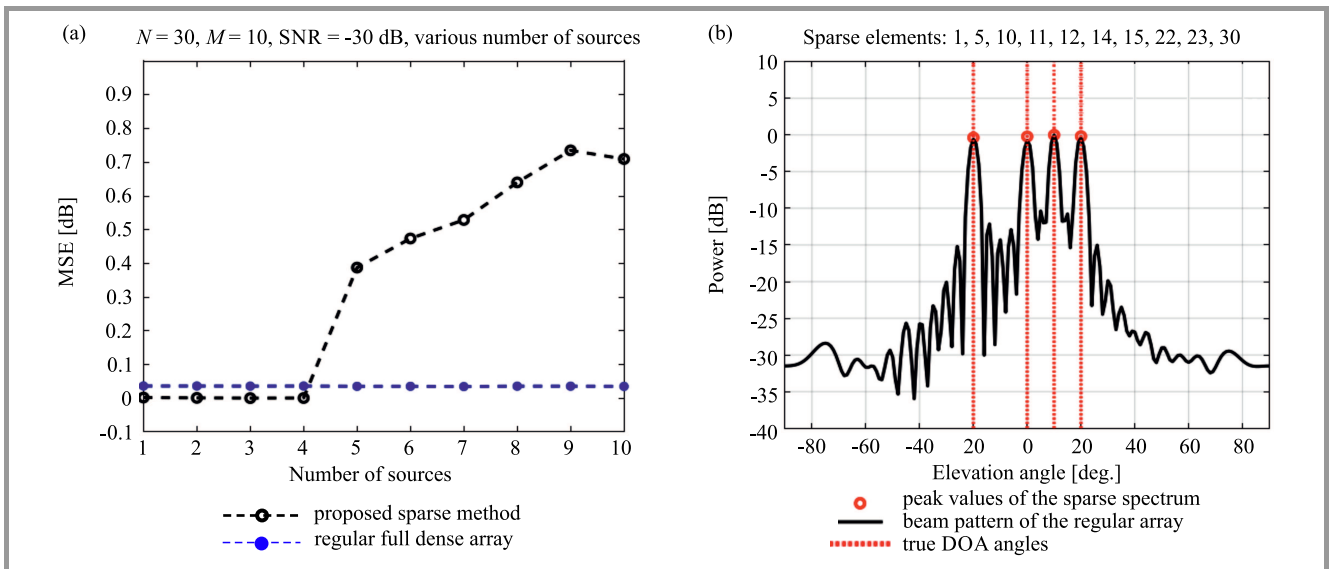


Fig. 5. MSE vs. the number of sources (a) and one sample result for four sources (b).

array method, the indices of the elements that remain after the sparseness process are also shown at the top of Fig. 3. It may be observed that all of the tested methods, including the proposed method with sparse elements of indices 1, 5, 10, 11, 12, 14, 15, 22, 23, and 30, perform very well as far as estimating the correct DOAs under high SNR is concerned. This estimation degrades for low SNR levels. For the proposed method and for each considered SNR value, the estimated DOAs were found to be  $(-20^\circ, 10^\circ)$ ,  $(-20^\circ, 10^\circ)$ ,  $(-21^\circ, 11^\circ)$  and  $(-21^\circ, 19^\circ)$ , meaning they differ from the true DOA angles by the following MSE values: 0.001, 0.0941, 0.6443, and 1.1588, respectively. Although little deviations in the estimation of DOA exists for SNR of -10 dB, performance of the proposed method was considered to be satisfactory. Figure 3d clearly shows the superiority of the proposed method in

comparison to all other tested methods which fail to estimate the DOAs.

In the second scenario, the estimation performance in terms of MSE of the proposed sparse and regular fully filled (or dense) arrays under various SNR values is further investigated and highlighted, as shown in Fig. 4. Sample results at specific -10 dB SNR are shown as well. Again, superiority of the proposed sparse array is evident, especially for lower SNR values.

In the third scenario, MSE is investigated versus the maximum allowable number of sources (Fig. 5). It may be observed that the maximum detectable number of source directions is only 4 for the case of  $M = 8$  sparse elements. The first and the last elements were not considered here, because they are not sparse elements. It should be noted that many other cases have been examined and, in general,

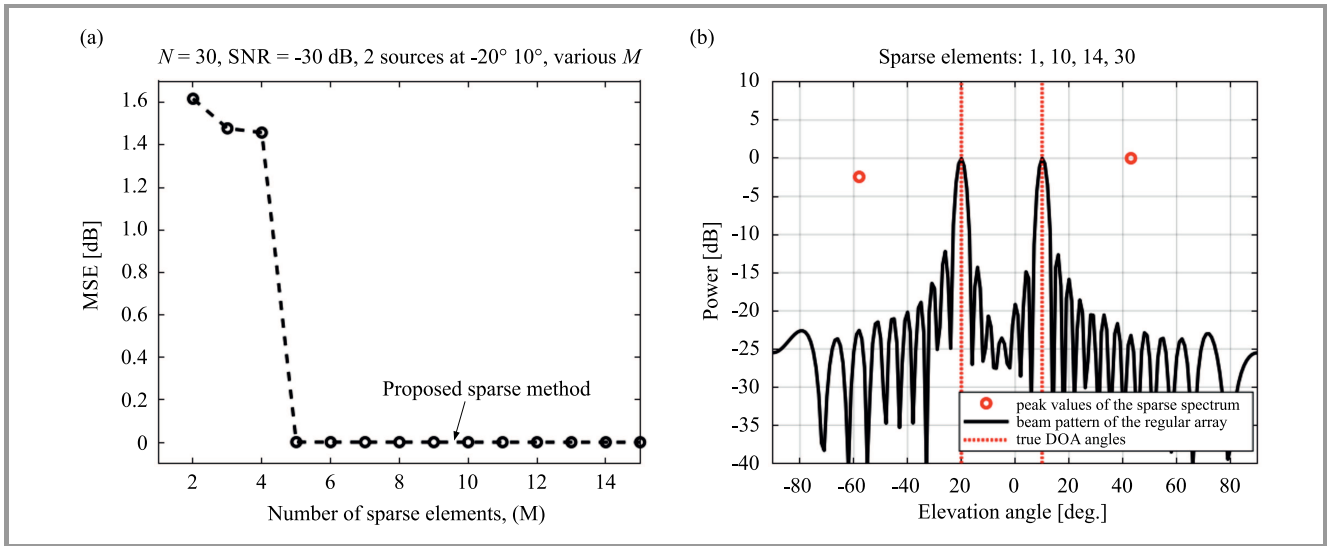


Fig. 6. MSE vs. the number of sparse elements (a) and one sample result for four sources for  $M = 2$  (b).

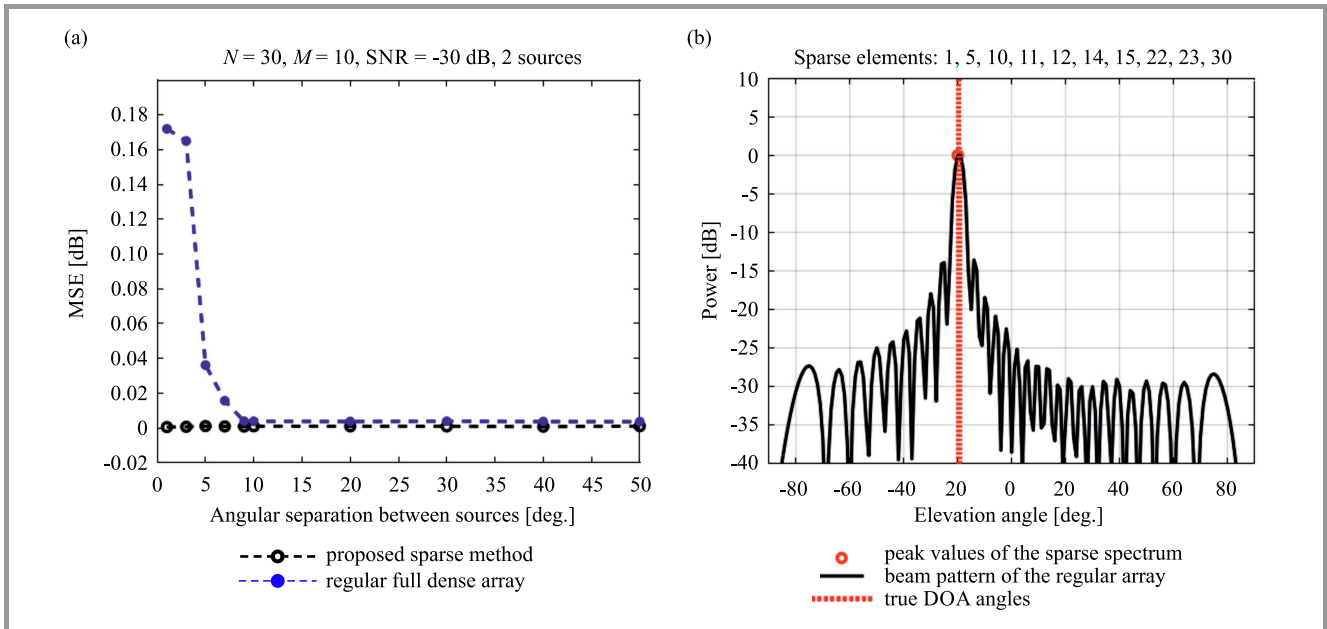


Fig. 7. MSE vs. angular separation between sources (a) and one sample result for  $1^\circ$  angular separation (b).

it is found that the maximum detectable number of source directions is directly proportional to the number of sparse elements. It may be expressed as  $M/\log N$  which is equal to 5.415 for  $M = 8$  and  $N = 30$ .

In the next scenario, the effect that the number of sparse elements exerts on estimation performance is studied, as shown in Fig. 6. It may be concluded that for two source directions and only two considered sparse elements, estimation performance is unsatisfactory and the directions are calculated incorrectly. To obtain correct directions, we need to set the value of  $M$  to equal at least 5 elements.

Finally, the resolution of the proposed sparse array under two closely spaced sources is investigated and shown in Fig. 7. Performance of the proposed array still remain better

than that of the regular full dense array, especially for very small angular distances, and this distinction vanishes for larger angular distances.

## 4. Conclusions

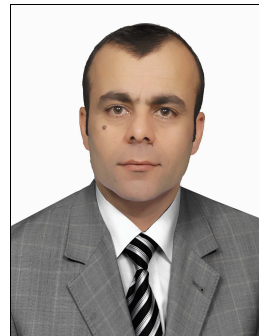
It has been shown that the proposed sparse array based compressed sensing method was effectively able to estimate the required DOAs. Its resolution was found to be accurate even under severe noisy environments. Moreover, the maximum allowable number of the detected sources was found to be proportional to the number of the sparse elements. In all tested scenarios, the output spatial spectrum



was plotted and compared. Unlike existing DOAs methods, the sparse spectrum of the proposed method had best spatial resolution.

## References

- [1] M. Guo, Y. D. Zhang, and T. Chen, "DOA estimation using compressed sparse array", *IEEE Trans. on Sig. Process.*, vol. 66, no. 15, pp. 4133–4146, 2018 (DOI: 10.1109/TSP.2018.2847645).
- [2] P. Gong, X. Zhang, and T. Ahmed, "Computationally efficient DOA estimation for coprime linear array: A successive signal subspace fitting algorithm", *Int. J. of Electron.*, vol. 107, no. 8, pp. 1216–1238, 2020 (DOI: 10.1080/00207217.2020.1726485).
- [3] B. D. van Veen and K. M. Buckley, "Beamforming: A versatile approach to spatial filtering", *IEEE Sig. Process. Mag.*, vol. 5, no. 2, pp. 4–24, 1988 (DOI: 10.1109/53.665).
- [4] M. Carlin, P. Rocca, G. Oliveri, F. Viani, and A. Massa, "Directions-of-arrival estimation through Bayesian compressive sensing strategies", *IEEE Trans. on Antenn. Propag.*, vol. 61, no. 7, pp. 3828–3838, 2013 (DOI: 10.1109/TAP.2013.2256093).
- [5] A. D. Lonkeng and J. Zhuang, "Two-dimensional DOA estimation using arbitrary arrays for massive MIMO systems", *Int. J. of Antenn. and Propag.*, vol. 2017, Article ID 6794920, 2017 (DOI: 10.1155/2017/6794920).
- [6] A. B. Gershman, M. RübSamen, and M. Pesavento, "One- and two-dimensional direction-of-arrival estimation: an overview of search-free techniques", *Sig. Process.*, vol. 90, no. 5, pp. 1338–1349, 2010 (DOI: 10.1016/j.sigpro.2009.12.008).
- [7] T. C. Yang, "Deconvolved conventional beamforming for a horizontal line array", *IEEE J. of Oceanic Engin.*, vol. 43, no. 1, pp. 160–172, 2018 (DOI: 10.1109/JOE.2017.2680818).
- [8] J. Capon, "High-resolution frequency-wavenumber spectrum analysis", *Proc. of the IEEE*, vol. 57, no. 8, pp. 1408–1418, 1969 (DOI: 10.1109/PROC.1969.7278).
- [9] R. O. Schmidt, "Multiple emitter location and signal parameter estimation", *IEEE Trans. on Antenn. and Propag.*, vol. 34, no. 3, pp. 276–280, 1986 (DOI: 10.1109/TAP.1986.1143830).
- [10] R. Roy and T. Kailath, "ESPRIT-estimation of signal parameters via rotational invariance techniques", *IEEE Trans. on Sig. Process.*, vol. 37, no. 7, pp. 984–995, 1989 (DOI: 10.1109/29.32276).
- [11] X. Fan, L. Pang, P. Shi, G. Li, and X. Zhang, "Application of bee evolutionary genetic algorithm to maximum likelihood direction-of-arrival estimation", *Mathem. Probl. in Engin.*, vol. 2019, Article ID 6035870, 2019 (DOI: 10.1155/2019/6035870).
- [12] H. Chen, S. Li, J. Liu, F. Liu, and M. Suzuki, "A novel modification of PSO algorithm for SML estimation of DOA", *Sensors*, vol. 16, no. 12, 2016 (DOI: 10.3390/s16122188).
- [13] S. Zhao, Y. S. Shmaliy, and C. K. Ahn, "Iterative maximum likelihood FIR estimation of dynamic systems with improved robustness", *IEEE/ASME Trans. on Mechatron.*, vol. 23, no. 3, pp. 1467–1476, 2018 (DOI: 10.1109/TMECH.2018.2820075).
- [14] K. H. Sayidmarie and J. R. Mohammed, "Performance of a wide angle and wideband nulling method for phased arrays", *Progr. in Electromag. Res. M*, vol. 33, pp. 239–249, 2013 (DOI: 10.2528/PIERM13100603).
- [15] J. R. Mohammed, "Design of printed Yagi antenna with additional driven element for WLAN applications", *Progr. in Electromag. Res. C*, vol. 37, pp. 67–81, 2013 (DOI: 10.2528/PIERC12121201).
- [16] J. R. Mohammed, "Element selection for optimized multi-wide nulls in almost uniformly excited arrays", *IEEE Antenn. and Wirel. Propag. Lett.*, vol. 17, no. 4, pp. 629–632, 2018 (DOI: 10.1109/LAWP.2018.2807371).
- [17] J. R. Mohammed and K. H. Sayidmarie, "Sidelobe cancellation for uniformly excited planar array antennas by controlling the side elements", *IEEE Antenn. and Wirel. Propag. Lett.*, vol. 13, pp. 987–990, 2014 (DOI: 10.1109/LAWP.2014.2325025).
- [18] J. Zhang, Z. Duan, Y. Zhang, and J. Liang, "Compressive sensing approach for DOA estimation based on sparse arrays in presence of mutual coupling", in *Communications, Signal Processing, and Systems. Proceedings of the 8th International Conference on Communications, Signal Processing, and Systems*, Q. Liang et al., Eds. *Lecture Notes in Electrical Engineering*, vol. 516. Springer, 2020 (DOI: 10.1007/978-981-13-6504-1\_151).
- [19] H. Li, C. Wang, and X. Zhu, "Compressive sensing for high-resolution direction-of-arrival estimation via iterative optimization on sensing matrix", *Int. J. of Antenn. and Propag.*, vol. 2015, no. 1, Article ID 713930, 2015 (DOI: 10.1155/2015/713930).
- [20] S. F. Cotter, B. D. Rao, K. Engan, and K. Kreutz-Delgado, "Sparse solutions to linear inverse problems with multiple measurement vectors", *IEEE Trans. on Sig. Process.*, vol. 53, no. 7, pp. 2477–2488, 2005 (DOI: 10.1109/TSP.2005.849172).
- [21] I. F. Gorodnitsky and B. D. Rao, "Sparse signal reconstruction from limited data using FOCUSS: A re-weighted minimum norm algorithm", *IEEE Trans. on Sig. Process.*, vol. 45, no. 3, pp. 600–616, 1997 (DOI: 10.1109/78.558475).



### Jafar Ramadhan Mohammed

received his B.Sc. and M.Sc. degrees in Electronics and Communication Engineering in 1998 and 2001, respectively, and Ph.D. in Digital Communication Engineering from Panjab University, India in 2009. He was a Visiting Lecturer at the Faculty of Electronics and Computer Engineering of the

Malaysia Technical University Melaka (UTeM), Melaka, Malaysia in 2011 and at the Autonomia University of Madrid, Spain in 2013. He is currently a Professor and Vice Chancellor for Scientific Affairs at Ninevah University. His main research interests are in the area of digital signal processing and its applications, antennas, and adaptive arrays.

 <https://orcid.org/0000-0002-8278-6013>

E-mail: jafarram@yahoo.com

College of Electronics Engineering  
Ninevah University  
Mosul, Iraq

# Location Estimation of Nodes in Underwater Acoustic Sensor Networks

B. S. Halakarnimath and A. V. Sutagundar

<sup>1</sup> *Research Scholar of VTU, Department of Computer Science and Engineering, S.G. Balekundri Institute of Technology, Belagavi, Karnataka, India*

<sup>2</sup> *Department of Electronics and Communication, Basaveshwar Engineering College, Bagalkot, Karnataka, India*

<https://doi.org/10.26636/jtit.2021.145720>

**Abstract**—The paper presents a location estimation scheme for underwater acoustic sensor networks. During the first phase, the sink node begins the trapezoid formation process by activating the trapezoid formation agent. It stores relevant information in the sink's knowledge base and in the node's knowledge base, and also develops the search data structure required for locating the node. During the second phase, the position of the node is determined by utilizing the search data structure. Identification of the location of all nodes by traveling across the trajectory may be performed as well, as an alternative approach. When identifying the location of one node, the estimation is performed based on the search data structure. When determining the position of all nodes, the sink node agent travels along the defined trajectory and transmits beacon messages which contain the real-time location at specific points. The anchor node agent measures the signal strength and localizes itself and begins estimating the locations of other nodes within the trapezoids, using location estimation techniques. Various performance parameters are used to validate the proposed scheme.

**Keywords**—location estimation, trapezoid, UASN.

## 1. Introduction

Location estimation for large scale mobile underwater acoustic sensor networks (UASNs) is intriguing because of harsh aqueous environments. Even though acoustic methods are suitable for underwater communication, such features as moderate bandwidth and considerable failure rate impose specific constraints on location estimation schemes [1]. Propagation delays, movement-caused Doppler shifts, amplitude and phase fluctuations, and multipath obstruction are all factors that need to be taken into consideration in location determination procedures. Some of the localization-related issues are presented below [2]:

- need for a proper sound-speed variation model used for location estimation,
- immersed sensor nodes need precise time synchronization,
- efficient node mobility pattern for dynamic underwater conditions,

- impacts related to medium access control (MAC), including contention fixing, transmission overhead, localization accuracy and latency,
- implications of location estimation protocols for location-based routing and clustering techniques.

In this paper, a computational geometrical-based localization technique is presented. The proposed location estimation scheme works in the following manner.

During the first stage, the sink node begins the trapezoid formation process on the sea surface by activating the trapezoid formation agent (TFA) and by deploying an autonomous underwater vehicle (AUV) to reach a particular depth below the surface of the sea. The AUV travels across the linear trajectory of a fixed length, at a specific depth, and the TFA creates trapezoids in the upper and lower portions of the path. The TFA stores the relevant information in the sink knowledge base (SKB) and in the node knowledge base (NKB). In the meantime, the TFA develops also the SDS in order to locate the node in the easiest manner possible.

During the second phase, position of the node is determined by relying on two methods. The first method determines the node's location by utilizing the SDS, and the other consists in finding the location of all the nodes by traveling across the trajectory. In any case, the sink triggers the localization agent (LA) and deploys the AUV to a specific depth under the surface of the ocean.

In the case of finding the location of one node, the LA moves directly to the trapezoid, which is given per the SDS, and performs the localization process.

In the case of determining the position of all nodes, the AUV traverses along the continuing trajectory and transmits beacon messages which contain real-time locations at specific points. The anchor agent (AA) at the anchor node receives these beacon messages, measures the signal strength and localizes itself based on the position of the broadcast point and the received signal strength. The LA begins the location estimating activity with the associated trapezoids of the anchor nodes, relying on location estimation techniques.

All agents keep updating the information to the respective knowledge bases whenever the data is modified.

## 2. Problem Statement

In a fixed area water network  $O$ ,  $n$  uw-sensor nodes are randomly placed.  $m$  is the number of reference nodes with known locations and  $N$  is the total number of nodes existing in the network, where  $N = n + m$ . For a 2D localization problem  $N = [N_x, N_y]$ , where  $N_x = \{x_1, x_2, \dots, x_n\}$ ,  $N_y = \{y_1, y_2, \dots, y_n\}$  and where the reference nodes' coordinates are  $N_x = \{x_{n+1}, x_{n+2}, \dots, x_{n+m}\}$ ,  $N_y = \{y_{n+1}, y_{n+2}, \dots, y_{n+m}\}$ . The location of each uw-sensor node  $i$  is appended with a third coordinate  $Z_i$ , being the depth of each uw-sensor node. The 2D problem is extended to 3D by appending the third coordinate to each uw-sensor node location. The  $n_{x,y}$  measurement could be a physical reading indicating the relative position. Process the monitoring area of ocean  $O$ , and divide the network into trapezoids of variable sizes, find the trapezoid of  $O$  containing the uw-sensor node  $uw_i$ , and then estimate the location of unlocalized  $uw_i$  within that trapezoid. The aim is to design and simulate the above task by creating trapezoids to facilitate efficient localization by considering the dynamic characteristics of the ocean.

In the proposed location-estimation scheme, our research additions are as follows:

- Setting up a network to perform the localization process.
- Applying a computational geometry-based trapezoidal map forming numerous trapezoids of distinct shapes.
- Developing the AUV's path of travel and iteratively submitting real-time position information.
- Creating appropriate node agencies for the proposed MASD scheme.
- Developing methods for trapezoid formation, single-node location estimation, and for localization of all nodes.
- Simulating the proposed location estimation scheme.
- Evaluating the proposed MASD scheme based on different performance parameters.

## 3. Related Work

Range-free and range-based techniques are the two primary classifications of location estimation techniques [3]. The range-based schemes, such as time of arrival (ToA), time difference of arrival (TDoA), angle of arrival (AoA), and received signal strength indicator (RSSI) provide a relatively precise location compared with range-free schemes. The speed of underwater sound propagation encourages the employment of range-based schemes for underwater environments. The speed of sound depends on salinity, density, and temperature. It changes continuously in undersea conditions. Hence, an accurate time synchroniza-

tion model is also required. Assume that the sound speed change remunerated by applying signal processing methods. Range-based systems, such as TDoA and ToA, achieve relatively high accuracy levels but require more real-time synchronization within uw-nodes, which increases the cost of UASNs due to the additional hardware needed. Range-free location finding algorithms are accessible if high localization accuracy levels are not essential. In range-free schemes, neighboring ranges or angle learning is challenging to measure due to hardware limitations. Once the range between uw-nodes has been estimated, range-free techniques rely on trilateration to determine precise locations.

In [4], energy models of acoustic waves are applied to determine the location of acoustic sensors in physical networks. For the calculation of a specific target position, efficiency and impact analyses are performed by applying the Cramer-Rao bound (CRB). The ML approach provides exceptionally reliable results and an enhanced level of capacity for location estimation based on multiple sources. This approach is scalable and may cover more targets within a predefined sensor area. The scheme requires some improvement in terms of parameter sensitivity analysis and sequential Bayesian estimation. The authors proposed a non-distributed range-free method in [5] that presents a rough location calculation of a sensor within a particular area, instead of its exact position. A sensor node overhears beacons from various anchor nodes and records their power levels independently, measuring also the mode used by the recorded power signals of each anchor node. Once collected, the information is transmitted to the onshore sink to identify the area in which the anchor node is present. This approach is manageable, synchronization free and cooperative. It is also resistant to changes in the speed of sound.

In [6], an event-driven iterative distributed location estimation method is proposed that produces excellent throughput, still retaining a moderate percentage of beacon nodes. The mobility model is a shortfall of this work. Localization becomes more comfortable in undersea conditions if anchor/reference nodes are available within the network [7]. The link is adopted to succeed in the failures linked to the balance of the line of sight (LOS). Underwater signal reflection-enabled acoustic-based localization (UREAL) is suitable for networks operating in shallow water environments. It offers the use of multi-modal directional undersea piezoelectric transducers that are relied upon to create either directional or omnidirectional beacons. To distinguish between LOS/NLOS, RSSI is applied. To calculate the location, AoA is applied. This scheme is independent of the LOS link in performing the location estimation process. The finite difference time domain (FDTD) approach is applied to estimate the reflection points for non-line of sight (NLOS) positioning.

In [8], collision-free and collision-tolerant packet scheduling techniques are proposed for location estimation in single-hop underwater networks. Experimental analysis



proves that sophisticated collision design takes less time than its collision-free counterpart, when the average probability of packet loss is close to one. Authors in [9] describe different deployment approaches and their impacts on localization-related performance. They consider the tetrahedron deployment scheme for a 3D environment that performs better than cube deployment and random deployment schemes in terms of providing better localization ratios, minimizing localization errors, and maintaining better network connectivity. They emphasize that their future work should focus on designing a realistic model that considers the various conditions experienced in underwater environments, including mobility issues, sound speed variations and propagation losses. Harsh underwater environments require cooperation between the nodes for broader coverage and better accuracy in identifying locations of the nodes.

For NLOS localization, the least square cooperative localization method is considered in [10]. The authors analyze consistency and efficiency of least square cooperative localization. The Fisher information matrix (FIM) is derived for an NLOS bios model and proves that Gaussian bias produces the worst-case scenario, as well as that lower partial ordering leads to the largest FIM.

RSS-based localization for UASNs is proposed in [11]. The system model considers various attenuation parameters, spreading losses and issues related to the environment, in order to account for acoustic propagation losses. The author examines semi-definite programming with frequency-dependent RSS and RSS based to yield better localization performance.

The method known as localization technique for underwater sensor networks (LOTUS) [3] estimates the nodes' approximate location based on two reference/anchor nodes only, by using fewer iterations and with local interactions. Experimental results justified a reduction in overhead, improved localization coverage and minimum localization error compared with large-scale localization. A collaborative or n-hop multilateration primitive for higher accuracy in two computation models, i.e. the centralized and the distributed model, is presented in [12]. An atomic/collaborative multilateration used iteratively to compute the locations of unlocalized uw-sensors is adopted in [13]. The method presented in [14] employs two-phase localization, i.e. anchor node location estimation and other normal node localization based on mobility prediction. Parameters of mobility patterns are predicted by using the covariance algorithm. Prediction errors are minimized by employing the covariance algorithm.

In [15], the author presents a localization method using the mobile beacon (LoMoB) range-free algorithm. Sensor nodes receive beacon messages which contain location information, and are localized without communicating with other nodes. The beacon points are projected on the sensor nodes' three-dimensional horizontal plane. Once the projection is made, the 3D localization problem is converted into a 2D localization problem. The sensor node's location is estimated based on the potential locations, by using

a weighted mean of those potential locations. The author compares his scheme with LDB and shows a significant improvement in localization accuracy. The RSSI-assisted mobile anchor node location determination scheme is proposed in [16], aiming to reduce the location lead time and to enhance the level of location accuracy. Using the mobile anchor node's trajectory, projection of the sensor node is estimated by using the interpolation method supporting vector regression, which improves location accuracy. A curve matching method is designed to reduce the localization lead time and to obtain the perpendicular distances, along the mobile anchor node's linear trajectory, from each sensor node. The benefit of this scheme is that it requires a one-time trajectory for the mobile anchor node to locate other sensor nodes. To improve location accuracy even further, the error within the actual perpendicular distance and the estimated perpendicular distance in the curve matching method could be reduced.

The multi-anchor nodes' collaborative localization (MANCL) [17] method classifies the entire localization process into four sub-processes: ordinary node location estimation process, iterative location estimating method, enhanced 3D Euclidean distance calculation method, and 3D DV-Hop distance calculation method based on two-hop anchor nodes. The enhanced 3D Euclidean distance calculation process applies the transmission mechanism or the voting mechanism to estimate the transient locations of regular sensor nodes. During the 3D DV-Hop distance calculation process, the ordinary node's coordinates are calculated based on the average two-hop anchor node distance.

The double rate localization (DRL) method is described in [18], relying on one anchor for performing localization in multi-hop underwater acoustic networks (UANs). In this scheme, the localization process is divided into high-rate and low-rate transmission modes by selecting an appropriate bit duration to ensure the transmission rate and to improve the accuracy of range measurements in multi-hop networks. Optimized selection of reference nodes improves the accuracy of localization performed with the help of one anchor.

Most localization algorithms are synchronized with the time frame, and it is not very easy to achieve accurate times. In [19], the author proposes a localization scheme without any time synchronization. The existing dive and rise (DNR) scheme is enhanced for the purpose of the localization process by excluding time synchronization. A specific anchor node dives vertically and broadcasts beacon messages at regular intervals to localize the sensor nodes. After a specific time, the anchor node rises vertically, broadcasting the beacon messages. This entire process allows to identify the distance between the anchor node and the nodes within the transmission area, thus estimating the nodes' position. This scheme assumes that the nodes are motionless, which is impractical.

In [20], the authors develop a multi-period particle swarm optimization (MP-PSO) algorithm that analyzes water mo-

bility patterns the seashore, for the purpose of the localization process. The beacon nodes are located, and their velocities are estimated using the range-based PSO algorithm. Initially, the spatial mobility correlation of the underwater objects (the nodes) is applied to estimate the velocity of the undiscovered nodes and, their locations are predicted thereafter. This algorithm offers more reliable localization coverage and enhanced localization accuracy. Computation complexity and energy consumption of this algorithm are relatively high.

Papers [2], [4], [8], [9] focus primarily on traditional methods used for determining node locations, neglecting undersea conditions. Their authors present numerous techniques that provide more insight into such issues as time synchronization, network lifetime enhancement, as well as mobility in localization processes, with empirical results shown, too.

Most of the existing algorithms focus on estimating the nodes' location by relying on autonomous underwater vehicles, anchor nodes using geometrical structures, but neglect the mobility of the nodes and their energy efficiency. The survey shows also that computational geometry is to relied upon while estimating node locations. There was a lack of focus on the adoption of computational geometrical fundamental approaches in localization schemes. This factor motivates us to design and simulate a geometrically-based mechanism for forming trapezoids and finding the nodes' location, with the dynamic sea conditions taken into consideration. In article [21], a review has been conducted, revealing the existing difficulties encountered in marine environments. In the review, the UWSN is introduced initially. Then, basic information concerning underwater conditions and the localization technique are discussed. After that, the article focuses on the UWSN architecture and on the technologies used for localization purposes. Several centralized and distributed localization techniques are presented in the paper. The estimation- and prediction-based localization algorithms are presented as well. The localization algorithms are grouped based on range-free and range-based schemes. Finally, the article focuses on the difficulties impacting underwater acoustic communications and underwater localization.

## 4. Proposed Work

In this section, the proposed localization scheme using computational geometry is presented. Though this work focuses mainly on localization in 3D network architectures, some issues, such as cluster creation, energy usage and topology control are intrinsic. These issues play a significant role in creating an efficient location estimation method. This section described the network architecture, the trilateration method, the agent technology, and the localization scheme under consideration.

### 4.1. Network Environment

In two-dimensional UASN, sensor nodes are grounded at the bottom of the sea. In the 3D variant, underwater sensor

nodes are deployed at various depths in order to cover the desired area. The 3D UASN that this work is concerned with consists of AUVs, ordinary uw-sensor nodes, and anchor nodes. Each node may operate in different modes. In its active state, the node operates with full functionality. In the semi-active state, the sensor node is capable of sensing and receiving signals. In the inactive state, the node is not in the operating state, i.e. its residual energy level is below the threshold value. It is assumed that uw-nodes are allowed to transmit to/from anchor/reference nodes only. The sink node controls the operation of AUV and obtains information that tasks have been performed. Some anchor/reference that are more capable than uw-sensors are randomly deployed at various sea levels and are motionless. The nodes are deployed uniformly and randomly throughout the targeted section of the sea. Each node is capable of communicating, may be anchored, and is movable. One sink node is installed onshore to control all activities performed.

The range of capabilities of AUVs is higher than in the case of uw-sensor and anchor nodes. The network model consists of a few AUVs to avoid the extra costs. Uw-sensors are deployed randomly by dropping them in the water. Uw-sensor and anchor nodes collectively make up an ad-hoc network operating on plane  $O$ . When the AUV is deployed at a certain depth and travels, and it may calculate its coordinates. In this work, the AUV helps the nodes estimate their location. Some reference/anchor nodes are employed on the seaplane to assist in the localization process. The network environment is shown in Fig. 1. The monitored area of ocean  $O$  is a planar subdivision with the size of  $O_l X O_b X O_d$ . The water is divided into many vertical levels based on the transmission range of AUV as:

$$O_{VL} = \frac{O_d}{AUV_{CR}} \quad (1)$$

At each vertical layer, AUVs are deployed at a fixed depth. AUVs are proficient in acquiring their locations directly

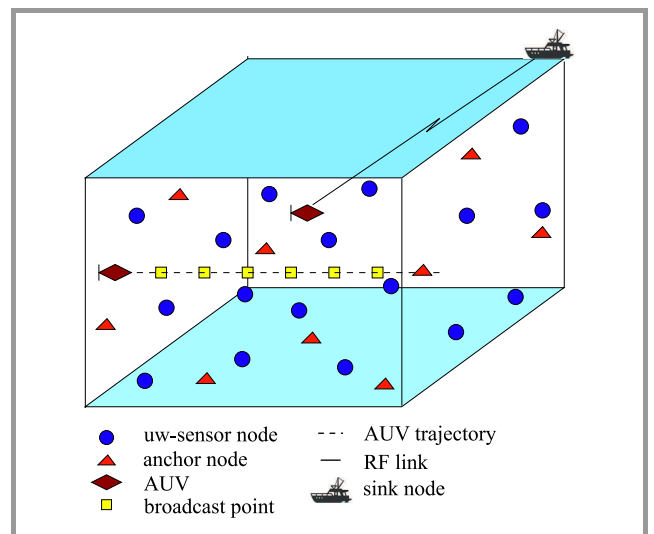


Fig. 1. The UASN network architecture.

Table 1  
 Abbreviations used

Definition	Notation
Absorption model	$\alpha(f)$
Autonomous underwater vehicle	AUV
Anchor ID	$A_{ID}$
Trapezoid ID of anchor	$A_{NT}$
Neighbors of anchor's node	$A_{NNT}$
Residual energy	$A_{ER}$
Position of anchor	$A_{(X,Y,Z)}$
AUV communication range	$AUV_{cr}$
Directive index	DI
Detected threshold	DT
Node energy threshold	$E_{th}$
Geometrical spreading factor of propagation	k
Length of the AUV's linear trajectory	L
Neighbor count	$N_C$
Node depth	$N_D$
Node ID	$N_{id}$
Node's trapezoid ID	$N_{iid}$
Node position	$N_{(x,y,z)}$
Noise level	NL
Propagation loss	PL
Source level	SL

from GPS. Assuming that the outline of each trapezoid  $T_i$  or  $T_j$  ( $i, j \leq n$ ) is disjoint without gaps and overlaps, i.e. the trapezoid is located between  $T_{i,j} \subseteq O$  and  $T_i \cap T_j = \emptyset$ , where  $i, j \leq n$ . Since the AUV may transmit in all directions, sensor nodes may be located in the upper and lower portions of its linear trajectory. Anchor/reference nodes acquire their positions whenever they are within the AUV's transmission range, by using the RSSI technique. Let us assume that the deployment of anchor nodes forms a planar graph  $G(V, E)$ , where reference/anchor nodes are the vertices, and communication edges between these nodes are the segments/edges. Table 1 presents the abbreviations used in this work.

#### 4.2. Trilateration Method

Trilateration is a process of finding position by measuring the distance using signal strengths from different sources. In a trilateration scheme, the location of a uw-sensor  $u_i$  may be found if at least three localized nodes (signal sources) or reference nodes appear in the proximity of  $u_i$ . As shown in Fig. 2a,  $L_1$ ,  $L_2$ , and  $L_3$  are three localized uw-sensors with known locations, present in the proximity of an unlocalized uw-sensor node  $u$ . It is possible to determine the distance of an object if it remains within the sensing range centered around  $L_1$  or  $L_2$  or  $L_3$ . Let  $u$  be the un-localized node with location  $(x_u, y_u)$  and let be the known locations of  $(x_{L1}, y_{L1})$ ,  $(x_{L2}, y_{L2})$ , and  $(x_{L3}, y_{L3})$ ,  $L_1, L_2$ , and  $L_3$ , respec-

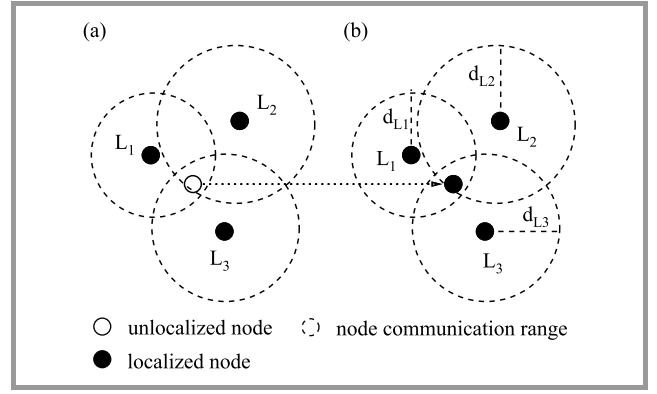


Fig. 2. Network: (a) before trilateration and (b) after trilateration.

tively. Let  $d_1, d_2$ , and  $d_3$  be distances from the unknown object, respectively. The distance equations are:

$$(x_u - x_{L1})^2 + (y_u - y_{L1})^2 = d_1^2, \quad (2)$$

$$(x_u - x_{L2})^2 + (y_u - y_{L2})^2 = d_2^2, \quad (3)$$

$$(x_u - x_{L3})^2 + (y_u - y_{L3})^2 = d_3^2. \quad (4)$$

By expanding the squares in each equation:

$$x_u^2 - 2x_u x_{L1} + x_{L1}^2 + y_u^2 - 2y_u y_{L1} + y_{L1}^2 = d_1^2, \quad (5)$$

$$x_u^2 - 2x_u x_{L2} + x_{L2}^2 + y_u^2 - 2y_u y_{L2} + y_{L2}^2 = d_2^2, \quad (6)$$

$$x_u^2 - 2x_u x_{L3} + x_{L3}^2 + y_u^2 - 2y_u y_{L3} + y_{L3}^2 = d_3^2. \quad (7)$$

From Eqs. (5)–(6):

$$(-2x_{L1} + 2x_{L2})x_u + (-2y_{L1} + 2y_{L2})y_u = d_1^2 - d_2^2 - x_{L1}^2 + x_{L2}^2 - y_{L1}^2 + y_{L2}^2. \quad (8)$$

From Eqs. (6)–(7):

$$(-2x_{L2} + 2x_{L3})x_u + (-2y_{L2} + 2y_{L3})y_u = d_2^2 - d_3^2 - x_{L2}^2 + x_{L3}^2 - y_{L2}^2 + y_{L3}^2. \quad (9)$$

Equations (8)–(9) with two unknowns are:

$$Ax + By = C, \quad (10)$$

$$Dx + Ey = F, \quad (11)$$

which gives the solution:

$$x = \frac{CE - FB}{EA - BD}, \quad (12)$$

$$y = \frac{CD - AF}{BD - AE}. \quad (13)$$

The value of the  $z$  coordinate is the depth of the node. Figure 2b shows the node after the trilateration process. In an ideal case, the intersection of three sensing ranges is the exact location of the object, i.e. node  $u$ . Once the node computes its location through trilateration, it assumes the

role of a reference node R in order to further assist in determining the location of unlocalized nodes. In many cases, distance computations are imprecise, because the sensing range circles may not intersect at a single location. To overcome this error, a maximum likelihood scheme may be adopted to minimize the degree of imprecision in determining the location of a given node.

### 4.3. Node Agency

Node agency is a critical component of each uw-node. It comprises of a static agent NA, and a mobile agent NMA – both residing at the node level. It also includes NKB to store node- and trapezoid-related information. Migrant mobile agents TFA and LA perform inter-node communications, assist in location estimation and in the trapezoid formation process. This agency is taking an active part in localization and is also partially involved in the trapezoid formation process. Node agency is shown in Fig. 3.

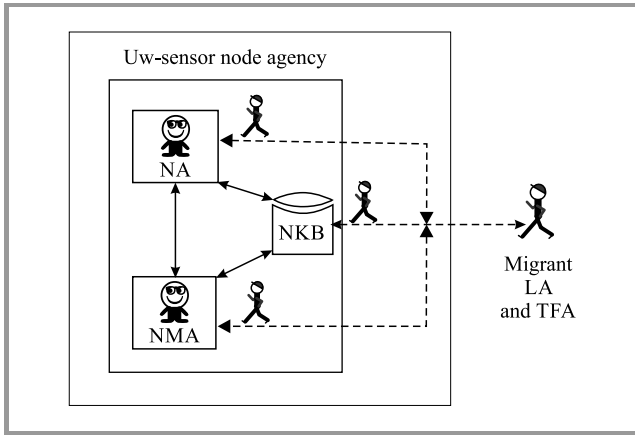


Fig. 3. Node agency.

**Node agent (NA)** is an autonomous, universal and reactive agent. NA is situated locally at the node level. NA uses NKB to store and retrieve information. NA coordinates with NMA to oversee the activities that are taking place at the uw-sensor node level. This agent communicates with LA to support the location estimation process and interacts with TFA to learn its trapezoid information. NA is responsible for learning which trapezoid it belongs to and for informing node agency when localization is required.

**Node manager agent (NMA)** is situated in each uw-sensor node of the network. NMA monitors everything that is taking place in and around the node, for taking some decisions and for performing regular activities. Activities performed at the NMA at level include the following:

- changing the node state from semi-active to active and vice-versa,
- to communicating with the outside world in order to synchronize all actions,
- becoming actively involved in the location estimation process with LA,

- effectively managing the node’s battery for longer life,
- updating the node knowledge base,
- NMA coordinates with NA, LA, and TFA to complete the tasks.

NMA decides when to estimate its location by verifying the present status of the sensor node.

**Node knowledge base (NKB)** is a local information storage existing at the level of each node. This knowledge base comprises  $N_{ID}$ ,  $N_{TID}$ ,  $N_{ER}$ ,  $N_D$ ,  $N_{(X,Y,Z)}$ , and all information observed. Local and migrant agents communicate with this information storage to store, modify and retrieve the data. The structure of the NKB is given in Table 2.

Table 2  
Node knowledge base

Sl no.	$N_{ID}$	$N_{TID}$	$N_{ER}$	$N_C$	$N_D$	$N_{(X,Y,Z)}$
1	24	4	4.6	4	203 m	–
2	5	6	4.76	2	123 m	–
3	12	3	4.32	3	174 m	–
4	–	–	–	–	–	–

### 4.4. Anchor Agency

Anchor agency comprises a static anchor agent and a mobile anchor management agent (AMA). It includes an anchor knowledge base (AKB) used to store and retrieve information concerning the trapezoids, the node, and the anchor node. Migrant mobile agents – LA and TFA – are used for inter-agent communication in order to perform localization and trapezoid formation processes. This agency plays the key role in creating trapezoids in the target area and participates in the localization process. It stores and updates information in AKB. The anchor agency is shown in Fig. 4.

**AUV agent (AA)** is an autonomous, universal and reactive agent. It is situated locally at the anchor node level. It uses AKB to store, retrieve and modify information. AA coordinates with AMA to oversee the activities that are taking place at the anchor node level. This agent actively communicates with TFA to create trapezoids. It also communicates with LA and participates in the process of estimating locations within the trapezoids. It stores, in AKB, the trapezoid ID, trapezoid boundary, number of nodes present in the trapezoid, and its association with different trapezoid IDs. AA is responsible for communicating with the sink node in order to identify any variations in the system.

**Anchor Manager Agent (AMA)** is situated within each anchor node of the network. AMA monitors all activities taking place in and around the anchor node and performs regular tasks. The activities of AMA existing at the anchor node level include the following:

- communicating with the outside world in order to synchronize all actions,

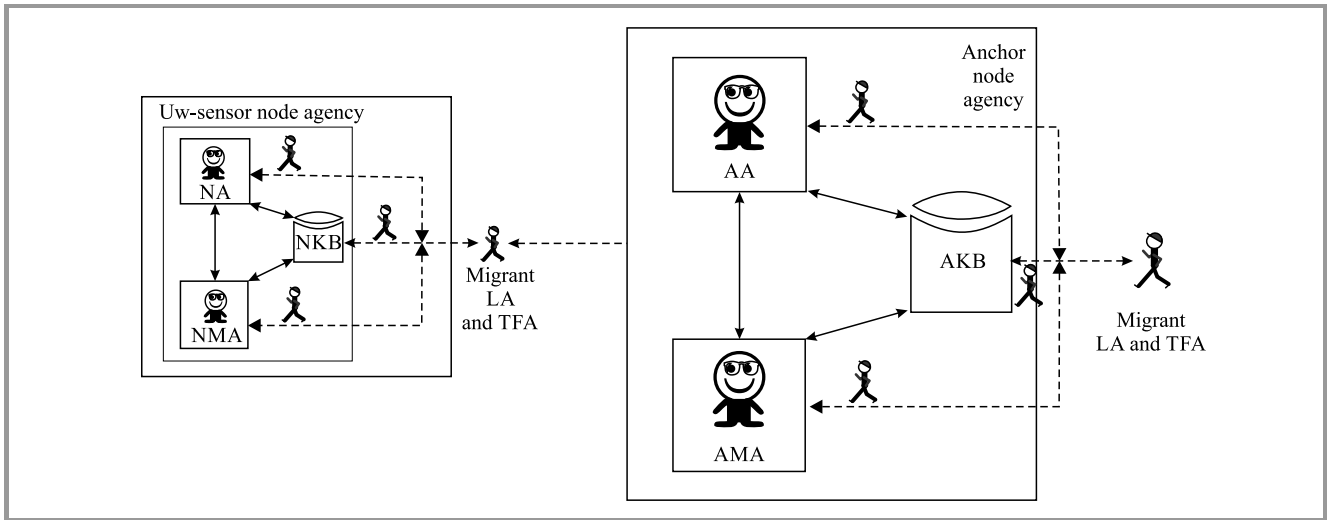


Fig. 4. Anchor node agency.

- becoming actively involved in the location estimation process with LA,
- participating actively in the creation of trapezoids with TFA,
- effectively managing the node’s battery for longer life,
- updating the anchor knowledge base,
- AMA coordinates with NA, AA, LA, and TFA to complete the tasks.

AMA informs the sink node about initiating the trapezoid formation process whenever a significant variation takes place concerning the anchor node’s location. AMA keeps on updating its position and battery information to the sink node at regular intervals.

**Anchor knowledge base (AKB)** is a local information storage at each anchor node level. This knowledge base contains  $A_{ID}$ ,  $A_{NT}$ ,  $A_{NNT}$ ,  $A_{ER}$ ,  $A_{(X,Y,Z)}$ ,  $N_C$ , and all observed information. Local and migrant agents communicate with this information storage to store, modify and access the data. The structure of NKB is shown in Table 3.

Table 3  
Anchor knowledge base

Sl no.	$A_{ID}$	$A_{NT}$	$A_{NNT}$	$A_{ER}$	$A_{(X,Y,Z)}$
1	3	2	5	4.00	–
2	5	3	6	3.47	–
3	14	1	2	4.72	–
4	–	–	–	–	–

4.5. Sink Agency

Sink agency comprises a static sink management agent (AMA), as well as TFA and LA mobile agents. It uses SKB to save and access information about the entire network.

LA and TFA mobile agents are triggered to perform localization and trapezoid formation processes. Sink agency is the central agency that initiates the trapezoid creation process and the location estimation process. It stores and updates the information in SKB. Anchor agency is shown in Fig. 5.

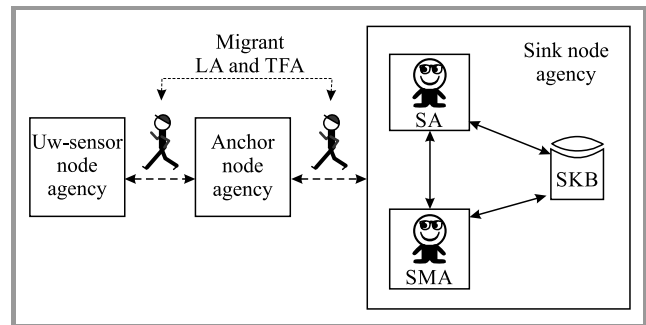


Fig. 5. Sink node agency.

**Sink Agent (SA)** is an autonomous, universal, adaptive, smart and proactive agent. It is situated locally at the sink node level. It triggers and coordinates LA for localization TFA for trapezoid formation process. It utilizes SKB to save and access information. Sink node communicates with other agencies and agents to accomplish the desired activities, as and when required for the network. The trapezoid formation process is performed for the entire targeted area. On-demand single node or all node localization is performed as and when needed.

**Localization Agent (LA)** is an autonomous, social, proactive and mobile agent. It interacts with all agents and agencies to collect the required information and to accomplish the localization process. LA is initiated by the sink node to accomplish the on-demand single node or all node localization process and updates the data in all information storages.

**Trapezoid Formation Agent (TFA)** is a mobile, self-sufficient, proactive and social agent. The sink node triggers TFA, and its primary objective is to create trapezoids and to construct SDS for a given network. It communicates with all agents and agencies to gather the required information and to accomplish the trapezoid formation process. It creates SDS during the creation of trapezoids. SDS is a tree-based data structure that is better suited for the location of trapezoids.

**Sink Manager Agent (SMA)** is situated in the network, at the sink node. Its duties include the following:

- communicating with other components of the system and synchronizing the actions,
- intimate sink agent to activate TFA through pre-localization LA, while the localization, and maintain SDS,
- associate in the location estimation process with LA and trapezoid creation process with TFA,
- SMA manages, virtually, the batteries of the uw-sensor and the anchor nodes, increasing their life,
- updating the SKB at regular intervals.

**Sink Knowledge Base (SKB)** is the sink node’s information storage, accessible to TFA and LA mobile agents during the trapezoid formation and localization process. This knowledge base contains information on the energy level of the entire network, on AUV’s trajectory, on trapezoid information, as well as on the number of active and failed nodes, as shown in Table 4. SA, SMA, LA, and TFA communicate with this information storage to retrieve, modify and store information.

Table 4  
Sink knowledge base

SN	$A_{ID}$	$N_{ID}$	$N_{TID}$	$N_{ER}$	A/F	Trajectory info
1	1	5	3	4.56	3/0	40 m, up
2	4	13	7	3.57	4/1	70 m, down
3	3	16	5	4.89	0/1	110 m, up
4	–	–	–	–	–	–

**4.6. Formation of Trapezoids**

The sink node begins the process of creating clusters with the support of TFA and AUV. AUV is deployed at fixed depth levels of the ocean and traverses across the linear trajectory. At each level of the linear trajectory, TFA activates the trapezoid formation model to divide the horizontal plane into many vertical slabs whenever the anchor nodes come within the transmission range of AUV, and it stores the anchor nodes’  $x$  coordinate in a structured manner on the array, to create SDS. TFA divides each vertical slab further into trapezoids, with the assistance of reference/anchor nodes. Each area of the vertical slab between two

consecutive edges forms a unique trapezoid. Some trapezoids border on the seafloor and on the sea surface within the bounding box boundary regions. Vertical lines and the anchor nodes’ edges passing through the endpoints create geometrical shapes such as trapezoids, unbounded trapezoids and triangles, as shown in Fig. 6.

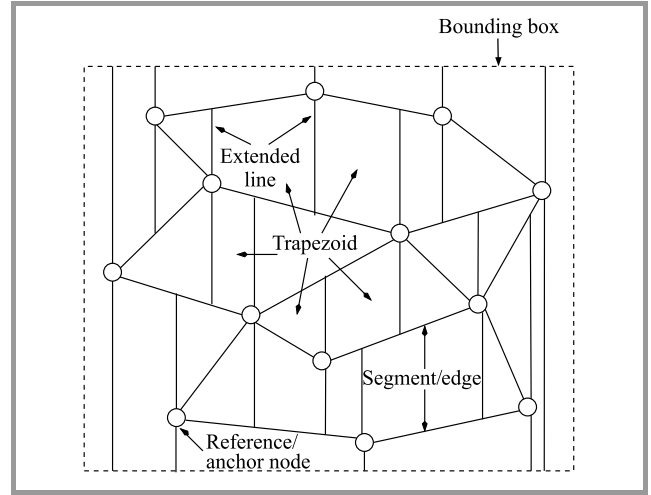


Fig. 6. Trapezoidal map.

A binary search is performed to determine the trapezoid of the uw-sensor node, and  $x$  coordinates are stored in the array, as shown in Fig. 8 [22]. Provisionally, the diagram contains a set of non-crossing line-segments,  $S = \{s_1, s_2, \dots, s_n\}$ , embedded in the bounding box  $R$  and characterized by the fact that any two anchor nodes have different  $x$  coordinates. If the arrangement comprises a set of non-crossing edges having different anchor nodes’  $x$  coordinates and surrounded by fixed limits, then the process of creating a trapezoidal map is more straightforward. TFA creates the trapezoidal map  $T(S)$  using the non-crossing edges of the anchor nodes on the ocean’s surface. TFA enlarges two perpendicular edges from each anchor node, one in the ascending direction and the other in the descending direction, until they reach either the edge or the border of  $S$ , as shown in Fig. 7 of the trapezoidal map. In a scenario

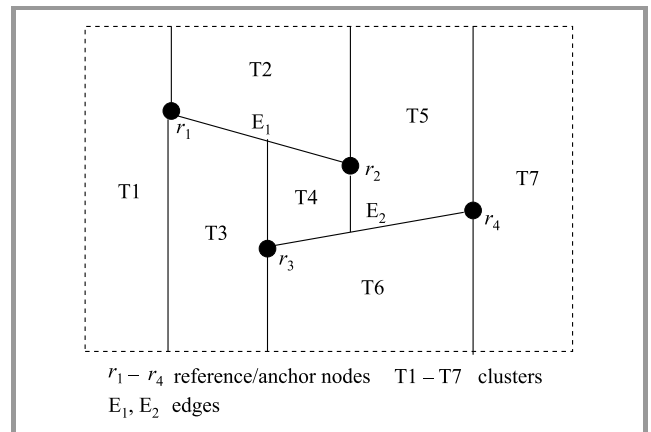


Fig. 7. Two segments trapezoidal map.

in which any two trapezoids are located next to each other, then such trapezoids share a perpendicular edge. A double connected edge is used in the formation of the trapezoidal map.

During the process of creating the trapezoids, TFA develops SDS  $D$ , as shown in Fig. 8. Its properties are:

- SDS is a directed-acyclic-graph (DAG),
- SDS is a single-rooted, and each trapezoid is rendered by a leaf node in the trapezoidal-map of  $S$ ,
- inner nodes' out-degree is two:  $x$ -node and  $y$ -node, where  $x$ -node shows with the endpoints of segments in  $S$  and  $y$ -node represents the segment itself.

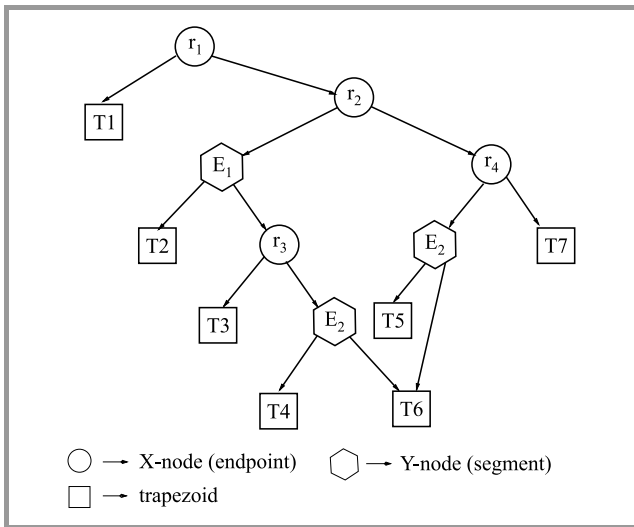


Fig. 8. Search data structure.

**Algorithm 1.** Trapezoidal map

**Input:** Set  $S = s_1, s_2, \dots, s_n$  where  $s$  is the non-crossing line segment between the nodes.

**Output:** trapezoidal map, data structure  $D$

- 1: **Function** TMAP(V)
- 2: Define the network environment and initialize the data structure
- 3: **While**  $k = 2$  **downto** 2 **do**
- 4:      $randomindex = \text{Random}(k)$
- 5:     Exchange  $S[k]$  and  $S[randomindex]$
- 6: **End while**
- 7: **For** all segments/edges in the network **do**
- 8:     Find the set of trapezoids that are properly intersected by each segment
- 9:     Remove some of the trapezoids to replace the new trapezoids which are appearing because of the insertion of the segment
- 10:    Remove the leaves from the data structure and add the leaves for new trapezoids
- 11: **End for**
- 12: **End function**

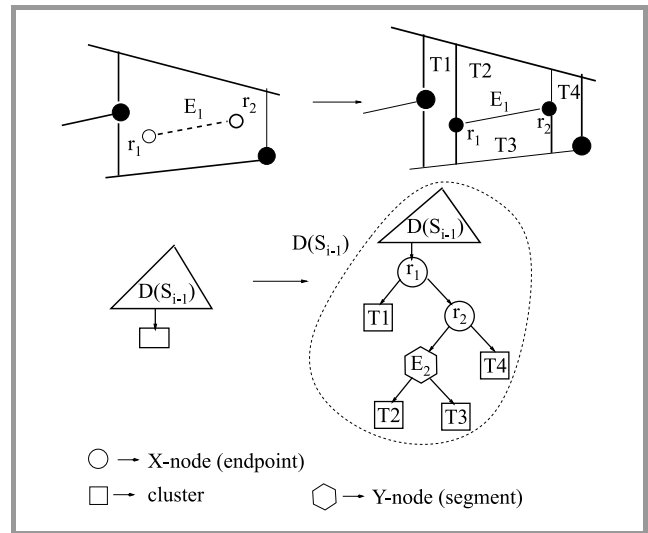


Fig. 9. Data structure used for adding a new segments by replacing trapezoids.

The trapezoidal map and SDS are interlinked with each other. Algorithm 1 describes the process of constructing the trapezoidal map the network. When two anchor/reference nodes, such as  $r_1, r_2$ , are positioned entirely in any of the trapezoids, TFA removes some trapezoids and replaces them with new trapezoids, as presented in Algorithm 1, and the related search data structure is constructed as shown in Fig. 9 [22].

**4.7. AUV Trajectory**

The AUV moves along the continuous trajectory at distance  $l$  from the initial position  $T_{start}$ , until the end position  $T_{end}$ . It moves horizontally, at fixed underwater levels, at a constant speed. At each depth, AUV periodically transmits, omnidirectionally, beacon messages including real-time position information. It does so at fixed intervals and with full communication power, as depicted in Fig. 10. The migrant LA activates the localization model at each

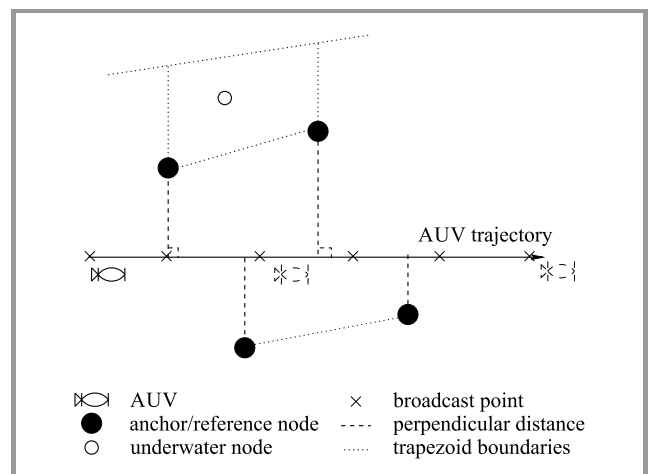


Fig. 10. The trajectory of AUV.

---

**Algorithm 2.** Localization of un-localized underwater nodes within the trapezoid at the second level

---

```

1: Function UWNLocalize( $t, D, \text{trap}[]$ )
2: If one unlocalized node in  $\text{trap}[]$  & in the communication range of anchor node then
3:   Compute localization by using the RSSI method
4: else
5:   If more than one unlocalized nodes are there in  $\text{trap}[]$  then
6:     Get at least 3 localized node's information in the trapezoid
7:     Compute localization using trilateration
8:     Update SKB and NKB
9:   else
10:    If the node is not in the range then
11:      Defer localization until next iteration
12:    End if
13:  End if
14: End if
15: Foreach node  $j$  in the  $\text{trap}[]$  do
16:   Compute energy consumption of node  $N_{ER}(j)$ 
17:   If  $N_{ER}(j) \leq E_{th}$  then
18:      $N_{failure} = N_{failure} + 1$ 
19:     Change the node  $N_j$  state into inactive
20:   End if
21: End for
22: Update SKB and NKB
23: End function

```

---

anchor node to receive beacon messages and calculates the received-signal-strength (RSS) of each beacon message. LA estimates the received RSS value in the network environment as:

$$R_{SL} = SL + NL - PL(l) , \quad (14)$$

where  $SL$  is the source level,  $NL$  is the noise level,  $PL(l)$  is the propagation loss for an acoustic signal in underwater conditions, given as:

$$NL(f) = N_{tn}(f) + N_w(f) + N_s(f) + N_{tu}(f) \text{ [Pa/Hz]} , \quad (15)$$

$$SL = 10 \log \frac{I_t}{1 \mu Pa} , \quad (16)$$

where  $I_t$  is the the intensity of the signal transmitted from the broadcast point, at a distance of 1 m measured in  $\mu Pa$ . The  $I_t$  yield as per [24] is:

$$I_t = 10^{\frac{SL}{10}} \cdot 0.67 \cdot 10^{-68} \quad (17)$$

in watts/m<sup>2</sup>. The propagation loss is:

$$10 \log PL(l, f) = k \cdot 10 \log(l) + l \cdot \alpha(f) + A , \quad (18)$$

where  $k$  is the geometrical spreading constituent of the distribution,  $\alpha(f)$  is the absorption pattern shown in Eq. (19), and  $A$  is the communication irregularity that eliminates con-

---

**Algorithm 3.** Localization of unlocalized anchor nodes at the first level

---

**Input:** search data structure  $D$ , trapezoid information  $T$   
**Output:** network with localized nodes

```

1: Function ( $D, T$ )
2: Get network environment, data structure  $D$ , trapezoid map  $T$ 
3: loop = 1,  $N_{failure} = 0$ ,  $N_{ER} = 5.0$   $\triangleright$  measuring unit is Joule
4:  $AUV_{CR} = 60$ ,  $N_{CR} = 30$ ,  $N_{SR} = 20$   $\triangleright$  measuring unit is meter
5: While  $N_{failure} \leq N - \frac{LP}{100} \cdot N$  do  $\triangleright$  Number of failed nodes below LP%
6:   Sink begins the location estimation process by triggering LA.
7:    $AUV_d = 100$   $\triangleright$  Initially, AUV depth is set to 100 m
8:   While  $AUV_d \leq O_d$  do  $\triangleright$  Considered depth of the ocean boundary
9:     Change all the nodes' state into a semi-active state
10:     $T_{start} = 0$ ,  $T_{end} = 800$ 
11:    Install AUV at  $AUV_d$  [m]
12:     $B_{point} = 30$   $\triangleright$  The initial broadcast point on a linear trajectory
13:    While  $B_{point} \leq T_{end}$  do
14:      AUV announces beacon message  $bm$  at  $B_{point}$ 
15:      For each anchor node  $A_i \leq AUV_{CR}$  do
16:        LA at anchor node calculates the signal strength of received beacon message
17:        Anchor node estimates its location
18:        Calculate power consumption and update  $N_{ER}$ 
19:         $\text{trap}[] =$  find the trapezoids associated with  $A_i$ 
20:        uwnLocalize ( $A_i, D, \text{trap}[]$ )  $\triangleright$  perform localization within the trapezoid
21:      End for
22:       $B_{point} = B_{point} + 30$   $\triangleright$  Advance to next broadcast point
23:    End while
24:     $AUV_d = AUV_d + 200$ 
25:  End while
26:  loop = loop + 1  $\triangleright$  Total number of localization processes for the whole network
27:  Find the failed nodes in the network
28: End while
29: End function

```

---

sumption factors and involves the refraction, diffraction, and scattering.

In general, the spreading factor of  $k = 1.5$  is assumed in this work. Spreading loss is wavelength-independent, and it has the rounded or cylindrical spreading.

Thorp's formula [25] describes  $\alpha(f)$  – frequency absorption model as:



$$\alpha(f) = \left( 0.11 \frac{f^2}{f^2 + 1} + 44 \frac{f^2}{f^2 + 4100} + 2.75 \cdot 10^{-4} f^2 + 0.003 \right) \cdot 10^{-3}. \quad (19)$$

Consider any announcement position is  $(x, y, z)$  along the AUV's linear path at each depth level, and  $(x_r, y_r, z_r)$  being any anchor node position on the ocean's surface.  $z$  is 0, and the  $y$  coordinate is linearly expressed by  $x$  due to the AUV's path, which is linear on the ocean's surface. LA gets the RSSI value vector of all announcement points and the  $x$  coordinate vector of the announcement points and estimates the position of an anchor node by using RSSI. Once the reference/anchor nodes have learned their locations, LA visits each trapezoid and calculates the location of unlocalized nodes, as described in Algorithm 2. Algorithm 3 describes the process of estimating the location of nodes.

#### 4.8. Single-node Localization

If a node moves within the trapezoid due to underwater currents or other aquatic characteristics, then NA may demand localization by asking the anchor node. The anchor node initiates the location estimation process by triggering LA and the procedure is given in Algorithm 4.

---

#### Algorithm 4. On-demand single-node localization

---

```

1: Function SN Localization( $N_{ID}$ )
2:   The node realizes the need for location estimation
3:   Uw-sensor transmits a request message to the anchor
   node about the need for localization
4:   Anchor node informs the sink node about the ini-
   tiation of the localization process and provides
   node details
5:   Anchor triggers LA to initiate the localization pro-
   cess
6:   LA gets the information of  $N_{ID}$  and anchor node of
    $N_{ID}$ 
7:   LA gets the trapezoid-id of  $N_{ID}$  using search-data-
   structure
8:   LA visits to trapezoid-id for localization
9:   If LA finds at least 3 localized nodes (including an-
   chor node) within the communication range of  $N_{ID}$ 
   in the trapezoid then
10:     LA estimates the location of  $N_{ID}$  using the tri-
     lateration technique
11:   else
12:     If LA finds  $N_{ID}$  is within the communication
     range of anchor node then
13:       LA estimates the location of  $N_{ID}$  using RSSI
14:     else
15:       Defer the location estimation process until the
       next trapezoid formation process.
16:     End if
17:   End if
18: End function

```

---

The sink node initiates all-node localization at regular intervals. The scheme is as below:

1. The sink node begins the trapezoid formation activity at each iteration by TFA. TFA divides the region into perpendicular slabs and further divides these into trapezoids. TFA counts the number of localized and unlocalized nodes present in each trapezoid. TFA stores relevant information in SKB, i.e. information storage of the sink node, and also creates search data structure  $D$ .
2. The sink node begins the localization process through LA and deploys AUV at various depth levels. AUV traverses along the linear trajectory from starting point  $T_{start}$  to endpoint  $T_{end}$  at each depth, with a constant speed. AUV transmits beacon messages including real time location information at fixed distances and with a fixed transmission power, as depicted in Fig. 10. At the anchor node, the LA receives these messages and executes the localization model to estimate its location.
3. The anchor agent at each anchor node initiates the localization process in its assigned trapezoids based on the data given by TFA and SDS  $D$ .
4. At each trapezoid, LA performs the localization process in the following manner:
  - if the node is already localized, then LA updates the localization knowledge base with such information as uw-sensor node ID, uw-sensor node energy level, trapezoid ID, adjacent trapezoids, etc. LA changes its state from semi-active to active;
  - if the node is unlocalized, then LA looks for at least three localized nodes which are there in the trapezoids, within the communication range, completes the localization process by using the trilateration technique and changes the node status into active;
  - if the uw-sensor node is unlocalized and it is within the communication range of the anchor node, then LA applies the RSSI method to estimate its location;
  - if an unlocalized uw-sensor node exists in the trapezoid and it is out of the communication range of the anchor node and of other nodes, then the localization process is deferred until the next iteration;
  - the above steps are repeated to localize other nodes in the trapezoid. LA changes the state of all localized nodes from semi-active to active.
5. LA updates location-related information in SKB, AKB, and NKB for future use.

6. Steps 1–5 are repeated until AUV reaches  $T_{end}$  of each linear trajectory.
7. AUV is deployed at the next vertical level and repeats steps 1–6 to cover the entire targeted area.
8. At the end of each localization period, all the underwater sensor nodes change their status to semi-active in order to preserve their energy levels.

Algorithm 2 describes the localization process within the trapezoids.

#### 4.9. Mobility in the Localization Problem

Movement of the nodes is unavoidable due to underwater currents and other underwater conditions. Each NA maintains NKB, containing such information such as energy level, neighbor count and location points. The movement of a node is severe in shallow waters due to numerous human activities and unpredictable behavior of the sea environment. On the contrary, in deep water, most of the time, the movement of the nodes is not present at all or is very much restricted. The agent may perform self-localization in deep water by itself, provided the node is in communication with at least one node which knows its location. If node A is already localized with  $N_{A(x,y)}$  points and if NA observes that the node has changed its position, then LA at the node performs re-localization, with the process explained below:

1. LA obtains the location of the previous uw-sensor node from the NKB and stores it as  $NP_{A(x,y)}$ , and  $NP_{A_{depth}}$  (i.e. NP is the previous location of the node).
2. LA computes the distance to the uw-sensor node, i.e.  $N_{dist} = N_{speed} \cdot N_{\delta t}$ , where  $N_{\delta t}$  is the time difference between the last localized time and the agent's observation time,  $N_{speed}$  is the speed of the uw-sensor node,  $N_{dist}$  is the distance which is scalable. The current position of the node is calculated as:
  - assign  $NC_{A_{depth}} = \text{Get}(N_D)$ , NC is the current location of the uw-sensor node,
  - compute  $d = NP_{A_{depth}} - NC_{A_{depth}}$ ,
  - test if  $(d \leq 0)$  and then  $NC_{A_y} = NP_{A_y} + d$ , i.e. the node is moved downwards down,
  - test if  $(d \geq 0)$  and then  $NC_{A_y} = NP_{A_y} - d$ , i.e. the node moved upwards.
3. Now, the location of mobile node A is  $(NC_{A_x}, NC_{A_y})$ , where the  $x$  coordinate is unknown. The distance formula may be applied to find out the  $x$  coordinate if the mobile node is capable of communicating with at least one localized uw-sensor node, i.e. node B with location  $(NC_{B_x}, NC_{B_y})$ .
4. Find distance  $D$  between nodes A and B using RSSI.
5. RSSI = antenna gain + transmit power – path loss.

6. For non-mobile nodes A and B, antenna gain and transmit power are both constant. Path loss is the function of distance  $d$ . Hence,  $\text{RSSI} = f(d)$ ,  $d = f'(\text{RSSI})$ .
7. For simplicity, consider node A points as  $(x_1, y_1)$  instead of  $(NC_{A_x}, NC_{A_y})$  and node B points as  $(x_2, y_2)$  instead of  $(NC_{B_x}, NC_{B_y})$ . Calculate the unknown  $x_1$  value by:

$$d = \sqrt{(x_2 - x_1)^2 + (y_2 - y_1)^2} . \quad (20)$$

By taking a square on both the sides, we get:

$$d^2 = (x_2 - x_1)^2 + (y_2 - y_1)^2 , \quad (21)$$

and:

$$d^2 - (y_2 - y_1)^2 = (x_2 - x_1)^2 , \quad (22)$$

where  $d, y_1, y_2$  are known values. After solving RHS, a constant value  $v$  becomes:

$$v = (x_2 - x_1)^2 . \quad (23)$$

After removing the square on both sides Eq. (23) becomes:

$$\sqrt{v} = (x_2 - x_1) , \quad (24)$$

then:

$$x_1 = x_2 - \sqrt{v} . \quad (25)$$

Now, the  $x$  coordinate of node A is computed and the  $y$  coordinate is computed in Step 2.

8. The agent performed internal localization, and the new coordinates of mobile node A are  $(NC_{A_x}, NC_{A_y})$ .

The proposed work highlights the use of computational geometry for estimating the location of unlocalized nodes. It is supported by agent technology, which supports various APIs for during the implementation phase. Modules for trapezoid creation, SDS establishment and trajectory path formation are designed using mathematical models and may be implemented with suitable modifications. Anchor/reference nodes are considered at each stage of the proposed work, and are therefore included in trapezoid creation, trajectory path formation, SDS creation and location estimation modules. Regular nodes predominantly included in location estimation and mobility modules.

## 5. Simulation

The proposed uw-sensor node localization method is simulated and assessed based on various parameters. At the initial stage of the simulation, all nodes are considered to be characterized by equal power, equal sensing range and equal transmission capability. The sink node switches all nodes into semi-active state to preserve energy. The node location estimation process is performed iteratively. At each step,

most of the nodes attempt to localize themselves and consume energy. The simulation is terminated when the energy level of 70% of all nodes falls below a specific threshold value. Simulation models, procedures and performance parameters are discussed in this section.

### 5.1. Simulation Model

A monitored area with the size of  $600 \times 600 \times 600$  m is used for UASN simulation purposes. Initially, uw-sensor nodes are deployed randomly, beginning with 20 and with their number increasing to 100 within the 3D space. Initially, the sink node deploys AUV at  $AUV_d$  and it then moves along a continuing trajectory. AUV broadcasts location information at regular intervals, 5L is set to 30 m. At each vertical level, AUV travels linearly over a distance of 600 m, with fixed frequency  $T_f = 24$  kHz, sound level SL = 100 dB and spreading factor  $k = 1.5$ . A few anchor nodes are deployed randomly. A beacon message advances linearly at a velocity of one m/s and makes announcements one second intervals. The sink node is installed onshore. In the propagation model, sensing range  $N_{SR}$ , communication range  $N_{CR}$  of an acoustic UASN node for single hop communication and attenuation factor  $\alpha(f)$  are given in Eq. (19), as per Ainslie and McColm [26].

Table 5  
Simulation input data

Parameter	Value
Width $w$	600 m
Length $l$	600 m
Depth $d$	600 m
Uw-sensor nodes $n$	100
Uw-sensor node communication range $N_{CR}$	30 m
Temperature range	2–20°C
AUV communication range $AUV_{CR}$	60 m
Anchor nodes	30
Transmission frequency $T_f$	24 kHz
Attenuation $\alpha$	0.01–1.0
SL	100 dB
$\delta L$	30 m
Speed of ship $v$	5 m/s
$k$	1.5

The performance parameters are:

**Localization ratio.** It is the ratio of localized uw-sensor nodes to the total number uw-sensor nodes in the network.

**Energy consumption.** It is calculated as total power consumption of all nodes in one iteration. To obtain intensity  $I_t$  with communication power  $P_t$  at an interval of 1 m from the origin towards the recipient as per [24], the following equation is used:

$$P_t = 2\pi D/t \cdot 1 \text{ [m]}, \quad (26)$$

in watts, where  $D$  is the depth measured in meters and  $I_t$  is taken from Eq. (17).

In each trapezoid, power consumption of  $m$  localized uw-sensor nodes involved in the trilateration of packet size  $P_{size}$ , is:

$$P_c = \frac{mP_{size}}{m1024} = \frac{P_{size}}{1024} \quad (27)$$

in watts/bit. Assume  $T_{active}$  is the total active time of a uw-sensor node's transceiver in seconds, per one iteration,  $N_{ER}$  is the residual energy available at every uw-sensor node in w/h. The ratio of the total residual energy to the power required for one packet is the total active time of the transceiver and is given by:

$$T_{active} = \frac{N_{ER}}{P_c}. \quad (28)$$

Since the uw-sensor node operates in different states, its transceiver's active period equals  $A$  seconds, and the node's battery life is given by:

$$T_{lifetime} = \frac{T_{active}}{T_{active}} \cdot \frac{A}{24 \cdot 60} \text{ [days]}. \quad (29)$$

**Localization accuracy.** It's the difference between the original and the estimated location. If  $NE_{(x,y,z)}$  is the calculated location of node and  $NA_{(x,y,z)}$  is the original location, localization accuracy is given as:

$$LE = |NE_{(x,y,z)} - NA_{(x,y,z)}|. \quad (30)$$

The average location error is:

$$LE_{avg} = \frac{1}{n} \sum_{i=1}^n LE_i. \quad (31)$$

The location error is a vital factor if it is larger than a specified threshold value.

**Network lifetime.** It is the number of times the location estimation process is performed until the energy level of 70% of the deployed uw-sensor nodes falls below a specified threshold value. To calculate it, we need to first obtain the number of uw-sensor nodes  $m$  whose power level is greater than the threshold value, i.e. the number of nodes  $m$  if  $(T_{lifetime}(i) \leq E_{th})$  for every node  $i$  in the system. To ensure the network is connected, let  $P_N$  be the percentage share of uw-sensor nodes whose energy level is higher than the threshold value. Here,  $T_{lifetime}$  is the total lifetime of a uw-sensor node:

$$N_{stable} = \frac{P_N}{100} \cdot n, \quad (32)$$

if  $m \geq (n - N_{stable})$ , the network fails. The location estimation process is repeated after a specific condition is satisfied.

### 5.2. Simulation Procedure

The proposed MASD scheme relies on specific simulation parameters and the simulation process is repeated until 70%

of the uw-sensor nodes retain energy levels that are higher than a specific threshold value. Algorithm 5 presents the simulation procedure using pseudo-code.

**Algorithm 5.** Simulation procedure

- 1: **Function** Simulation
- 2: Setup the network system
- 3: Initialize agencies, nodes, state, knowledge base
- 4: Defining the AUVs trajectory
- 5: Formation of trapezoids by TFA over defined ocean volume.
- 6: **While** energy of 70% of nodes higher than specified threshold **do**
- 7:     AUV moves along a fixed linear path
- 8:     AUV announces beacon messages containing real-time location
- 9:     Anchor nodes re-localize themselves
- 10:    LA begins location estimation process at each trapezoid
- 11:    LA stores the necessary data in the knowledge-bases
- 12: **End while**
- 13: Convert uw-sensor node status into a semi-active state after localization
- 14: **End function**

**6. Analysis of Results**

In the proposed scheme, the algorithm is focused on creating trapezoids with the help of an internal search data structure. Figures 11 and 12 show the number of trapezoids created with a fixed number of 40 and 80 uw-sensor nodes, respectively. A higher number of trapezoids is observed in shallow waters, due to the denser deployment of uw-sensor nodes. In a scenario with a lower number of reference nodes, the formation of trapezoids is restricted due to greater gaps between the positions of reference nodes. If the number of reference nodes is increased, the number of trapezoids of various sizes present in the network increases as well. In the case shown in Fig. 12, it is observed that a higher number of trapezoids is created because

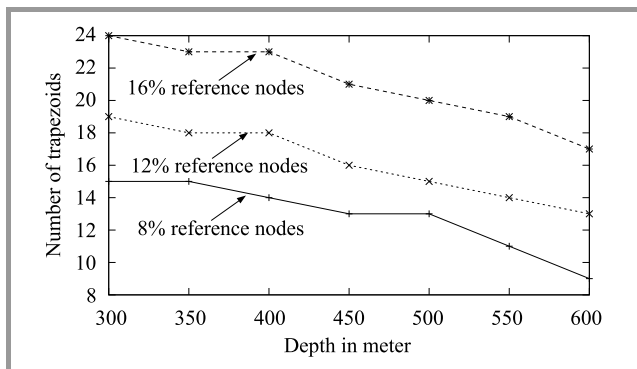


**Fig. 11.** Number of trapezoids created for 40 nodes at various depths.

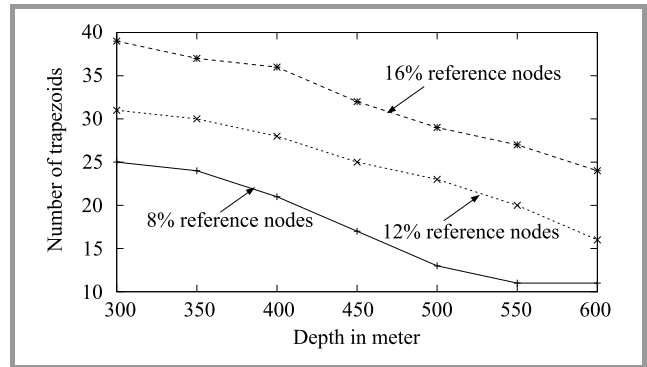


**Fig. 12.** Number of trapezoids created for 80 nodes at various depths.

of the deployment of more uw-sensor nodes. If more trapezoids are created, the lifetime of the network is affected, but it becomes easier to localize uw-sensor nodes. The sink node also participates in the creation of SDS, as shown in Fig. 8.

**6.1. Localization Accuracy**

Figure 13 shows that the location error is higher in the case of the LDB scheme than in the proposed scheme. In the recommended scheme, agents broadcast beacon messages

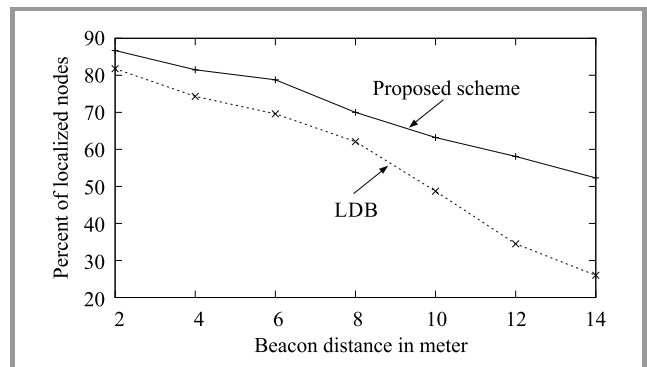


**Fig. 13.** Localization accuracy.

at regular intervals of variable beacon distance. In the proposed scheme, the size of the trapezoid is measurable and is well defined by anchor nodes, making it easier to localize the unlocalized nodes with a minimum error rate. The SDS identifies the node’s nearest trapezoid to which it belongs. This reduces the error in the actual location and the calculated location. If the beacon distance keeps increasing, the error in the computed position increases as well, as observed in the proposed scheme. Acoustic waves propagate spherically, making them vulnerable to attenuation. Hence, the position of sensor nodes is estimated with a minor error rate. Location estimation depends also on the nodes’ movement in the undersea environment, caused by water currents. In this calculation, the mobility factor is not taken into consideration.

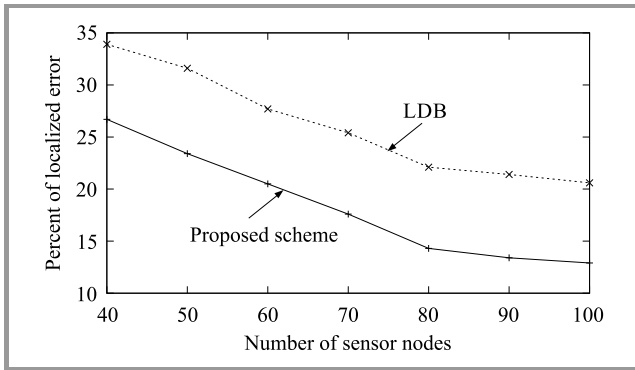


Fig. 14. Localization error.

Figure 14 shows the impact of the change in the number of uw-sensor nodes on the localization error. The proposed scheme renders better results in terms of minimizing the localization error, even if the number of nodes increases. It results in a higher level of availability of nodes in each trapezoid, which facilitates trilateration. It is observed that the sufficient availability of nodes in each trapezoid reduces the localization error. Such an approach consumes more power due to excessive communication between the nodes. It is observed that the location error does not varies much in the event of an increase in the number of uw-sensor nodes beyond a specific limit value.

6.2. Network Lifetime

Figure 15 shows network lifetime as a function of active nodes in the network. Network lifetime for the proposed MASD scheme is better than in the LDB method. In a scenario with a higher number of reference nodes, network lifetime is shorter due to the fact that the nodes are involved, on numerous occasions, in the location estimation process. Once the nodes have been localized, then their status needs to be changed to semi-active in order to improve network endurance. In the case of fewer reference nodes, network lifetime is comparatively better than in the case of other schemes. Nodes positioned in shallow water are more mobile due to the presence of water currents and require frequent localization, which reduces network lifetime.

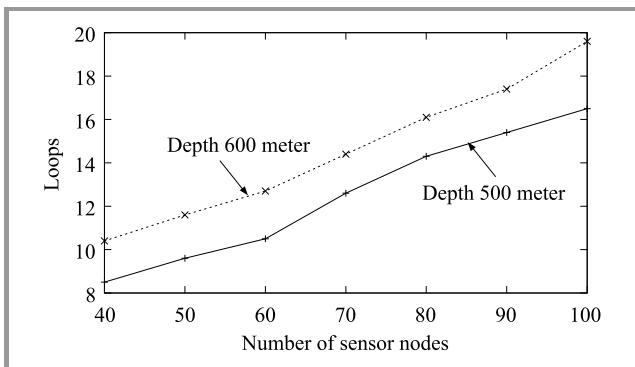


Fig. 15. Network lifetime.

6.3. Localization Ratio

As depicted in Fig. 16, the localization ratio depends, to a higher degree, on the deployment of reference nodes within the undersea network. The location estimation ratio improves linearly with an increase in the number of reference nodes. The proposed MASD scheme proves that more non-localized uw-sensor nodes are then localized in large numbers and, hence, the localization ratio is better than in the LDB scheme. In the proposed method, many trapezoids are formed and each reference node has a common vertex with several trapezoids. Therefore, each reference node is participating in the location estimation process with its dependent trapezoids. In larger structure trapezoids, it is not easy to localize unlocalized nodes because of the transmission range of reference nodes, which causes a reduction in the localization ratio. However, trapezoidal map and the search data structure allow the proposed scheme to achieve a better localization ratio.

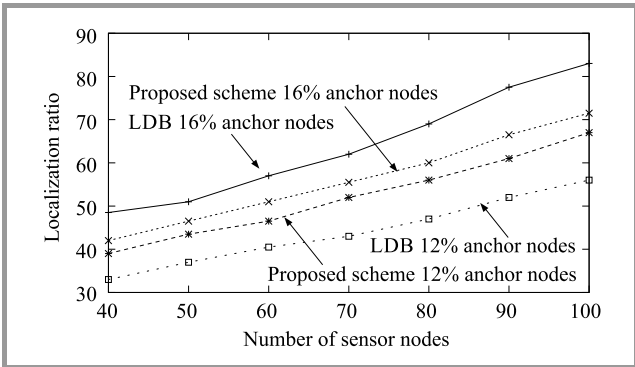


Fig. 16. Localization ratio.

6.4. Energy Consumption

Energy consumption of the presented scheme is lower, in the case of a small number of reference nodes, than in other schemes (Fig. 17). The proposed MASD scheme depletes more power (compared to the LDB scheme) in a scenario with more reference nodes because of the unnecessary participation of nodes in the location estimation process. Sensor nodes near the ocean’s surface are mobile and require frequent localization, which causes an increase

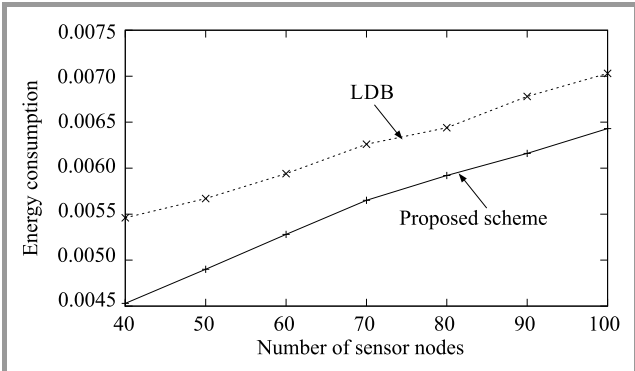
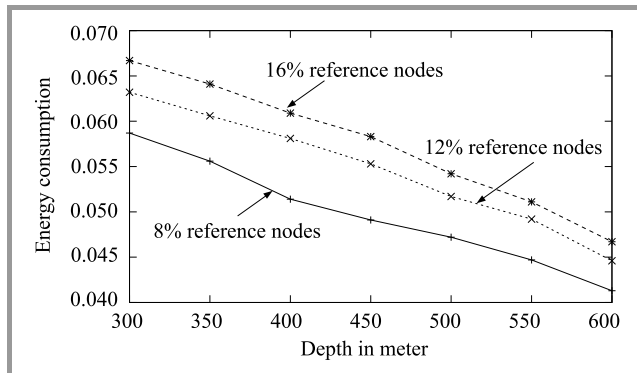


Fig. 17. Localization energy.

in power consumption. At higher depth levels, mobility of uw-sensor nodes is restricted and, hence, frequent localization of uw-sensor nodes is not required. The graph below shows energy consumption with several nodes.



**Fig. 18.** Energy consumed by nodes in each trapezoid for 40 nodes.

Figure 18 presents the amount of energy consumed by uw-sensor nodes in each trapezoid, at various depth levels, for a fixed number of 40 uw-sensor nodes. At the depth of 300 m, the reference nodes form several trapezoids of variable sizes. This means that more nodes are present in each of the trapezoids and that many nodes are involved in the localization process. The recursive involvement of nodes in the localization process leads to higher power consumption. If the depth is increased further, the number of trapezoids formed decreases and fewer uw-nodes are present in such trapezoids. Redundant involvement of the nodes in the localization process is minimized and energy consumption of the nodes decreases, as shown in the graph.

Figure 19 shows the energy dissipated by uw-sensor nodes in each trapezoid, with changing water depth and a fixed number of 80 nodes. In shallow water, reference nodes form some trapezoids of variable sizes. The scenario evolves into one characterized by higher density of nodes in each of the trapezoids, with a higher number of nodes involved in the localization process, compared to Fig. 18. The recursive engagement of nodes in the localization process drives power dissipation, which is higher than that

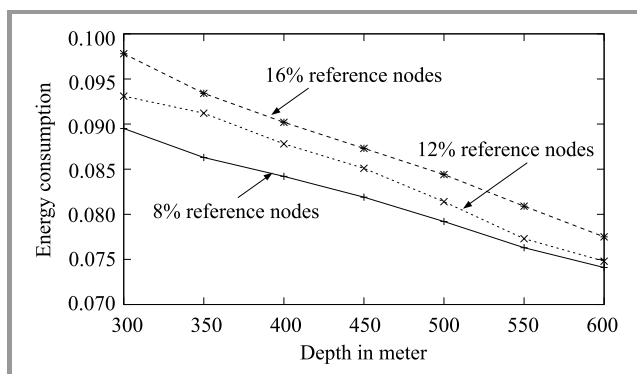


**Fig. 19.** Energy consumed by nodes in each trapezoid (for 80 nodes).

shown in Fig. 18. If the depth is increased further, fewer trapezoids are formed and fewer uw-nodes are present in such trapezoids. The nodes' excessive involvement in the localization process is moderately reduced and minimizes energy consumption, as observed in the graph.

## 7. Conclusion

In this paper, a node location estimation method is presented relying on computational geometrical trapezoids. The proposed scheme uses the trapezoids to create clusters of various sizes. The entire network is divided into trapezoids and a search data structure (SDS) is established. Further location estimation techniques are applied to localize nodes. Simulations performed prove that the proposed scheme may be used in UASN networks, offering good performance and accuracy levels.

## References

- [1] Z. Zhou, Z. Peng, J. Cui, and A. Bagtzoglou, "Scalable localization with mobility prediction for underwater sensor networks", *IEEE Trans. on Mob. Comput.*, vol. 10, no. 3, pp. 335–348, 2011 (DOI: 10.1109/TMC.2010.158).
- [2] X. Cheng *et al.*, "Silent positioning in underwater acoustic sensor networks", *IEEE Trans. Veh. Technol.*, vol. 57, no. 3, pp. 1756–1766, 2008 (DOI: 10.1109/TVT.2007.912142).
- [3] Y. S. Uddin, "Low-overhead range-based 3D localization technique for underwater sensor techniques", in *Proc. of IEEE Int. Conf. on Commun. ICC 2016*, Kuala Lumpur, Malaysia, 2016 (DOI: 10.1109/ICC.2016.7510873).
- [4] X. Sheng and Y.-H. Hu, "Maximum likelihood multiple-source localization using acoustic energy measurements with wireless sensor networks", *IEEE Trans. on Sig. Process.*, vol. 53, no. 1, pp. 44–53, 2005 (DOI: 10.1109/TSP.2004.838930).
- [5] V. Chandrasekhar and W. Seah, "An area localization scheme for underwater sensor networks", *Proc. OCEANS 2006 – Asia Pacific*, Singapore, 2006 (DOI: 10.1109/OCEANSAP.2006.4393969).
- [6] S. Kundu and P. Sadhukhan, "Design and implementation of a time synchronization-free distributed localization scheme for underwater acoustic sensor network", in *Proc. of Appl. and Innov. in Mob. Comput. AIMOC 2015*, Kolkata, India, 2015, pp. 74–80 (DOI: 10.1109/AIMOC.2015.7083833).
- [7] E. E. Lloyd *et al.*, "UREAL: underwater reflection-enabled acoustic-based localization", *IEEE Sensors J.*, vol. 14, no. 11, pp. 3915–3925, 2014 (DOI: 10.1109/JSEN.2014.2357331).
- [8] R. Hamid *et al.*, "Collision tolerant and collision free packet scheduling for underwater acoustic localization", *IEEE Trans. on Wirel. Commun.*, vol. 14, no. 5, pp. 2584–2595, 2015 (DOI: 10.1109/TWC.2015.2389220).
- [9] G. Han *et al.*, "Impacts of deployment strategies on localization performance in underwater acoustic sensor networks", *IEEE Trans. on Industr. Electron.*, vol. 62, no. 3, pp. 1725–1733, 2015 (DOI: 10.1109/TIE.2014.2362731).
- [10] T. V. Nguyen *et al.*, "Least square cooperative localization", *IEEE Trans. on Veh. Technol.*, vol. 64, no. 4, pp. 1318–1330, 2015 (DOI: 10.1109/TVT.2015.2398874).
- [11] T. Xu *et al.*, "RSS-based sensor localization in underwater acoustic sensor networks", in *Proc. of 41st IEEE Int. Conf. on Acoust., Speech and Sig. Process. ICASSP 2016*, Shanghai, China, 2016, pp. 3906–3910 (DOI: 10.1109/ICASSP.2016.7472409).
- [12] A. Savvides, H. Park, and M. B. Srivastava, "The bits and flops of the N-hop multilateration primitive for node localization problems", in *Proc. of the 1st ACM Int. Worksh. on Wirel. Sensor Netw. and Appl. WSN'02*, Atlanta, GA, USA, 2002, pp. 112–121 (DOI: 10.1145/570753.570755).

- [13] A. Savvides, C. C. Han and M. B. Srivastava, "Dynamic fine-grained localization in ad hoc networks of sensors", in *Proc. of the 7th Ann. Int. Conf. on Mob. Comput. and Network. MobiCom'01*, Rome, Italy, 2001, pp. 166–179, 2001 (DOI: <https://doi.org/10.1145/381677.381693>).
- [14] G. Zhu *et al.*, "A distributed localization scheme based on mobility prediction for underwater wireless sensor networks", in *Proc. of the 26th Chinese Contr. and Decision Conf. CCDC 2014*, Changsha, China, 2014, pp. 4863–4867 (DOI: 10.1109/CCDC.2014.6853044).
- [15] S. Lee and K. Kim, "Localization with a mobile beacon in underwater acoustic sensor networks", *Sensors*, vol. 12, no. 5, pp. 5486–5501, 2012 (DOI: 10.3390/s120505486).
- [16] Y. Sun *et al.*, "A mobile anchor node assisted RSSI localization scheme in underwater wireless sensor networks", *Sensors*, vol. 19, no. 20, 2019 (DOI: 10.3390/s19204369).
- [17] C. Zhang *et al.*, "A collaborative localization algorithm for UASNs", in *Proc. of the Int. Conf. on Comput., Manag. and Telecommun. ComManTel 2014*, Da Nang, Vietnam, 2014, pp. 211–216 (DOI: 10.1109/ComManTel.2014.6825606).
- [18] J. Gao *et al.*, "A double rate localization algorithm with one anchor for multi-hop underwater acoustic networks", *Sensors*, vol. 17, no. 5, pp. 984–1001, 2017 (DOI: 10.3390/s17050984).
- [19] M. Beniwal, R. P. Singh, and A. Sangwan, "A localization scheme for underwater sensor networks without time synchronization", *Wirel. Pers. Commun.*, vol. 88, no. 3, 2016 (DOI: 10.1007/s11277-016-3175-2).
- [20] Y. Zhang, J. Liang, S. Jiang, and W. Chen, "A localization method for underwater wireless sensor networks based on mobility prediction and particle swarm optimization algorithms", *Sensors*, vol. 16, no. 2, pp. 212, 2016 DOI: <https://dx.doi.org/10.3390/s16020212>.
- [21] Xin Su, I. Ullah, X. Liu, and D. Choi, "A review of underwater localization techniques algorithms and challenges", *J. of Sensors*, vol. 2020, no. 1, pp. 1–24, 2020 (DOI: 10.1155/2020/6403161).
- [22] M. de Berg *et al.*, *Computational Geometry*, 3 ed. Berlin, Heidelberg: Springer, 1983 (ISBN: 9783540779742).
- [23] B. Zhang *et al.*, "Received signal strength-based underwater acoustic localization considering stratification effect", in *Proc. of the OCEANS 2016*, Shanghai, China, 2016 (DOI: 10.1109/OCEANSAP.2016.7485561).
- [24] R. J. Urick, *Principles of Underwater Sound*, 1 ed. New York: McGraw-Hill, 1983 (ISBN: 9780070660878).
- [25] W. H. Thorp, "Analytic description of the low frequency attenuation coefficient", *J. of Acoustic. Soc. of America*, vol. 42, no. 1, pp. 270, 1967 (DOI: 10.1121/1.1910566).
- [26] W. Zhang *et al.*, "Fault-tolerant relay node placement in wireless sensor networks: Problems and algorithms", in *Proc. of the 26th IEEE Int. Conf. on Comp. Commun. INFOCOM 2007*, Barcelona, Spain, 2007, pp. 1649–1657 (DOI: 10.1109/INFCOM.2007.193).



**B. S. Halakarnimath** received his B.E. and M.Tech. degrees in Computer Science and Engineering from VTU, Belagavi, Karnataka, India. Presently, he is a VTU research scholar pursuing his Ph.D. under the guidance of Dr. A. V. Sutagundar, at Basaveshwar Engineering College, Bagalkot, Karnataka, India. He has authored one book

chapter and published five conference and journal papers. His research areas include underwater acoustic wireless sensor networks, machine learning, and algorithms. He is a life member of IEI and ISTE organizations.

E-mail: [basaprabhu97@gmail.com](mailto:basaprabhu97@gmail.com)

Research Scholar of VTU

Department of Computer Science and Engineering

S.G. Balekundri Institute of Technology

Belagavi-590010, Karnataka, India



**A. V. Sutagundar** received his B.E. and M.Tech. degrees in Electronics and Communication Engineering from VTU, Belagavi, Karnataka, India. He received his Ph.D. in 2013 from VTU, Belagavi, India. Presently, he is working as an Associate Professor at the Department of ECE, Basaveshwar Engineering College, Bagalkot,

Karnataka, India. He has authored eight book chapters and published more than 75 papers at international conferences and in various journals. His research areas include IoT, wireless sensor networks, machine learning, and digital image processing.

E-mail: [sutagundar@gmail.com](mailto:sutagundar@gmail.com)

Department of Electronics and Communication

Basaveshwar Engineering College

Bagalkot-587102, Karnataka, India

# Suboptimal Approach to Distributed Detection in Cognitive Radio Networks

Shweta Kumari and Sirimilla Praveena

*Department of Electronics and Communication, Indian Institute of Information Technology Design & Manufacturing (IIITDM), Kancheepuram, Chennai, India*

<https://doi.org/10.26636/jtit.2021.144720>

**Abstract**—In this paper a dynamic spectrum access (DSA) concept is explored for mitigating the paucity of spectral bandwidth in cognitive radio (CR) for opportunistic, dynamic access of the spectrum without any interference. Dynamic spectrum access schemes are proposed for a distributed cognitive radio network consisting of one secondary user (SU) and many primary users (PUs). The SU has to make decisions for accessing PU channels within discrete time slots. The design of sensing and access strategies that govern channel choice in each slot for near-optimal throughput performance of the SU may be formulated as a partially observable Markov decision process (POMDP). Furthermore, it is considered that the SU incurs a cost whenever it switches to a different channel. The switching cost is expressed in terms of delay, packet loss and packet overhead. In this work, the SU access policy based on a myopic approach is proposed and evaluated.

**Keywords**—cognitive radio, distributed detection, energy detector, myopic policy, spectrum sensing.

## 1. Introduction

According to a survey by the US Federal Communications Commission (FCC), utilization of the radio spectrum in the 30–3000 MHz frequency bands equaled, in the US, just 5.2% in 2004–2005 [1]. The spectrum utilization rate is also characterized by variations based on geographical locations. This underutilization of the spectrum resources creates a new communication paradigm to exploit it dynamically. A solution under which the licensed spectrum is shared among unlicensed users is a promising approach allowing to cope with the issue of spectrum scarcity. Dynamic spectrum access (DSA), i.e. a method allowing the spectrum to be accessed dynamically depending on current needs is a promising solution to this problem. DSA is supported by spectrum agile devices, such as cognitive radio (CR), which may opportunistically identify vacant portions of the spectrum known as white holes, and may transmit using them while maintaining limited interference, so as not to affect the licensed users.

In this paper, a simple, heuristic spectrum sensing policy deployed in a distributed POMDP CRN framework comprising 1 SU and  $N$  PUs is presented. In addition, a less

complex access policy relying on the myopic approach with immediate two-stage reward in a similar environment of 1 SU and  $N$  PUs, where  $N > 1$ , along with energy constraints and channel switching costs, is proposed.

## 2. Related Works

A variety of spectrum sensing techniques for CR is proposed in [2]. These techniques range from simple energy detection to advanced schemes based on cyclostationary feature detection. A survey of available schemes presented in [3] reveals that energy detection (ED) is the easiest and most widely used sensing approach. Its advantage lies in the fact that it does not need any a priori information concerning the primary user (PU) channel transmission characteristics, is easily implementable and has low computational complexity. The disadvantage, however, is that ED takes a long sensing time for the detection of low SNR primary signals. Besides, the sensing threshold in ED is an important parameter. The receiver operating characteristic (ROC) curve and the interference limits determine the threshold values. In [4], dynamic estimation of noise power is proposed. It eliminates the performance-related restrictions of ED due to the estimation error of noise signal power.

The authors describe the concept of the adaptive threshold in [5]. It is based on the signal-to-interference noise ratio (SINR). Bazerque *et al.* in [6] proposed that spectrum sensing may be performed either in a centralized or distributed manner. The centralized and distributed approaches may be either cooperative or non-cooperative. The centralized approach involves the collection of data from each SU at the center and taking the final decision based on a specific rule. Cooperative spectrum sensing is studied in [6] to reduce the detection time and to improve robustness. An OFDM-based system is proposed in [7], wherein the decisions from all local SUs are taken and given to the center. The center makes the final decision on the bias and/or logical combinations. However, due to the existence of different channel conditions, the approach is not optimal.



A sequential detection procedure is proposed in [8], where the samples are taken sequentially and the log-likelihood ratio is computed for each SU. This approach makes use of two thresholds. If the ratio falls within the upper and lower threshold, the next sample is taken. Otherwise, a decision is made. An improvement to the previous approach is made in [9] and is known as sequential shift chi-square test. The improvement consists in introducing a bound to the number of sensing samples. In [10], the authors proposed a consensus-based algorithm for sensing policy. It considers a distributed environment where the SU makes the decision based on local observations only. The previous works take into account a cooperative distributed environment in which the SUs cooperate with each other make the final decision. Also, the observations of all SUs are taken to a fusion center in order to make the final decision, meaning that the approach is centralized.

Very few works are concerned with distributed non-cooperative environments. In this project, we have considered a distributed scenario with 1 SU and  $N$  PUs. The PUs and the SU are working independently, without any knowledge of each other's state. Under the energy constraint, we have developed a heuristic access policy for SU. Also, another algorithm has been developed which takes into account the switching cost that the SU incurs when it switches to a channel other than the current channel. The objective is to minimize the switching cost.

### 3. Heuristic Approach to Energy Efficient Detection

Consider a CRN comprising a set  $N$  PUs, i.e.  $P = \{1, 2, \dots, N\}$  and 1 SU. The channel is intended for use by the PU, but while it is not transmitting, it is sensed and used by SUs. The propagation condition has been taken as an unfading channel. Time is  $k$ -slotted and is non-negative  $k = \{1, 2, 3, \dots\}$ . The statistics of primary network traffic are such that the occupancy of the primary channel in time slot  $k$  follows  $N$  independent discrete time Markov processes comprising two states. The state of channel  $i$  in time slot  $k$  may be either busy (0) or idle (1), which is denoted by a theta vector  $\theta_{i,k} \in (0, 1)$ . The state vector of  $N$  PUs at the beginning of time slot  $k$  is denoted as  $\Theta_k = \{\theta_{1,k}, \theta_{2,k}, \dots, \theta_{N,k}\}$ . The transition probability of the theta vector is  $P_{i,k} = [p_{00}p_{01}; p_{10}p_{11}]$ . The sensing model is:

$$P(Y_{i,k} = 0 | \theta_{i,k} = 0) = \alpha, \quad (1)$$

$$P(Y_{i,k} = 0 | \theta_{i,k} = 1) = \beta, \quad (2)$$

$$P(Y_{i,k} = 1 | \theta_{i,k} = 0) = 1 - \alpha, \quad (3)$$

$$P(Y_{i,k} = 1 | \theta_{i,k} = 1) = 1 - \beta. \quad (4)$$

The considered framework is a partially observable Markov decision process (POMDP) environment, where the SU does not have a complete knowledge of the states of PUs. In this case, the SU senses the spectrum available at a given time slot and decides to access a free channel. The observations may therefore result in some collisions, thereby decreasing the overall throughput. To keep the energy low and due to the limited sensing ability of the SU, a heuristic approach to its access-related actions is formulated.

The cost incurred when the SU switches to a channel other than its current channel  $c$  and assumed as  $\lambda$ . The SU notices the state of the system at the beginning of time slot  $k$  as  $Y_k = [\Theta_k, c]$ . Since the SU cannot observe the state of the channel directly, it has to infer that state from partial sensing outcomes. For this,  $\pi_{i,k}$  denotes the conditional probability that channel  $i$  is sensed as idle, given the past and present states of the channel:

$$\pi_{i,k} = P(\theta_{i,k} = 1 | Y_1, Y_2, \dots, Y_k). \quad (5)$$

The probability that channel  $i$  is idle in time slot  $k+l$  depends on the probability of channel  $i$  being idle in previous time slot  $k$  and the transitional probability of state.  $\pi_{i,k+1}$  is therefore a recursive function of its previous value.  $\pi_{i,k+1}$  is calculated for two scenarios. The first scenario is concerned with the sensed channel:

$$\pi_{i,k+1} = \frac{[p_{11}\pi_{i,k} + p_{01}(1 - \pi_{i,k})]\beta}{[p_{11}\pi_{i,k} + p_{01}(1 - \pi_{i,k})]\beta + [p_{10}\pi_{i,k} + p_{00}(1 - \pi_{i,k})]\alpha}, \quad (6)$$

when  $Y_{i,k} = 0$ , and

$$\pi_{i,k+1} = \frac{[p_{11}\pi_{i,k} + p_{01}(1 - \pi_{i,k})](1 - \beta)}{[p_{11}\pi_{i,k} + p_{01}(1 - \pi_{i,k})](1 - \beta) + [p_{10}\pi_{i,k} + p_{00}(1 - \pi_{i,k})](1 - \alpha)}, \quad (7)$$

when  $Y_{i,k} = 1$ .

For the unsensed channel, it is:

$$\pi_{i,k+1} = p_{00}\pi_{i,k} + p_{01}(1 - \pi_{i,k}). \quad (8)$$

The proposed algorithm is given as Algorithm 1.

---

**Algorithm 1:** A direct algorithm signifying the importance of parameter  $\pi_{i,k}$

---

1. **Input** vector:  $S_k = [1, 2, \dots, N]$ .
  2. **Output:** SU accesses any of the above channels based on sensing policy.
  3. **For**  $i = 1$  **to**  $N$  calculate  $|\pi_{j,k}|$  **End for**
  4. **If**  $|\pi_{j,k}| > \gamma$  then access  $j$
  5. **Else** do not access  $j$
  6. **End if**
-

### 3.1. Simulation Results

The simulation was performed using Matlab software. A CRN consisting of 1 SU and  $N$  PUs is considered. Monte Carlo simulation is carried out with  $10^4$  iterations, which is also the number of available time slots. The initial  $\theta_i$  for  $t = 0$  is taken as 0.5. The observations at each time slot are generated based on Eqs. 1–4. For each time slot,  $\pi_i$  is generated for channel  $i$ , where  $i \in \{1, 2, \dots, N\}$  from Eqs. 6–8. Next,  $\pi_i$  is compared with the threshold value  $\gamma$  that varies from 0.2–0.7. The throughput of SU against the threshold values is defined as:

$$\text{Throughput} = \frac{\text{Total no. of accesses}}{\text{Total time slot}} \cdot (1 - \text{Probability of collision}) .$$

Based on the simulation, the number of slots found to be idle is: 4012.3 and the number of busy slots is: 5987.7. The results given by the heuristic algorithm are shown in Figs. 1–3. As may be observed from Figs. 1–2, the throughput and the probability of collision decrease. This is clearly understandable, because as the threshold value increases, the number of primary channels open for access to SU will decrease, thus reducing throughput. Figure 3 shows that the probability of collision varies as the number of accesses by the SU increases until it reaches full saturation. As the number of accesses by SU increases, the number of SU’s

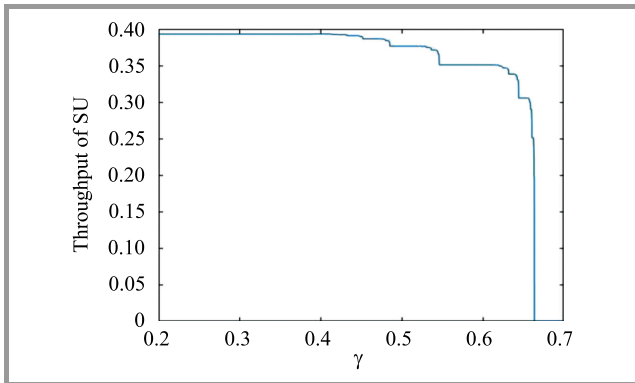


Fig. 1. Throughput vs.  $\gamma$ .

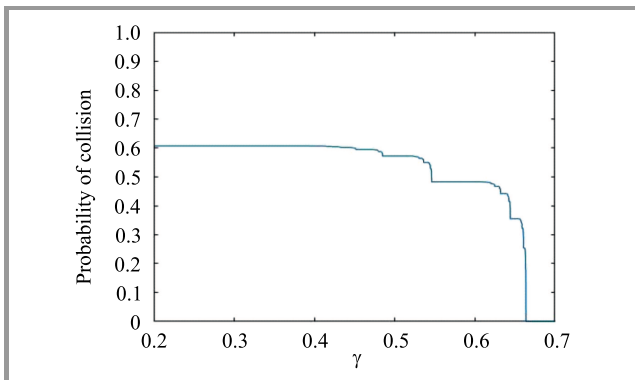


Fig. 2. Probability of collision vs.  $\gamma$ .

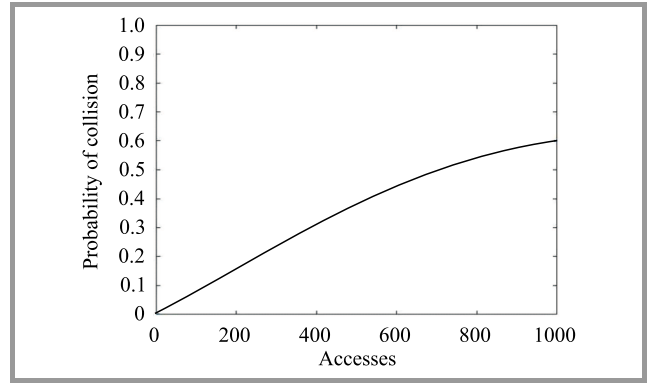


Fig. 3. Probability of collision vs. number of accesses.

collisions with the licensed user grows, explaining the variation shown in Fig. 2. So, a trade-off is achieved between the probability of a collision and throughput at a particular threshold value. The value of the threshold should be such that the quality of service is not compromised for PUs. Since this is a heuristic approach, it just offers an insight into the basic understanding of the parameter  $\pi_{i,k}$  for access into the activity of SU in an environment with distributed PUs, while maintaining the required QoS.

## 4. Energy Efficient Detection Using Myopic Policy

For a greater convergence with the optimal solution, we propose a myopic policy for sensing and for access actions undertaken by SU. Let  $a_k = [1, 2, 3, \dots, 10]$  denote the access action of SU in a given time slot  $k$ , where 0 means no access action. Here, we introduce the concept of a reward. Every action and state of SU carries with itself a certain reward. The SU considered here incurs a switching cost whenever it has to switch to other channels. The switching cost mentioned here and incurred by SU is expressed in terms of delay, packet loss, and packet overhead. This is because when the SU changes from one frequency to another, both the SU transmitter and receiver should be coordinated properly. If they are not coordinated, the SU transmitter may start sending packets even when the SU receiver is not ready. This incurs a delay, also it may lead to packet loss at the receiver. The packet loss initiates a retransmission which is considered as packet overhead. The significance of the reward lies in the fact that it helps the SU analyze how useful its access actions are in the long run. The usefulness is stated here in terms of minimizing the number of frequent channel changes.

The SU cannot make the observations directly, since the problem is considered for a POMDP environment. It has to sense the observations and make decisions. In the heuristic solution proposed in Section 3, no attempt is made to reduce the number of occasions on which SU switches to another PU channel in order to reduce the switching cost. Therefore, a sensing and access policy is needed that allows

SU to switch the channel whenever the necessity arises. Obtaining the optimal policy for a general POMDP is often intractable. In fact, based on [11], it is clear that the complexity for obtaining the optimal solution for spectrum sensing and accessing opportunistically is of the order of  $N^T$ , where  $N$  is the number of channels in the spectrum of interest and  $T$  is the total time horizon. In this regard, a myopic policy with an immediate two-stage reward is proposed as a simple solution that achieves near-optimal performance.

#### 4.1. Myopic Policy Solution

For a given state-action pair  $([\theta_k, a_k], c_k)$ , we assume the immediate reward earned by SU accessing channel  $i$  in time slot  $k$  as:

$$r([\theta_k, c], a_k) = \begin{cases} 0, & \text{if } a_k = 0 \\ 1, & \text{if } a_k = c, \theta_{c,k} = 1 \\ l - \lambda, & \text{if } a_k \neq c, \theta_{a,k} = 1 \end{cases} \quad (9)$$

The maximum reward is 1 when the SU makes the decision to access the same channel in the next time slot and that channel happens to be idle also. Let us define  $S_k \in \{1, 2, \dots, N\}$  as the state of SU in time slot  $k$ . Since the transition probabilities of vector  $S$  do not remain constant and depend on the current state and action, they are derived as:

$$P(S_{k+1}|S_k, a_k) = \begin{cases} p_{11} \text{ with probability } \pi_{i,k} & \text{if } a_k = c \\ p_{01} \text{ with probability } 1 - \pi_{i,k} & \text{if } a_k = c \\ p_{11} \cdot \pi_{i,k} + p_{01} \cdot (1 - \pi_{i,k}) \text{ with probability } 1 & \text{if } a_k \neq c \\ 0 & \text{if } a_k = 0 \end{cases} \quad (10)$$

The two-stage reward is formulated as the sum of the reward in the current state and the reward in the immediate future time slot. Thus, the reward depends on the current reward and on the transitional probabilities of the state. The reward is:

$$R(S_k, a_k, a_{k+1}) = r(S_k, a_k) + \sum_{S_{k+1}} r(S_{k+1}, a_{k+1}) \cdot P(S_{k+1}|S_k, a_k) \quad (11)$$

The SU senses the observation and, hence, the two-stage reward becomes the expected two-stage reward and is:

$$E[R(S_k, a_k, a_{k+1})] = E[r(S_k, a_k)] + \sum_{S_{k+1}} E[r(S_{k+1}, a_{k+1})] \cdot P(S_{k+1}|S_k, a_k) \quad (12)$$

The SU sensing policy then proceeds to sensing those channels for which the parameter  $\pi_{i,k}$  is greater than a certain threshold  $\gamma$ . The access policy starts choosing only those channels in the discrete time slot  $k$  for which the expected two-stage reward is the highest:

$$a_k = \arg \max(E[R(S_k, a_k, a_{k+1})]) \quad (13)$$

#### 4.2. Simulation of the Myopic Approach

The simulation is carried out using Matlab with CRN and the same environment as given in Subsection 3.1, consisting of 1 SU and  $N$  PUs. Based on the sensed channels, the SU calculates the maximum two-stage reward in each time slot and accesses only those primary user channels that are characterized by the maximum two-stage reward. As far as channel quality is concerned, parameter  $\pi_{i,k}$  is taken, since it describes the probability of the primary channel being idle in time slot  $k$ . The switching cost  $\lambda$  is taken as 0.3. For a particular access policy, a particular threshold value of 0.48 is taken for which the total reward accumulated is the highest.

The two-stage reward myopic policy is an alternative for the intractable optimal solution while maintaining a certain quality standard. Figure 4 shows that overall throughput is acceptable. As shown in Fig. 1 and Fig. 4, the throughput is improved from 0.4 to 0.65. Figure 4 shows throughput against the probability of collision. Throughput increases as the probability of collision increases. This is counterintuitive, since the collision rate should decrease the throughput of the network. But since the threshold values increase, the number of accesses by SU decreases, as may be seen from Fig. 6. Therefore, the probability of a collision of SU decreases as well. The total reward earned by the SU and the number of accesses show similar variations with respect

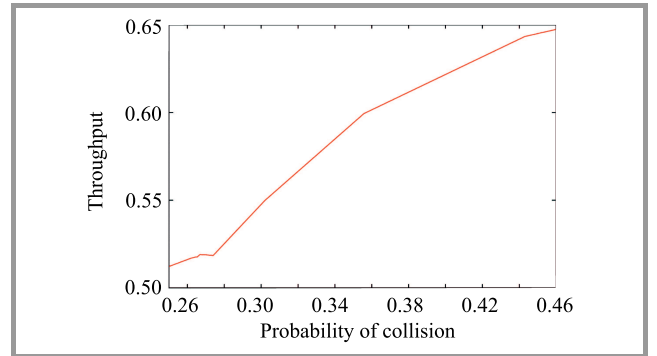


Fig. 4. Throughput as a function of probability of collision.

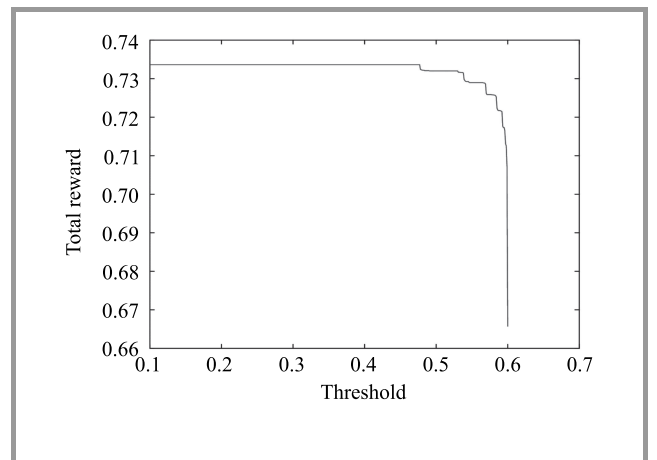


Fig. 5. Total reward as a function of threshold.

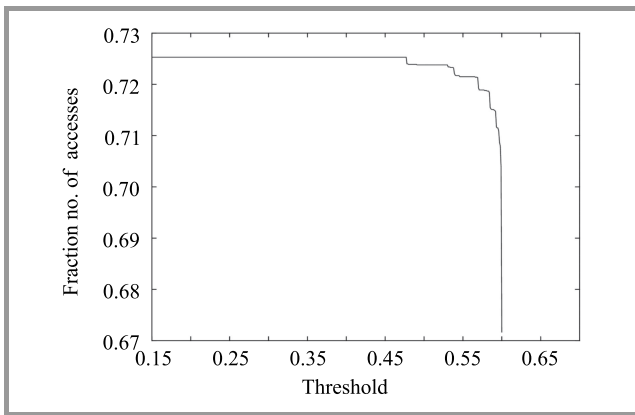


Fig. 6. Number of access of PU by SU as a function of threshold.

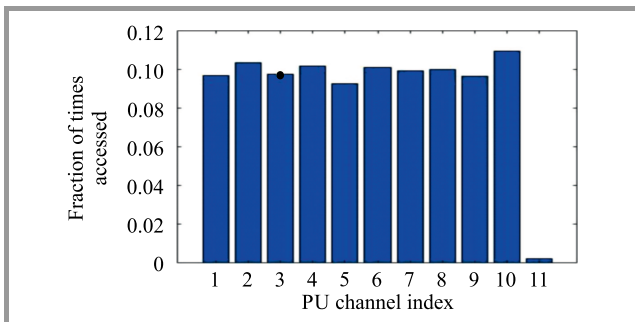


Fig. 7. Access action for  $\pi_{i,k} = 0.48$ .

to the threshold values as those seen in Figs. 5–6. This implies that the total reward that a SU earns is directly proportional to the number of times it is allowed to use a PU channel. Figure 7 shows the access action of SU for the threshold value of 0.48. This value is chosen to ensure that the chance of finding a busy channel is not lower, while also keeping in consideration the total reward accumulated. The maximum throughput value of 0.65, as shown in Fig. 4, is meaningful for the result in [12].

## References

- [1] K. Patil, R. Prasad, and K. Skouby, “A survey of worldwide spectrum occupancy measurement campaigns for cognitive radio”, in *Proc. Int. Conf. on Devices and Commun. ICDeCom* IEEE, Mesra, India, 2011, pp. 1–5 (DOI: 10.1109/ICDECOM.2011.5738472).
- [2] E. Axell, G. Leus, E. G. Larsson, and H. V. Poor, “Spectrum sensing for cognitive radio: State-of-the-art and recent advances”, *IEEE Signal Process. Mag.*, vol. 29, no. 3, pp. 101–116, 2012 (DOI: 10.1109/MSP.2012.2183771).
- [3] R. Umar and A. U. Sheikh, “A comparative study of spectrum awareness techniques for cognitive radio oriented wireless networks”, *Physical Commun.*, vol. 9, pp. 148–170, 2013 (DOI: 10.1016/j.phycom.2012.07.005).
- [4] A. A. Khan, M. H. Rehmani, and M. Reisslein, “Cognitive radio for smart grids: Survey of architectures, spectrum sensing mechanisms, and networking protocols”, *IEEE Commun. Surveys & Tutorials*, vol. 18, no. 1, pp. 860–898, 2016 (DOI: 10.1109/COMST.2015.2481722).
- [5] M. Riahi Manesh, N. Kaabouch, H. Reyes, and W.-C. Hu, “A Bayesian approach to estimate and model SINR in wireless networks”, *Int. J. of Commun. Systems*, vol. 30, no. 9, pp. 1–11, 2016 (DOI: 10.1002/dac.3187).

- [6] J. A. Bazerque and G. B. Giannakis, “Distributed spectrum sensing for cognitive radio networks by exploiting sparsity”, *IEEE Transactions on Signal Process.*, vol. 58, no. 3, pp. 1847–1862, 2010 (DOI: 10.1109/TSP.2009.2038417).
- [7] G. Ganesan and Y. Li, “Cooperative spectrum sensing in cognitive radio networks”, in *Proc. 1st IEEE Int. Symp. on New Frontiers in Dynamic Spectrum Access Networks. DySPAN 2005*, Baltimore, USA, 2005, pp. 137–143 (DOI: 10.1109/DYSPAN.2005.1542628).
- [8] T. Weiss, J. Hillenbrand, A. Krohn, and F. K. Jondral, “Efficient signaling of spectral resources in spectrum pooling systems”, in *Proc. 10th Symp. on Commun. and Vehicular Technol. SCVT*, 2003 [Online]. Available: [https://www.teco.edu/krohn/efficient\\_signaling.pdf](https://www.teco.edu/krohn/efficient_signaling.pdf)
- [9] A. Wald, *Probability and Mathematical Statistics*. Wiley, 1947 (ISBN: 9780471918066).
- [10] Y. Xin, H. Zhang, and S. Rangarajan, “SSCT: A simple sequential spectrum sensing scheme for cognitive radio”, in *Proc. IEEE Global Telecommun. Conf. GLOBECOM*, Honolulu, USA, 2009, pp. 1–6 (DOI: 10.1109/GLOCOM.2009.5425738).
- [11] D. V. Djonin, Q. Zhao, and V. Krishnamurthy, “Optimality and complexity of opportunistic spectrum access: a truncated Markov decision process formulation”, in *Proc. of IEEE Int. Conf. on Commun. ICC*, 2007, pp. 5787–5792 (DOI: 10.1109/ICC.2007.959).
- [12] A. Fanous, Y. E. Sagduyu, and A. Ephremides, “Reliable spectrum sensing and opportunistic access in network-coded communications”, *IEEE J. on Selected Areas in Commun.*, vol. 32, no. 3, 2013, pp. 400–410 (DOI: 10.1109/JSAC.2011.031403).



**Shweta Kumari** has an M.Tech. degree in Communication Systems Design from IITDM Kancheepuram, India. Her areas of interest include wireless communications, image processing and antenna design. She was selected for JASSO Scholarship, Japan, where she worked on the YOLO object detection algorithm.

E-mail: fsc.kshweta@gmail.com  
 Department of Electronics and Communication Engineering VFSTR  
 Guntur, A.P.  
 India



**Sirimilla Praveena** has an M.Tech. degree in Communication Systems Design from IITDM Kancheepuram, India. Her areas of interest include antenna design and wireless communication.

E-mail: psirimilla@gmail.com  
 Department of Electronics and Communication Engineering VFSTR  
 Guntur, A.P.  
 India

# Evaluation of Reliability of Mobile ICT Services

Marian Kowalewski, Ryszard Kobus, and Tomasz Sędek

*National Institute of Telecommunications, Warsaw, Poland*

<https://doi.org/10.26636/jtit.2021.141420>

**Abstract**—This article discusses common problems with reliability and availability of ICT services, mainly in mobile networks. Internet access-related services have been examined and traditional service quality assessment methods have been compared with the proposed solutions, with the primary focus placed on availability and reliability of mobile services. The required parameter values describing reliability and quality levels have been defined and proposed.

**Keywords**—reliability, ICT mobile services, user satisfaction.

## 1. Introduction

The problem of ensuring the highest quality of telecommunication services enjoyed by users has been on the agenda for quite some time now. It was finally tackled, in connection with telephony services, in 1994, in the ITU-T E.800 recommendation that contained definitions of terms related to the quality of service. E.800 emphasizes the fact that the opinion of service users forms an important aspect of the overall assessment of any given service. This assumption serves as a basis for determining the degree of user satisfaction. Recommendation E.800 provides:

- primary concepts,
- basic information related to the quality of services and to network performance,
- a set of key performance indicators (KPIs).

Broadband Internet access relying on fixed connections was not offered until the 1990s. The first patent for an asymmetric digital subscriber line (ADSL) was filed in 1988. Initially, twisted-pair telephone cables with digital subscriber line (DSL) systems were used. Then, ADSL was introduced, and cable television networks entered the mainstream by relying on the data-over-cable service interface specification (DOCSIS) technology, offering speeds similar to those achieved with ADSL. The definition of QoS was then extended to cover broadband Internet access as well [1]. It should be noted that in cable networks the number of users and the maximum data transfer rate were known a priori. Therefore, ensuring the quality of service was relatively simple. However, due to concerns regarding competitive pricing, the services were offered as a “best

effort delivery”, i.e. without promising the same speeds at all times.

Usually, a given service is offered with a transfer rate that exceeds the users’ typical needs, and some loss of speed is acceptable.

In wireless radio networks, QoS parameters depend also, to a considerable degree, on the following [2]:

- user location,
- season (of the year),
- day of the week,
- time of day.

The related model of Internet access is presented in Fig. 1 [3], [4]. It presents the chain of a typical use of Internet service from the user’s terminal through the access network (wire or wireless) and the backbone network to the content provider’s server (Internet service). The research and practice show that each of the presented components of the model introduces some throttling limitations in the transmission of data packets.

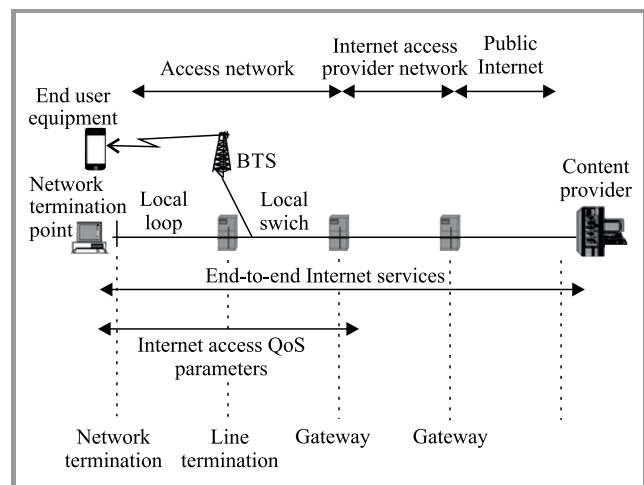


**Fig. 1.** Internet service provision model.

## 2. Research on the Quality of Services

We should take into account that Internet access-related needs of PC computer and smartphone users vary signifi-



cantly. Smartphone owners are highly mobile, but accept slightly lower data transmission speeds. Smartphone users are currently the largest and continuously growing group of mobile network users. For many of them, the smartphone has become a basic communication tool used during business and tourist travel. Such users need to use navigation data, tourist guides, apps containing timetables and routes, as well as those allowing to purchase city and regional transportation tickets. Social applications, video calls, etc. are used as well.

Unlike in the case of cable-based services, mobile service providers (operators) cannot control the number of users in a given area. Usually, the operator manages several networks relying on different telecommunication generations and technologies. Such an approach provides room for optimization, each user may be connected to a network that provides transmission speed that is optimized for a given location at current network load. The maximum transfer rate is defined for each frequency band, bandwidth or combination of both band and bandwidth, network configuration and type of equipment used, and is shared with a group of users.

The quality of service provided could be examined *inter alia* based on the parameters specified in QoS [5] or based on other measurements, such as quality of services dedicated to tourists [6].

In the European Union (EU), a document [7] issued by the Body of European Regulators for Electronic Communications (BEREC) serves as a guide related to the quality of services. It was drawn up in the process of implementing the European Electronic Communications Code (EECC) Directive [8]. The quality of service is defined, in the said document, in the form of the ITU-T Recommendation Y.2617 [9]. The document includes complex QoS parameters concerning Internet access services, including delay, jitter, and packet loss ratio.

Data throughput is a parameter that depends on conditions being beyond the control of the operator, and, therefore, cannot be guaranteed, but exerts a significant impact on QoS.

QoS measurements may be performed using dedicated testers installed at selected locations, or with the use of mobile equipment in vehicles traveling along selected routes [10]. Most often, these will include the most important public roads. Radio signal coverage is assessed based on computer simulations augmented with measurements performed at selected locations. Measurements covering the entire area on which a given service is rendered are too expensive.

### 3. Definition of Reliability of ICT Services

As far as the operation of equipment, devices and networks is concerned, and in terms of ICT services, the reliability of these components becomes increasingly important. Most

often it is perceived in two ways, from the point of view of the user and service provider, in this case referred to as the operator.

Reliability is a property of the system and of the ICT network that is related to the ability to perform tasks efficiently, i.e. to the availability of a defined range of services that are rendered in accordance with the intended use and under specific operating conditions. One may assume that reliability is the ability of the system and of the network to provide ICT services. Reliability is also defined by the ability of operator's organization to provide a specific service characterized by parameters expected by customers, under specific operating conditions affecting the telecommunications network.

From the user's point of view, QoS and reliability are defined in terms of their perception, i.e. satisfaction with ICT services provided to match their needs. From this point of view, assessment indicators play an important role in the process of evaluating the service, being a measure describing the degree to which the requirements have been fulfilled.

The research<sup>1</sup> carried out shows that availability of IT services is related to reliability of ICT services. Accessibility is a specific requirement and also a specific indicator describing the degree to which service reliability-related expectations have been fulfilled. Availability of a service means the ability to rely on that service, to a specific degree and in accordance with the user's needs, with the said degree (scope) of the service indicated in the contract for its provision and agreed upon between the operator and the service recipient (user or customer). In other words, availability means the ability to obtain services at the user's request, in accordance with a defined scope and under specific conditions.

Availability of a service is closely related to the timeliness of communication, understood as the ability of devices and IT networks to ensure the transmission of information within a predefined period of time [11]. This underscores the role and the importance of the service provider in ensuring timeliness, as well as availability and reliability of communication.

Review of the literature indicates that, initially, reliability was used mainly for describing specific features of technical devices and systems [12]. Currently, the concepts of reliability and durability are also applied in system modeling and in software quality models [5], [6], [13]. In addition, it should be noted that an attempt was made in [14] to apply these terms for the assessment of non-technical parameters related to the services provided.

### 4. Testing Reliability and Quality

As far as reliability of ICT services is concerned, work is underway to assess the impact of reliability and qual-

<sup>1</sup>Research performed as part of scientific (statutory) activities of the National Institute of Telecommunications and the Warsaw University of Technology (Poland) in 2016–2018.

ity of service on customer satisfaction [13]. This approach adheres to the principle of testing services in accordance with the end-to-end concept. The problem of researching end-to-end services in mobile networks has been comprehensively addressed by RootMetrics [15]. For the purpose of this paper, a methodology used for assessing achievement of the expectations of an end user relying on a device that is typical of a specific Internet service is determined. It takes into account the time of day and the location of the user to evaluate service availability and its perceivable quality. In [15], it is estimated that the assessment methodology in question is better correlated with the feelings of users of ICT services than research conducted based on the approach used in the case of traditional fixed networks.

Initially, a set of QoS indicators describing the quality of ICT services for fixed networks was developed. These indicators assess mainly the degree of fulfillment of the business contract or of the operator's promises, with the results presented as a score that is based on a series of tests or measurements during which the maximum capacity of the network in question was sought [16], [17]. These measurements were used mainly to assess performance of the network in terms of access thereto.

In the case of wireless radio networks, the studies conducted show that third, fourth and fifth generation mobile technologies are not capable of offering stable parameters pertaining to ICT services due to their dependence on:

- base station technology and cell capacity,
- type of user device and its technical advancements,
- network load, e.g. the number of active users using one base station,
- location, i.e. the user's distance to the nearest base station,
- date and time of day.

## 5. Proposed Solution

Mobile users are not usually interested in the maximum transmission speed offered by the network, but in achieving data throughput that is sufficient for their needs, their location and the services they use, with a satisfactory level of quality and reliability guaranteed as well. The research shows that the maximum transmission speed is achieved only during speed tests. Under real conditions, performance is often inferior. Service providers should therefore consider parameters guaranteeing that services may be provided to end users with satisfactory reliability and quality levels. The necessary network resources need to be estimated, as it has already been done, in practice, in [4], but only for a scenario in which the end user utilizes a personal computer. Currently, the recommended set of QoS indicators [7], [9] no longer includes transmission speed. Hence, the interest of the regulatory agencies in this indicator has decreased significantly.

At this point, the question arises whether the user's needs will be the same everywhere and at any time. Research shows that the same type of service will generate different experience on a high-performance computer and on a tablet or smartphone (with a smaller screen and less advanced processors). This is due to two reasons: the user's terminal (smartphone) may generate larger restrictions concerning the service rendered than a device operating within a fixed network. The service provider may adapt the content to the type of the user's terminal. To improve accessibility to information, websites are usually available in their mobile version as well, or are accessible through a dedicated application (proxy). It is often the case that they are adapted to smaller screens, which results in the fact that presentation of the mobile version of a web page requires lower data transfers.

The minimum values of network access-related parameters that need to be met to render selected ICT services using a PC computer and a smartphone are presented in Tables 1 and 2, respectively.

Table 1  
Minimum requirements concerning network access parameters that need to be fulfilled to provide services using a PC computer, based on [4]

Application group	Transmission speed (download/upload) above	Delay of up to
Browsing websites	1 Mb/s DL	200 ms
Watching videos in SD quality	2 Mb/s DL	200 ms
Viewing videos in HD quality	6 Mb/s DL	200 ms
HD video calls	1.5 Mb/s DL/UL	150 ms
Telephone services using VoIP technology	64 Kb/s DL/UL	150 ms
Multiroom services (3 × HD video)	18 Mb/s DL	200 ms
Real-time network games	2 Mb/s DL and 1 Mb/s UL	50 ms
Other network games (board games etc.)	1 Mb/s DL/UL	200 ms

Table 2  
Minimum requirements concerning network access parameters that need to be fulfilled to provide services using a smartphone

Application group	Transmission speed over	Delay of up to
Browsing mobile (or simplified) versions of web pages or using application	0.2 Mb/s DL	200 ms
Internet TV or video in 480p quality	0.5 Mb/s DL	200 ms
Internet TV or video in SD quality (720p)	1.5 Mb/s DL	200 ms
Internet TV or HD video (1080p)	6 Mb/s DL	200 ms

Table 1 was based on the experience of the largest telcos, collected while working, jointly, on the so-called memorandum on cooperation for improving the quality of services [4]. In addition to the indicators, changes to measurement methods were also suggested, compared to those proposed in [3].

Table 2 lists the minimum parameters for smartphones. Practical use cases show that these values are sufficient for watching IPTV (Internet TV) or movies at lower transmission speeds, thanks to smaller screen sizes and, therefore, lower resolution of videos that need to be downloaded. Examples of transmission speed requirements for high definition (HD), standard definition (SD) and 480p quality thresholds are shown in Table 2.

Based on the research performed, the authors propose that a downstream speed of at least 0.2 Mbit/s should be considered a minimum QoS requirement. Achieving a downstream speed of at least 1.5 Mbit/s should be regarded as a service with an average quality level, speeds of at least 6 Mbit/s should be considered as offering high levels of quality. Due to different packet types used in data transmission, the speed values given above should be considered as averages over 2 s periods.

The minimum quality speed (i.e. 0.2 Mbit/s) does not allow for comfortable use, but one that allows the smartphone user to receive the light-weight e-mails and to view simple, mobile versions of websites with a maximum delay of 200 ms. It is known from practice that such a transmission speed will not be sufficient for watching IPTV (Internet TV) or movies. To ensure the required reliability and quality levels and depending on the resolution of images, video transmission speeds should range from 0.5 to 6 Mbit/s. However, stability of the mobile service parameters is low and depends strongly, inter alia, on the traffic handled, i.e. on the number of active users presented in a given area.

The average throughput of 0.2 Mbit/s, available at a given location may be defined as a threshold value offering reliability of service and the minimum level of quality. On the other hand, reaching the speed of 1.5 Mbit/s may be defined as a value enabling to achieve reliability of service and the average level of quality. Going further, instead of

classic terrain coverage maps, service providers (operators) may publish service availability maps with areas where the service will be available with a 90% reliability level for transmission speeds of 0.2 and 1.5 Mbit/s.

In practice, such information would be more useful to the user than radio coverage maps, because it would include data on the level of availability and reliability of a given service at a specific location. Doubts concerning the usefulness of coverage maps for telecommunication network users were also expressed in [18].

Evaluation of reliability of services based solely on physical measurements is unrealistic due to the high costs involved. Therefore, the authors propose an evaluation method combining the following:

- measurements relying on testers installed at locations where the minimum level of service is expected,
- based on signal coverage in other areas.

Measurements should be carried out during typical periods of high activity, e.g. between 8 am to 8 pm. They should be performed with the test server connected outside the cellular operator's core network, e.g. at the Internet exchange point. The tester should rely on the most popular operating system (Android) and should be operated with typical user settings, i.e. it should be able to work with all available frequencies and access technologies by selecting them freely (free mode), in accordance with the operator's recommendations. Additionally, it is recommended that access to popular applications should be verified as well as social networks, train navigation, local public transport timetables, etc. It has been noticed that applications created for smartphones are better at coping with disruptions to mobile network transmissions than applications viewed with the use of web browser.

## 6. Conclusion

The traditional, indicator-based assessment of QoS allows to perform a basic evaluation of the data plan offered by the service provider (operator) to the user (customer). In such a method, the test equipment measures specific parameters



determining accessibility of services rendered with the use of the operator's network. Such an assessment offers reliable results for stationary users using dedicated data links (usually the cable). Research performed out in accordance with this method does not take into account, inter alia, limitations caused by the terminal or other user devices, and restrictions imposed by the service provider.

The presented method is not the best solution for evaluating mobile Internet access in a situation in which the operator does not guarantee the advertised access parameters, as these depend on the location, on the user's terminal, on the type of the network made available by the operator and on a range of other conditions. In this case, tests based on assessing the availability and reliability of services are more effective.

Transmission speed threshold values proposed in this paper should be amended in accordance with the needs of users when new transmission technologies are introduced. It is forecast that with the implementation and deployment of 5G networks offering significant transmission capabilities, the level of reliability of IT services will improve considerably.


## References

- [1] "TR 101 329. Telecommunications and Internet Protocol Harmonization Over Networks (TIPHON); General aspects of Quality of Service (QoS)" [Online]. Available: [https://www.etsi.org/deliver/etsi\\_tr/101300\\_101399/101329/02.01.01\\_60/tr\\_101329v020101p.pdf](https://www.etsi.org/deliver/etsi_tr/101300_101399/101329/02.01.01_60/tr_101329v020101p.pdf)
- [2] "Latin America. Mobile quality of service", *GSMA* [Online]. Available: <https://www.gsma.com/latinamerica/wp-content/uploads/2015/12/mobile-quality-of-service-latam-2015.pdf>
- [3] "ETSI EG 202 057-4. Speech processing, transmission and quality aspects (STQ); User related QoS parameter definitions and measurements" [Online]. Available: [https://www.etsi.org/deliver/etsi\\_eg/202000\\_202099/20205704/01.02.01\\_60/eg\\_20205704v010201p.pdf](https://www.etsi.org/deliver/etsi_eg/202000_202099/20205704/01.02.01_60/eg_20205704v010201p.pdf)
- [4] "Raport z prac realizowanych w ramach memorandum w sprawie współpracy na rzecz podnoszenia jakości usług na rynku telekomunikacyjnym", *UKE*, 2013, Warszawa [Online]. Available: <http://docplayer.pl/1641634-Raport-z-prac-realizowanych-w-ramach-memorandum-w-sprawie-wspolpracy-na-rzecz-podnoszenia-jakosci-uslug-na-rynku-telekomunikacyjnym.html> (in Polish)
- [5] E. Budiman and O. Wicaksono, "Measuring quality of service for mobile internet services", in *Proc. 2nd Int. Conf. on Sci. in Informat. Technol. (ICSITech)*, IEEE, Balikpapan, Indonesia, 2016 (DOI: 10.1109/ICSITech.2016.7852652).
- [6] B. Schmidt-Belz, M. Makelainen, A. Nick, and S. Poslad, "Intelligent brokering of tourism services for mobile users", in *Informat. and Commun. Technol. in Tourism*, K. Wöber, A. Frew, M. Hitz, Eds. pp. 275–284, Springer, 2002 (ISBN: 3211837809).
- [7] BEREC, "Guidelines detailing quality of service parameters" [Online]. Available: [https://berec.europa.eu/eng/document\\_register/subject\\_matter/berec/regulatory\\_best\\_practices/guidelines/9043-berec-guidelines-detailing-quality-of-service-parameters](https://berec.europa.eu/eng/document_register/subject_matter/berec/regulatory_best_practices/guidelines/9043-berec-guidelines-detailing-quality-of-service-parameters)
- [8] Directive (EU) 2018/1972 of the European Parliament and of the council of 11 December 2018 establishing the European Electronic Communications Code, *Official J. of the EU*, 2018 [Online]. Available: <https://eur-lex.europa.eu/legal-content/EN/TXT/PDF/?uri=CELEX:32018L1972&from=EN>
- [9] Recommendation ITU-T Y.2617, "Quality of service guaranteed mechanisms and performance model for public packet telecommunication data networks" [Online]. Available: <https://www.itu.int/rec/T-REC-Y.2617-201606-1/en>
- [10] "ETSI TR 103 559. Speech and multimedia Transmission Quality (STQ); Best practices for robust network QoS benchmark testing and scoring" [Online]. Available: [https://www.etsi.org/deliver/etsi\\_tr/103500\\_103599/103559/01.01.01\\_60/tr\\_103559v010101p.pdf](https://www.etsi.org/deliver/etsi_tr/103500_103599/103559/01.01.01_60/tr_103559v010101p.pdf)
- [11] M. Kowalewski, *Usługi Teleinformatyczne Administracji Publicznej*. Warszawa: OWPW, 2019 (ISBN: 9788378149323) (in Polish)
- [12] D. M. Curpen, M. Alexandru, and O. Croitoru, "Considerations about the reliability of telecommunications systems", in *Proc. 7th Int. Conf. on Electromechanical and Power Systems*, no. 33, Iași, Romania, 2009 [Online]. Available: <http://elth.ucv.ro/fisiere/anale/2009/11.pdf>
- [13] H. F. H. Omar, K. B. Saadan, and K. B. Seman, "Determining the influence of the reliability of service quality on customer satisfaction: the case of Libyan e-commerce customers", *Int. J. of Learning and Development*, vol. 5, no. 1, 2015 (DOI: 10.5296/ijld.v5i1.6649).
- [14] J. P. Carvallo and X. Franch, "Extending the ISO/IEC 9126-1 quality model with non-technical factors for COTS components selection", 2006 (DOI: 10.1145/1137702.1137706).
- [15] "A simple premise for a sophisticated methodology", *RootMetrics* [Online]. Available: <https://www.rootmetrics.com/en-US/methodology>
- [16] D. Hoyle, *ISO 9000: Quality Systems Handbook, 4th ed.* San Diego: Butterworth-Heinemann, 2001 (ISBN: 9780750644518).
- [17] R. Kobus, "Jakość usług telekomunikacyjnych czynnikiem kreującym rozwój społeczeństwa informacyjnego", *Ekonomiczne problemy łączności*, no. 12, pp. 197–209, Szczecin, Poland, 2011 (in Polish)
- [18] TELKO, "Rz: Nowy prezes UKE o rynku telekomunikacyjnym" [Online]. Available: <https://www.telko.in/rz-nowy-prezes-uke-o-rynku-telekomunikacyjnym> (in Polish)



**Marian Kowalewski** graduated from the Military Academy of Telecommunications in Żegrze (1975). He was an academic teacher, research worker and vice-chancellor for education and research at the same Academy (1975–1997), deputy director for science and general matters in NIT (1997–2004). He is a Professor at the National

Institute of Telecommunications and at Warsaw University of Technology. Head of TETRA project in NIT (since 2002), scientific manager of the IT System of the Country's Protection Against Extreme Hazards project (ISOK) in NIT (2011–2012), Intelligent Transport Systems (ITS) in NIT (2011–2013), cybersecurity (2014–2017). Organizer and co-organizer of many seminars and scientific conferences, author of numerous textbooks, academic course books, articles and R&D works concerning telecommunications problems. His scientific interests are planning and developing of telecommunications, telematics systems, and their efficiency.

 <https://orcid.org/0000-0001-6509-5141>

E-mail: [m.kowalewski@il-pib.pl](mailto:m.kowalewski@il-pib.pl)

National Institute of Telecommunications


Szachowa 1

04-894 Warsaw, Poland



**Ryszard Kobus** received his B.Sc. and M.Sc. degrees from the Faculty of Electronics of the Warsaw University of Technology in 1975. He worked at the National Institute of Telecommunications since 1975 to 2020. He is a member of the Expert Technical Committee CEN/TC 331 specializing in postal services, and the deputy

chairman of the Postal Service Committee PKN/TC 259. He is a co-author of many patented telecommunications solutions. His research interests include: telecommunications, measurements and evaluation of quality of telecommunications services, quality surveys, evaluation the quality of postal services, standardization.

 <https://orcid.org/0000-0001-7783-2794>

E-mail: [rys@r-kobus.eu](mailto:rys@r-kobus.eu)

National Institute of Telecommunications


Szachowa 1

04-894 Warsaw, Poland



**Tomasz Sędek** received his B.Sc. and M.Sc. degrees from the Faculty of Electronics and Information Technology of the Warsaw University of Technology in 1997. He has been working at the National Institute of Telecommunications since 1996. His research interests include: telecommunications, measurements and evaluation

of quality of telecommunications services, EMF measurements and analysis of results, statistical analysis of big data.

 <https://orcid.org/0000-0002-0416-4083>

E-mail: [t.sedek@il-pib.pl](mailto:t.sedek@il-pib.pl)

National Institute of Telecommunications

Szachowa 1

04-894 Warsaw, Poland

# Optimal Voting Rule and Minimization of Total Error Rate in Cooperative Spectrum Sensing for Cognitive Radio Networks

Samit Kumar Ghosh<sup>1</sup>, Sachin Ravikant Trankatwar<sup>1</sup>, and P. Bachan<sup>2</sup>

<sup>1</sup> Department of EEE, BITS, Pilani, Hyderabad Campus, Hyderabad, India

<sup>2</sup> Department of ECE, GLA University, Mathura, India

<https://doi.org/10.26636/jtit.2021.144420>

**Abstract**— In cognitive radio technology, spectrum sensing is essential for detecting spectrum holes which may be allotted to secondary users. In this paper, an optimal voting rule is used for cooperative spectrum sensing while minimizing the total error rate (TER). The proposed spectrum sensing method is more energy-efficient and may be implemented in practice. It is relied upon in an improved energy detector whose utilization depends on the presence or absence of the primary user. Expressions for false alarm and missed detection probabilities are derived in the paper as well. Overall performance is analyzed both for AWGN and Rayleigh fading channels, in the presence of additive white Gaussian noise (AWGN). The optimum voting rule is applied to the cooperative spectrum sensing process in order to identify the optimum number of sensing nodes and the detection threshold. Finally, an energy-efficient spectrum sensing algorithm is proposed, requiring a lower number of cognitive users for a given error bound.

**Keywords**—cognitive radio, energy detection, optimization, spectrum sensing.

## 1. Introduction

Efficient utilization of the spectrum is a primary requirement in current and future wireless communication systems. Exponential increase in the number of mobile services and smartphones requires a continued expansion of the spectrum resources [1], [2]. Hence, wireless multicasting techniques are used to transmit the same data to a group of users connected to the same base station, as such an approach is spectrally more efficient compared to wireless unicasting techniques [3]. Spectral efficiency may also be increased by using the non-utilized licensed spectrum assigned to primary users (PU). These spectra are non-continuous and are allocated dynamically to secondary users (SU) [4], [5]. Cognitive radio (CR) has been considered as a promising technique with this respect. CR is a software-defined technology, where the unused spectrum or the spectrum holes of the radio band owned by PU are detected and then as-

signed to SU for the transmission of their data [6], [7]. Spectrum sharing (SS) is another popular method. In this approach, SU is allowed to coexist with PU within the same band, without violating interference temperature (IT) restrictions [8], [9]. This technique is commonly known as the underlay spectrum sharing mode [10]. An optimized power allocation approach enhances SS capacity, both for PUs and cognitive radio network (CRN) [11]. This power allocation strategy is constrained by primary link outage probability (OP), which significantly improves the throughput of SU by considering the PU's QoS-related constraint, and hardly considering the IT constraint [12].

Spectrum hole sensing is one of the key problems of CR, as a single CR cannot sense the PU's spectrum holes reliably due to low SNR, multi-path fading, shadowing, and sensing time-related constraints. Hence, spectrum sensing needs to be performed by multiple CR users [13]–[15]. The cooperative spectrum sensing (CSS) mechanism is one of the most advanced spectrum sensing methods used in CR, where multiple SUs are allowed to use spectrum holes of the PU by relying on the co-operative mechanism [16]–[18]. In CSS, SUs sense the presence of the PU's spectrum holes and send the relevant information to the fusion center (FC), where the final decision is made. The primary objective of the CR is to utilize the unused spectrum of the PU without interfering with the PU, so that spectrum utilization may be improved [19]. In CR, energy detection is one of the most effective spectrum sensing methods, as it may compare the energy-related statistics of the received signal with a predefined threshold and is capable of deciding whether the spectrum is available or not [20]. Performance of the energy detection mechanism may be measured by relying on detection probability and false alarm probability [21], [22]. The analysis of this energy detector comes in handy for emerging applications, including ultra-wideband and cognitive radio technologies. Spectrum access may be increased in CR by reducing false alarm probability, and interference suffered by PU will de-

crease as detection probability improves. However, the important task is to establish a relationship between the two probabilities i.e. the probability of detecting  $P_d$  and the probability of false alarm  $P_f$ , by selecting an appropriate detection threshold. To ensure the best performance detection results, CSS is used. Multiple cognitive users (CU) are used and their observations are combined at the fusion center, using a voting rule.

The key contributions of this paper are as follows.

1. Analytical frameworks are formed for the optimality of CSS, utilizing the detecting channel in CR and the primary transmitter when energy detection and distributed decision fusion are applied to a CRN.
2. Optimal detection threshold is derived to minimize the total error rate (TER).
3. The optimum voting rule i.e. the optimal value of  $n$  for the  $n$ -out-of- $N$  is studied, both in AWGN and in the Rayleigh fading channel.
4. The optimal number of CRs are is required in CSS with large CRN to achieve the target error bound.

Following this introduction, the remaining part of the paper is organized as follows: Section 2 introduces the model of the system. Section 3 presents optimization of cooperative spectrum sensing, along with numerical results and discussions. Finally, conclusions are drawn in Section 4.

## 2. System Model

We consider a centralized CSS architecture in a CR network with an erroneous sensing/reporting channel, presented in Fig. 1, consisting of a PU,  $N$  number of CR (SUs), and an FC. All SUs coordinate and collaborate with each other and finally forward their local binary decisions (i.e. 0 or 1) to the FC through the erroneous reporting channel. Based on the received observations, the FC decides about spectrum access. Each CU performs spectrum sensing and, based on the presence or lack of presence of a PU, a binary deci-

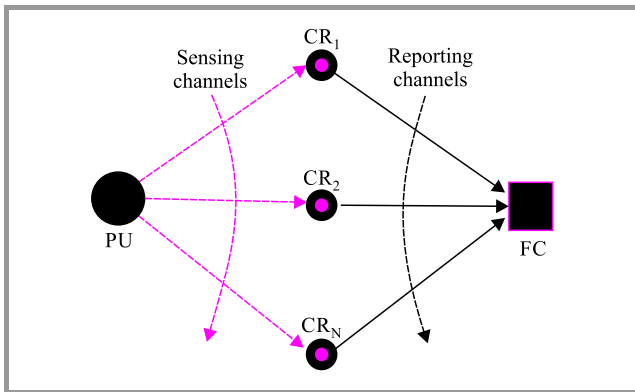


Fig. 1. Centralized CSS architecture in a CRN with erroneous reporting channel.

sion is made between the subsequent two hypotheses ( $H_0$  – absence of PU,  $H_1$  – presence of PU):

$$r_j(t) = \begin{cases} n_j(t), & H_0 \\ h_j(t)s(t) + n_j(t), & H_1 \end{cases} \quad (1)$$

In Eq. (1),  $j$  is the antenna index,  $j \in \{1, 2, \dots, N\}$  at each CR,  $s(t)$  denotes the signal transmitted by the PU with energy  $E_s$ ,  $n_j(t) \sim \mathcal{CN}(0, \sigma_n^2)$  is the circularly symmetric complex additive white Gaussian noise, where  $\mathcal{CN}(\cdot)$  denotes the complex normal distribution and  $h_j(t) \sim \mathcal{CN}(0, \sigma_h^2)$  represents the complex valued channel coefficient. Taking into account the assumption that, during the spectrum sensing process, sensing channel  $h_j(t)$  is time-invariant and the activities of the PU remain unchanged, energy  $r_j$  is taken as a decision statistic that has the following distribution:

$$r_j = \begin{cases} \chi_{2u}^2, & H_0 \\ \chi_{2u}^2(2\gamma_j), & H_1 \end{cases}, \quad (2)$$

where  $\chi_{2u}^2$  denotes a central chi-square distribution with  $2u$  degrees of freedom, which equals to twice the time-bandwidth product  $2TW$ , while  $\chi_{2u}^2(2\gamma_j)$  denotes a non-central chi-square distribution with the same number of degrees of freedom and a non-centrality parameter  $2\gamma_j$ , which equals to twice the instantaneous SNR of the  $j$ -th CR. The average probability of false alarm  $P_{f,j}$ , probability of detection  $P_{d,j}$ , and probability of missed detection  $P_{m,j}$  over AWGN channels in the energy detector for  $j$ -th CR are given, respectively, by [23]:

$$P_{f,j} = \frac{\Gamma(u, \frac{\lambda_j}{2})}{\Gamma(u)}, \quad (3)$$

$$P_{d,j} = Q_u(\sqrt{2\gamma_j}, \sqrt{\lambda_j}) \quad (4)$$

and

$$P_{m,j} = 1 - P_{d,j}. \quad (5)$$

In Eqs. (3)–(4) parameters  $u$ ,  $\gamma_i$ , and  $\lambda_i$  signify the time-bandwidth product, instantaneous signal-to-noise (SNR) ratio and energy detection threshold at the  $j$ -th CR, respectively.  $\Gamma(a, b)$ , and  $Q_u(p, q)$  are the incomplete gamma function and the generalized Marcum Q-function, respectively [24], [25],

$$\Gamma(a, b) = \int_b^\infty t^{a-1} e^{-t} dt,$$

and

$$Q_u(p, q) = \frac{1}{p^{u-1}} \int_q^\infty t^u e^{-\frac{t^2+p^2}{2}} I_{u-1}(pt) dt, \text{ with } I_{u-1}(\cdot)$$

is the modified Bessel's function of  $(u-1)$ -th order. In wireless communication systems,  $P_f$  will depend on the channel only. Path distribution and SNR will not affect it.

Hence, in Rayleigh fading distribution,  $P_f$  remains the same as AWGN in Eq. (3) and  $P_d$  is given by:

$$P_d = e^{-\frac{\lambda}{2}} \sum_{n=0}^{u-1} \frac{1}{n!} \left(\frac{\lambda}{2}\right)^n + \left(\frac{1+\bar{\gamma}}{\bar{\gamma}}\right)^{u-1} \times \left[ e^{-\frac{\lambda}{2(1+\bar{\gamma})}} - e^{-\frac{\lambda}{2}} \sum_{n=0}^{u-1} \frac{1}{n!} \left(\frac{\lambda\bar{\gamma}}{2(1+\bar{\gamma})}\right)^n \right]. \quad (6)$$

Using the relation  $\Gamma(a, x) = (a-1)! e^{-x} \sum_{n=0}^{a-1} \frac{x^n}{n!}$ , i.e. a gamma function that is incomplete in terms of generalized Laguerre polynomials, the Eq. (6), may be written as:

$$P_d = \left[ \frac{\Gamma\left(u-1, \frac{\lambda}{2}\right)}{(u-2)!} \right] + \left(\frac{1+\bar{\gamma}}{\bar{\gamma}}\right)^{u-1} e^{-\frac{\lambda}{2(1+\bar{\gamma})}} \times \left[ 1 - \frac{\Gamma\left(u-1, \frac{\lambda\bar{\gamma}}{2(1+\bar{\gamma})}\right)}{(u-2)!} \right]. \quad (7)$$

In CSS, the FC employs various hard decision-combining operations (OR, AND, majority rule) based on the received binary decision  $D_j \in \{0, 1\}$  (0 – absence of PU, 1 – presence of PU) and gives the final status (inactive/active) through the erroneous reporting channel. According to the  $n$ -out-of- $N$  rule, all 1-bit decisions are fused together at the common receiver.

$$\Delta = \sum_{j=1}^N D_j \begin{cases} \geq n, & H_1 \\ < n, & H_0 \end{cases}, \quad (8)$$

where the integer  $n$  is the threshold of the  $n$ -out-of- $N$  voting rule that indicates the OR rule when  $n = 1$  and corresponds to the AND rule when  $n = N$ . We assume that the distance between any two CRs is small compared to the distance from any CR to the primary transmitter, which implies that all CRs exhibit identical path losses. Therefore, we can conclude that in an AWGN environment,  $\gamma_1 = \gamma_2 = \dots \gamma_N = \gamma = \bar{\gamma}$  and in the case of Rayleigh fading, the instantaneous SNRs are identically distributed with their mean value of  $\bar{\gamma}$ . In fact, we suppose that all CRs use the same threshold  $\lambda$ , implying that  $\lambda_1 = \lambda_2 = \dots \lambda_k = \lambda$ . This implies that  $P_{d,i}$ ,  $P_{f,i}$ , and  $P_{m,i}$  being independent of  $i$  in both fading and non-fading channels. Therefore,  $P_{d,i} = P_d$ ,  $P_{f,i} = P_f$ , and  $P_{m,i} = P_m$ . For both kinds of environments, we have  $P_m = 1 - P_d$ . The false alarm and miss detection probability of CSS are expressed as:

$$Q_f = P(H_1|H_0) = \sum_{l=n}^N \binom{N}{l} P_f^l (1 - P_f)^{N-l}, \quad (9)$$

$$Q_m = P(H_0|H_1) = 1 - \sum_{l=n}^N \binom{N}{l} P_d^l (1 - P_d)^{N-l}. \quad (10)$$

### 3. Optimization of Cooperative Spectrum Sensing

In this section, we study the optimality of CSS when energy detection and decision fusions are applied.

#### 3.1. Optimal Voting Rule

An exact solution to obtain the optimal number of CR is required to minimize the TER i.e.  $Q_f + Q_m$  based on the following theorem.

**Theorem 1:** Given fixed number of  $N$ , the optimal voting rule for cooperative spectrum sensing that minimizes  $Q_f + Q_m$  is  $n_{\text{opt}} = \min(N, \lceil \frac{N}{1+\alpha} \rceil)$  where,  $\alpha = \frac{\ln \frac{P_f}{1-P_m}}{\ln \frac{P_m}{1-P_f}}$  and  $\lceil \cdot \rceil$  denotes the ceiling function.

**Proof:** Let  $F(n)$  be a function given by:

$$F(n) = \sum_{l=n}^N \binom{N}{l} \left[ P_f^l (1 - P_f)^{N-l} - (1 - P_m)^l P_m^{N-l} \right]. \quad (11)$$

Combining Eqs. (9) and (10), we get  $Q_f + Q_m = 1 + F(n)$ . Then, we have

$$\frac{\partial F(n)}{\partial n} \approx F(n+1) - F(n) = \binom{N}{n} \left[ (1 - P_m)^n P_m^{N-n} - P_f^n (1 - P_f)^{N-n} \right]. \quad (12)$$

The optimum value of  $n$  is obtained when  $\frac{\partial F(n)}{\partial n} = 0$ , i.e. when

$$(1 - P_m)^n P_m^{N-n} = P_f^n (1 - P_f)^{N-n}. \quad (13)$$

$$\text{Let } \alpha = \frac{\ln \frac{P_f}{1-P_m}}{\ln \frac{P_m}{1-P_f}}.$$

Then, after simplifying and re-arranging, we obtain  $n \approx \lceil \frac{N}{1+\alpha} \rceil$  which is a function of  $P_f$  and  $P_m$ . From the proportion, we can conclude that:

1. The optimum value of  $n$  is  $\frac{N}{2}$ . This can be achieved when  $\frac{P_f}{P_m} = 1$ , i.e.  $\alpha = 1$ .
2. The OR rule is optimal when the parameter  $\alpha \geq N - 1$ . This can be achieved when  $\frac{P_f}{P_m} \ll 1$ , i.e. for very large values of  $\lambda$ .
3. The AND rule is optimal when  $\alpha = 0$ . This can be achieved when  $\frac{P_f}{P_m} \gg 1$ , i.e. for very small values of  $\lambda$ .

Here, we consider the 10 voting rules between  $n = 1$  and  $n = 10$  for  $N = 10$  and calculate the TER at SNR=10 dB by considering the AWGN and Rayleigh fading channels. Figure 2 shows the plot of the TER versus the detection threshold, considering different voting rules between  $n = 1$  and  $n = 10$  in a CR network with 10 users, for both channels, respectively. It may be observed from Fig. 2a–b that to achieve the minimum error optimum value of the threshold,  $n = 5$  for AWGN and  $n = 2$  for the Rayleigh fading channel. However, the OR rule i.e.  $n = 1$ , and AND rule, i.e.  $n = 10$ , tends to be optimal for very large and very small thresholds, respectively.

Table 1 presents the optimum values of  $n$ , threshold ( $\lambda$ ) and TER ( $Q_f + Q_m$ ), respectively, for various network parameters. From Table 1, it can be found that threshold

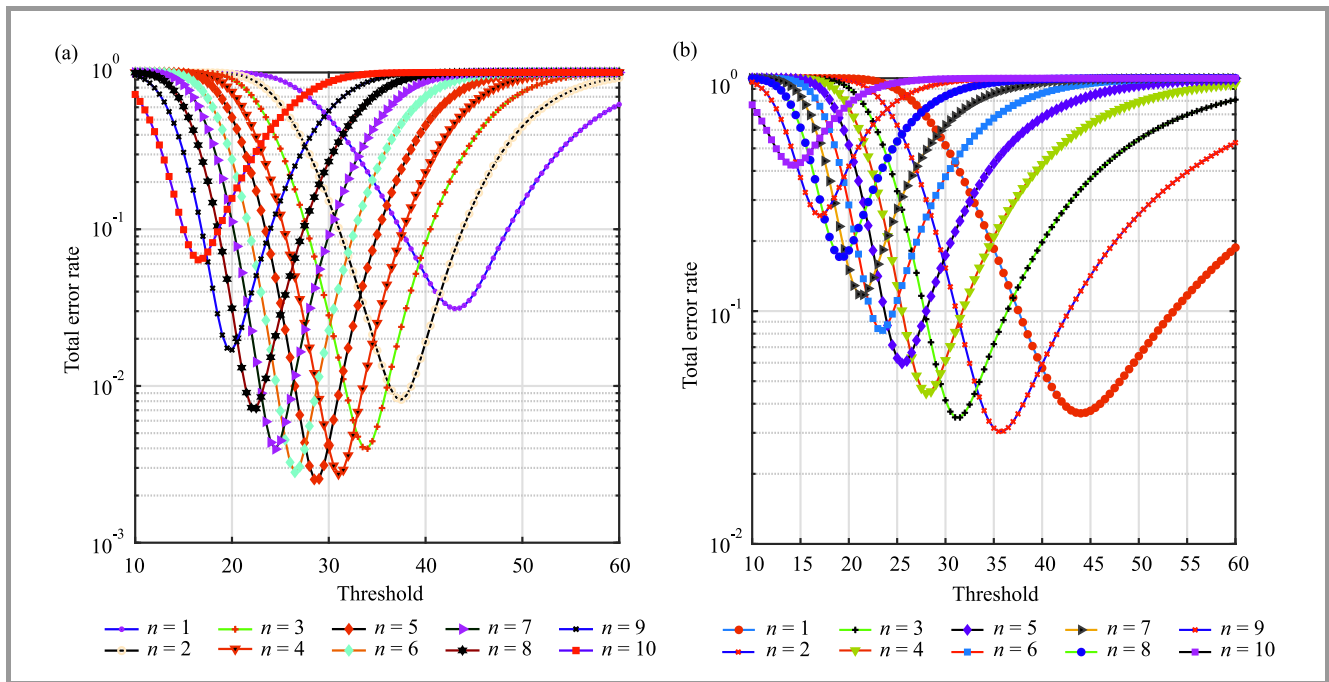


Fig. 2. Total error rate vs. threshold for AWGN channel (a) and total error rate vs. threshold for Rayleigh fading channel (b). (For color pictures see the digital version of the paper).

Table 1  
Comparison of TER for different threshold values for SNR = 10 dB

Channel	$n$	1	2	3	4	5	6	7	8	9	10
AWGN	Threshold	43.0	37.5	34.0	31.0	<b>28.5</b>	26.5	24.5	22.5	20.0	17.0
	TER	0.0311	0.0082	0.0040	0.0027	<b>0.0025</b>	0.0028	0.0040	0.0072	0.0170	0.0652
Rayleigh fading	Threshold	44.0	<b>35.5</b>	31.5	28.0	25.5	23.5	21.5	19.0	17.0	14.5
	TER	0.0364	<b>0.0304</b>	0.0349	0.0444	0.0596	0.0826	0.1175	0.1711	0.2573	0.4236

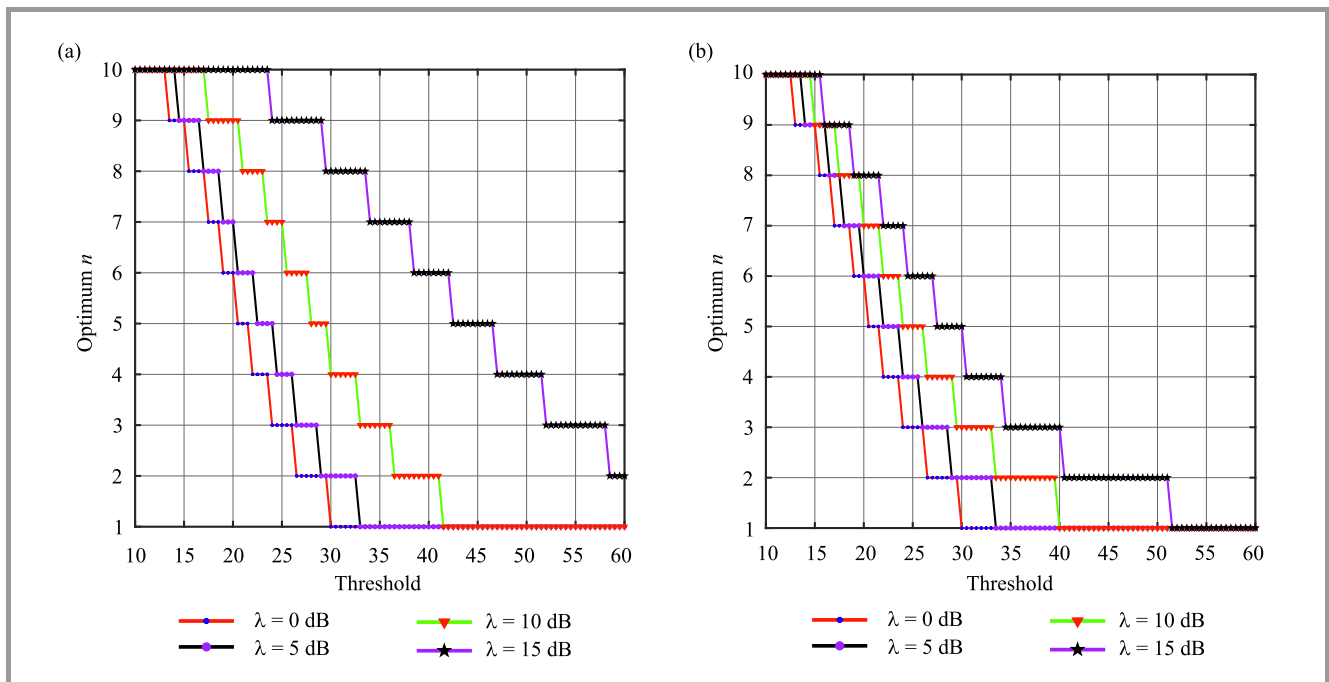


Fig. 3. Optimum voting rule vs. detection threshold for AWGN channel (a) and optimum voting rule vs. detection threshold for Rayleigh fading channel (b).



values decrease as the number of cognitive users increases at SNR = 10 dB in the case of both non-fading and fading channels. We also observe that minimization of TER occurs at  $\lambda = 28.5$  and  $n = 5$  in AWGN channel, and in the case of the Rayleigh fading channel, at  $\lambda = 35.5$  and  $n = 2$ .

Figure 3a–b shows the optimum voting rule versus detection threshold in the AWGN channel and the Rayleigh fading channel, respectively. It offers the exact solution of  $n$  in terms of the detection threshold for SNR = 0, 5, 10, 15 dB and  $N = 10$ . It is evident that, as SNR increases, the optimum number of cooperative SUs increases, and that as the detection threshold increases, the optimum number of cooperative SUs decreases with the SNR.

### 3.2. Optimum Energy Detection Threshold

We could observe in Fig. 2a–b that the TER curve of  $Q_f + Q_m$  in for a wide range of thresholds  $\lambda$  for the AWGN channel and the Rayleigh fading channel, respectively, considering different voting rules from  $n = 1$  to 10 in a CR network. This indicates that for the minimization of  $Q_f + Q_m$  only one value of  $\lambda$  exists. The optimal threshold is given by  $\lambda^{opt} = \text{minimized}(Q_f + Q_m)$ , which is achieved when

$$\frac{\partial Q_m}{\partial \lambda} + \frac{\partial Q_f}{\partial \lambda} = 0.$$

From Eq. (9) we can obtain the following:

$$\begin{aligned} \frac{\partial Q_f}{\partial \lambda} &= \sum_{l=n}^N \binom{N}{l} l P_f^{l-1} \frac{\partial P_f}{\partial \lambda} (1 - P_f)^{N-l} \\ &\quad - \sum_{l=n}^N \binom{N}{l} P_f^l (N-l) (1 - P_f)^{N-l-1} \frac{\partial P_f}{\partial \lambda} \\ &= \frac{\partial P_f}{\partial \lambda} \sum_{l=n}^N \binom{N}{l} P_f^{l-1} (1 - P_f)^{N-l} \\ &\quad \times \left[ l - (N-l) \frac{P_f}{1 - P_f} \right]. \end{aligned} \quad (14)$$

From Eq. (3), we obtain  $\frac{\partial P_f}{\partial \lambda}$ :

$$\frac{\partial P_f}{\partial \lambda} = \frac{\partial}{\partial \lambda} \frac{\Gamma(u, \frac{\lambda}{2})}{\Gamma(u)} = -\frac{1}{(u-1)!} \frac{\lambda^{u-1}}{2^u} e^{-\frac{\lambda}{2}}. \quad (15)$$

From Eq. (10), we can get:

$$\begin{aligned} \frac{\partial Q_m}{\partial \lambda} &= -\sum_{l=n}^N \binom{N}{l} l P_d^{l-1} \frac{\partial P_d}{\partial \lambda} (1 - P_d)^{N-l} \\ &\quad + \sum_{l=n}^N \binom{N}{l} P_d^l (N-l) (1 - P_d)^{N-l-1} \frac{\partial P_d}{\partial \lambda} \\ &= -\frac{\partial P_d}{\partial \lambda} \sum_{l=n}^N \binom{N}{l} P_d^{l-1} (1 - P_d)^{N-l} \\ &\quad \times \left[ l - (N-l) \frac{P_d}{1 - P_d} \right]. \end{aligned} \quad (16)$$

The detection probability of the AWGN channel is [23]:

$$\begin{aligned} P_d &= Q_u(\sqrt{2\gamma}, \sqrt{\lambda}) \\ &= \frac{1}{(\sqrt{2\gamma})^{u-1}} \int_{\sqrt{\lambda}}^{\infty} x^u e^{-\frac{x^2+2\gamma}{2}} I_{u-1}(\sqrt{2\gamma}x) dx. \end{aligned} \quad (17)$$

From Eq. (17), we obtain:

$$\frac{\partial P_d}{\partial \lambda} = -\frac{\lambda^{\frac{u-1}{2}}}{2(2\gamma)^{\frac{u-1}{2}}} e^{-\frac{\lambda+2\gamma}{2}} I_{u-1}(\sqrt{2\gamma\lambda}). \quad (18)$$

The detection probability of the Rayleigh fading channel is given in Eq. (7). Note that,  $\Gamma(a, x) = \int_x^{\infty} t^{a-1} e^{-t} dt$  and  $\frac{\partial \Gamma(a, x)}{\partial x} = -x^{a-1} e^{-x}$ .

Then:

$$\frac{\partial \Gamma(u-1, \frac{\lambda}{2})}{\partial \lambda} = -\frac{1}{2} \left(\frac{\lambda}{2}\right)^{u-2} e^{-\frac{\lambda}{2}}. \quad (19)$$

$$\frac{\partial \Gamma(u-1, \frac{\lambda\bar{\gamma}}{2(1+\bar{\gamma})})}{\partial \lambda} = -\frac{1}{2} \frac{\bar{\gamma}}{1+\bar{\gamma}} \left(\frac{\lambda\bar{\gamma}}{2(1+\bar{\gamma})}\right)^{u-2} e^{-\frac{\lambda\bar{\gamma}}{2(1+\bar{\gamma})}}. \quad (20)$$

Now consider

$$A_1 = \Gamma\left(u-1, \frac{\lambda}{2}\right)$$

and

$$B_1 = \Gamma\left(u-1, \frac{\lambda\bar{\gamma}}{2(1+\bar{\gamma})}\right).$$

By differentiating Eq. (7) w.r.t  $\lambda$ , we get:

$$\begin{aligned} \frac{\partial P_d}{\partial \lambda} &= \frac{\partial A_1}{\partial \lambda} + \left(\frac{1+\bar{\gamma}}{\bar{\gamma}}\right)^{u-1} \frac{e^{-\frac{\lambda}{2(1+\bar{\gamma})}}}{2(1+\bar{\gamma})} \\ &\quad \left[ 1 - \frac{B_1}{(u-2)!} \right] - \frac{\partial B_1}{\partial \lambda} \left(\frac{1+\bar{\gamma}}{\bar{\gamma}}\right)^{u-1} e^{-\frac{\lambda}{2(1+\bar{\gamma})}}. \end{aligned} \quad (21)$$

Simplifying first term and the third term, using Eqs. (19) and (20) in Eq. (21), we can write:

$$\frac{\partial P_d}{\partial \lambda} = \left(\frac{1+\bar{\gamma}}{\bar{\gamma}}\right)^{u-1} \frac{e^{-\frac{\lambda}{2(1+\bar{\gamma})}}}{2(1+\bar{\gamma})} \left[ \frac{\Gamma(u-1, \frac{\lambda\bar{\gamma}}{2(1+\bar{\gamma})})}{(u-2)!} - 1 \right]. \quad (22)$$

Further, using Eq. (7), we obtain:

$$\frac{\partial P_d}{\partial \lambda} = \frac{1}{2(1+\bar{\gamma})} \left[ \frac{\Gamma(u-1, \frac{\lambda}{2})}{(u-2)!} - P_d \right]. \quad (23)$$

The solution to  $\frac{\partial Q_m}{\partial \lambda} + \frac{\partial Q_f}{\partial \lambda} = 0$  (for  $\lambda$ ) can be calculated using Eqs. (14) and (16).

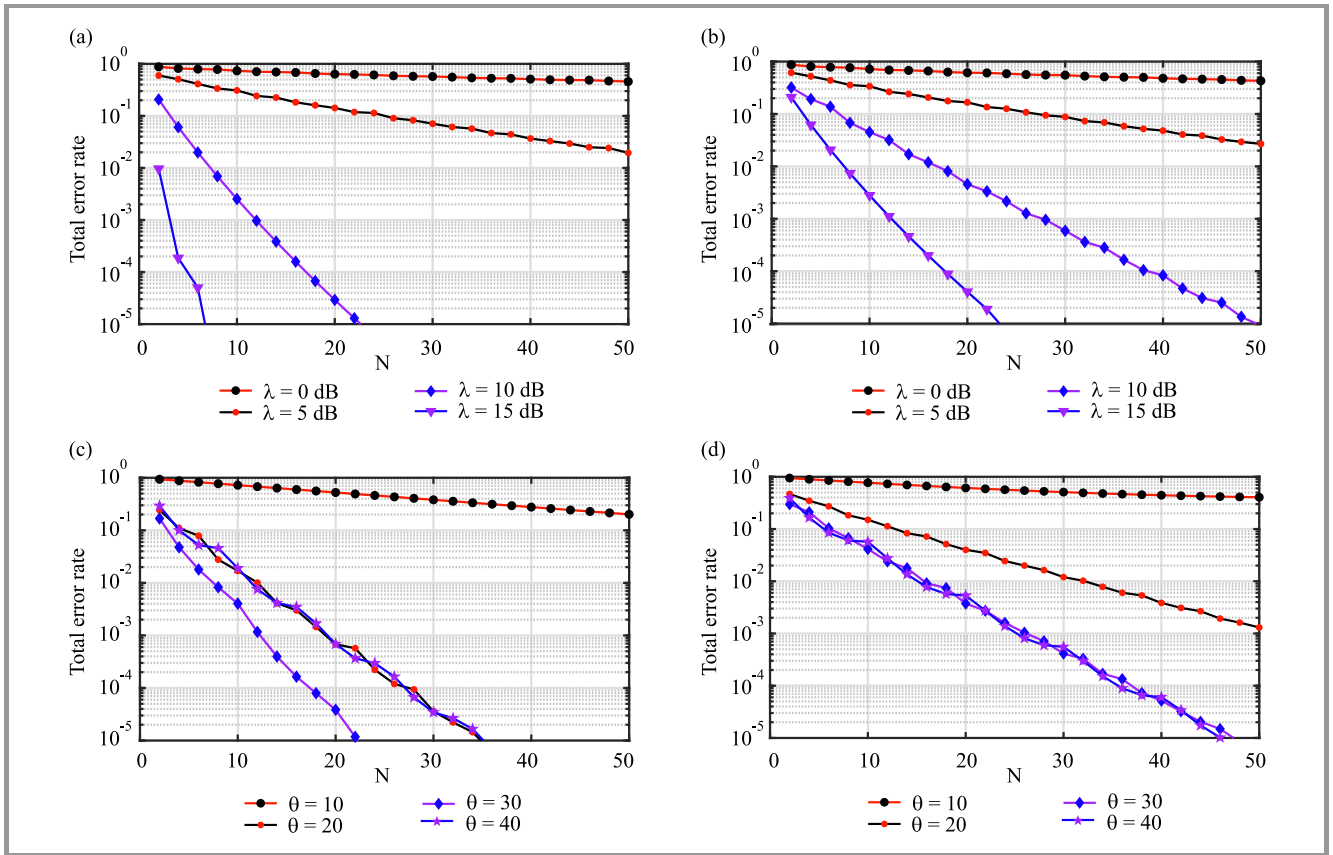


**Fig. 4.** Total error rate of CSS versus number of collaborating CRs in a network with 50 CRs in: (a) AWGN with SNR = 0–20 dB for  $\lambda = 28.5$ , (b) Rayleigh fading with SNR = 0–20 dB for  $\lambda = 28.5$ , (c) AWGN with SNR = 10 dB for  $\lambda = 10$ –40, (d) Rayleigh fading with SNR = 10 dB for  $\lambda = 10$ –40.

### 3.3. Optimal Number of Cognitive Radios

CSS become impractical when the number of CRs is higher in a CRN. So, for a particular specified time period, only one CR is capable of sending its local decision to the common receiver and of splitting the decision without difficulty at the end of the receiver. This problem may be tended to by enabling the CRs to transmit their choices simultaneously. But this causes difficulties related to the design of the receiver at the time of sorting out the decisions from various types of CRs.

Another possible option is to make choices concerning orthogonal frequency ranges, but that involves a significant portion of the usable bandwidth.

To resolve these problems, we suggest an effective sensing algorithm that relies on the transmission of judgment for one CR using one time slot, but retains a minimum error bound by allowing a few CRs in CSS, instead of all of them. First of all, we assume that to satisfy  $Q_m + Q_f \leq \varepsilon$ , the minimum number of CRs required in CSS is  $\tilde{n}^*$  ( $1 \leq \tilde{n}^* \leq N$ ). The optimal voting rule obtained from Theorem 1 for CSS with  $\tilde{n}^*$  CR is  $n_{\tilde{n}^*}^{opt} = \min\left(\tilde{n}^*, \left\lceil \frac{\tilde{n}^*}{1+\alpha} \right\rceil\right)$  where  $\alpha$  is related to  $P_f$  and  $P_m$ , and may be evaluated by giving the value of  $\lambda$  and the SNR. Let us define function  $F(\cdot, \cdot)$  in terms of variable as  $F(\tilde{n}, n_{\tilde{n}}^{opt}) = Q_f + Q_m - \varepsilon$ , where  $\tilde{n}$  denotes the number of cooperative CRs in CSS. Probabilities  $Q_f$  and

$Q_m$  are the functions of  $\tilde{n}$ , and  $n_{\tilde{n}}^{opt}$  are given by Eqs. (9) and (10), respectively. Then, we have  $F(\tilde{n}, n_{\tilde{n}}^{opt}) \leq 0$  and  $F(\tilde{n} - 1, n_{\tilde{n}-1}^{opt}) \geq 0$ .

Using these properties, we can obtain  $\tilde{n}^* = \lceil \tilde{n}_0 \rceil$ , where  $\tilde{n}_0$  represents the first zero-crossing point of the curve  $F(\tilde{n}, n_{\tilde{n}}^{opt})$  in terms of  $\tilde{n}$ . Therefore, it is possible to formulate a rapid spectrum sensing algorithm by only considering  $\tilde{n}^*$  in CSS instead of  $N$ . As a result, the duration of sensing can be reduced from  $N$  time slots to  $\tilde{n}^*$  time slots, while this error bound  $\varepsilon$  is guaranteed. To achieve a  $TER Q_f + Q_m < 0.01$ , the smallest number of CRs required is 2 and 7 for SNR values of 15 dB and 10 dB, respectively, with a fixed decision threshold of  $\lambda = 28.5$  over the AWGN channel. However, in the Rayleigh fading channel, the minimum values of CRs are 7 for 15 dB and 17 for 10 dB. Figure 4 shows the CSS error rate according to  $Q_f(N, n) + Q_m(N, n)$  with respect to specific  $N$  when the optimum voting rule  $n = n_{\tilde{n}}^{opt} = \min\left(N, \left\lceil \frac{N}{1+\alpha} \right\rceil\right)$  is implemented. This implies that it is necessary to employ limited cooperation in order to achieve the level of service needed.

Figure 4c and Fig. 4d demonstrate another example. It is observed that at SNR values of 10 dB and for the given error rate of 0.01, the number of CRs considered for threshold values of 30, 40, and 20 is 7, 11, and 12, respectively for



the AWGN channel, and 15, 16, and 32 for the threshold values of 40, 30, and 20.

## 4. Conclusion

In this work, we investigated the performance of cooperative spectrum sensing with energy detection. We derive the expression for the optimum value of  $n$  that minimizes the TER by applying the  $n$ -out-of- $N$  voting rule. The numerical expression for obtained the optimal detection threshold obtained has been discussed as well. In addition, an effective spectrum sensing algorithm has been proposed that needs less than the total number of cognitive radios in the cooperative spectrum sensing, thus fulfilling the specified bound error.

## References

- [1] S. Haykin, "Cognitive radio: brain-empowered wireless communications", *IEEE J. on Selec. Areas in Commun.*, vol. 23, no. 2, pp. 201–220, 2005 (DOI: 10.1109/JSAC.2004.839380).
- [2] Y.-C. Liang, Y. Zeng, E. C. Peh, and A. T. Hoang, "Sensing-throughput tradeoff for cognitive radio networks", *IEEE Trans. on Wirel. Commun.*, vol. 7, no. 4, pp. 1326–1337, 2008 (DOI: 10.1109/TWC.2008.060869).
- [3] K. Poularakis, G. Iosifidis, V. Sourlas, and L. Tassiulas, "Exploiting caching and multicast for 5G wireless networks", *IEEE Trans. on Wirel. Commun.*, vol. 15, no. 4, pp. 2995–3007, 2016 (DOI: 10.1109/TWC.2016.2514418).
- [4] F. Haider *et al.*, "Spectral and energy efficiency analysis for cognitive radio networks", *IEEE Trans. on Wirel. Commun.*, vol. 14, no. 6, pp. 2969–2980, 2015 (DOI: 10.1109/TWC.2015.2398864).
- [5] M. Klymash, M. Jo, T. Maksymuk, and I. Beliaiev, "Spectral efficiency increasing of cognitive radio networks", in *Proc. 12th Int. Conf. on the Exper. of Desig. and Appl. of CAD Syst. in Microelectron. CADSM 2013*, Polyana Svalyava, Ukraine 2013, pp. 169–171 (ISBN: 9781467364614).
- [6] J. Mitola and G. Q. Maguire, "Cognitive radio: making software radios more personal", *IEEE Pers. Commun.*, vol. 6, no. 4, pp. 13–18, 1999 (DOI: 10.1109/98.788210).
- [7] B. Wang and K. R. Liu, "Advances in cognitive radio networks: A survey", *IEEE J. of Selec. Topics in Sig. Process.*, vol. 5, no. 1, pp. 5–23, 2010 (DOI: 10.1109/JSTSP.2010.2093210).
- [8] T. Yucek and H. Arslan, "A survey of spectrum sensing algorithms for cognitive radio applications", *IEEE Commun. Surv. & Tutor.*, vol. 11, no. 1, pp. 116–130, 2009 (DOI: 10.1109/SURV.2009.090109).
- [9] M. S. Falih and H. N. Abdullah, "A combined spectrum sensing method based DCT for cognitive radio system", *Int. J. of Elec. & Comp. Engin.*, vol. 10, no. 2, pp. 1935–1942, 2020 (DOI: 10.11591/ijece.v10i2.pp1935-1942).
- [10] I. F. Akyildiz, W.-Y. Lee, M. C. Vuran, and S. Mohanty, "Next generation/dynamic spectrum access/cognitive radio wireless networks: A survey", *Computer Networks*, vol. 50, no. 13, pp. 2127–2159, 2006 (DOI: 10.1016/j.comnet.2006.05.001).
- [11] X. Kang, Y.-C. Liang, A. Nallanathan, H. K. Garg, and R. Zhang, "Optimal power allocation for fading channels in cognitive radio networks: Ergodic capacity and outage capacity", *IEEE Trans. on Wirel. Commun.*, vol. 8, no. 2, pp. 940–950, 2009 (DOI: 10.1109/TWC.2009.071448).
- [12] K. B. Letaief and W. Zhang, "Cooperative communications for cognitive radio networks", *Proc. of the IEEE*, vol. 97, no. 5, pp. 878–893, 2009 (DOI: 10.1109/JPROC.2009.2015716).
- [13] G. Zhao, G. Y. Li, C. Yang, and J. Ma, "Proactive detection of spectrum holes in cognitive radio", in *Proc. of IEEE Int. Conf. on Commun.*, Dresden, Germany, 2009 (DOI: 10.1109/JPROC.2009.2015716).
- [14] W. Zhang, R. K. Mallik, and K. B. Letaief, "Optimization of cooperative spectrum sensing with energy detection in cognitive radio networks", *IEEE Trans. on Wirel. Commun.*, vol. 8, no. 12, pp. 5761–5766, 2009 (DOI: 10.1109/TWC.2009.12.081710).
- [15] S. K. Ghosh and P. Bachan, "Performance evaluation of spectrum sensing techniques in cognitive radio network", *IOSR J. of Electron. and Commun. Engin. (IOSR-JECE)*, vol. 12, no. 4, pp. 17–21, 2017 (DOI: 10.9790/2834-1204051721).
- [16] I. F. Akyildiz, B. F. Lo, and R. Balakrishnan, "Cooperative spectrum sensing in cognitive radio networks: A survey", *Phys. Commun.*, vol. 4, no. 1, pp. 40–62, 2011 (DOI: 10.1016/j.phycom.2010.12.003).
- [17] G. Verma and O. Sahu, "A distance based reliable cooperative spectrum sensing algorithm in cognitive radio", *Wirel. Pers. Commun.*, vol. 99, no. 1, pp. 203–212, 2018 (DOI: 10.1007/s11277-017-5052-z).
- [18] P. Bachan, S. K. Ghosh, and S. K. Saraswat, "Comparative error rate analysis of cooperative spectrum sensing in non-fading and fading environments", in *Proc. of Commun., Contr. and Intell. Syst. CCIS 2015*, Mathura, India, 2015 pp. 124–127, 2015 (DOI: 10.1109/CCIntelS.2015.7437891).
- [19] W. Zhang and K. B. Letaief, "Cooperative spectrum sensing with transmit and relay diversity in cognitive radio networks", *IEEE Trans. on Wirel. Commun.*, vol. 7, no. 12, pp. 4761–4766, 2008 (DOI: 10.1109/T-WC.2008.060857).
- [20] S. K. Ghosh, J. Mehedi, and U. C. Samal, "Sensing performance of energy detector in cognitive radio networks", *Int. J. of Inf. Technol.*, vol. 11, no. 4, pp. 773–778, 2019 (DOI: 10.1007/s41870-018-0236-7).
- [21] S. Atapattu, C. Tellambura, and H. Jiang, "Energy detection based cooperative spectrum sensing in cognitive radio networks", *IEEE Trans. on Wirel. Commun.*, vol. 10, no. 4, pp. 1232–1241, 2011 (DOI: 10.1109/TWC.2011.012411.100611).
- [22] G. Mahendru, A. Shukla, and P. Banerjee, "A novel mathematical model for energy detection based spectrum sensing in cognitive radio networks", *Wirel. Pers. Commun.*, vol. 110, no. 3, pp. 1237–1249, 2020 (DOI: 10.1007/s11277-019-06783-3).
- [23] F. F. Digham, M.-S. Alouini, and M. K. Simon, "On the energy detection of unknown signals over fading channels", *IEEE Trans. on Commun.*, vol. 55, no. 1, pp. 21–24, 2007 (DOI: 10.1109/TCOMM.2006.887483).
- [24] I. S. Gradshteyn and I. M. Ryzhik, *Table of Integrals, Series, and Products*, 8th ed. Academic Press, 2014 (ISBN: 9780123849335).
- [25] A. Nuttall, "Some integrals involving the Q<sub>M</sub> function (Corresp.)", *IEEE Trans. on Inform. Theory*, vol. 21, no. 1, pp. 95–96, 1975 (DOI: 10.1109/TIT.1975.1055327).



**Samit Kumar Ghosh** received his B.Tech. degree in Electronics and Communication Engineering from Kalyani University, West Bengal, India, in 2002 and the M.Tech. degree in Electronics System and Communication Engineering from the National Institute of Technology (NIT) Rourkela, Rourkela, Odisha, India, in 2006. Currently, he is pursuing the Ph.D. degree in the department of Electrical and Electronics Engineering (EEE), Birla Institute of Technology and Science, Pilani, Hyderabad Campus, Hyderabad, India. His research interests include biomedical signal processing, medical devices and

instrumentation, non-stationary signal processing, machine learning, cognitive radio, spectrum sensing. He has published research papers in reputed international journals and conferences.

 <https://orcid.org/0000-0003-2267-7314>

E-mail:samitnitrkl@gmail.com

Department of Electrical and Electronics Engineering

Birla Institute of Technology and Science, Pilani  
Hyderabad Campus, Hyderabad-500078



**Sachin Ravikant Trankatwar** received his B.E. degree in Electronics and Telecommunications Engineering from IETE, New Delhi, in 2010, and a Master's degree from Electronics and Telecommunications Engineering Department, DBATU, Lonere, Raigad, India, in 2013. He is currently pursuing a Ph.D. degree from BITS Pilani, Hy-

derabad Campus, Hyderabad, India. He has over five years of teaching experience at an undergraduate level. His current research interest includes efficient techniques for 5G cellular networks.

 <https://orcid.org/0000-0001-5114-2058>


E-mail:strankatwar@gmail.com

Department of Electrical and Electronics Engineering  
Birla Institute of Technology and Science, Pilani  
Hyderabad Campus, Hyderabad-500078



**P. Bachan** received his B.Tech. from Dayalbagh Educational Institute, Agra, India in 2007, M.Tech. from National Institute of Technology, Kurukshetra, India in 2010. He is currently working as an Assistant Professor and also pursuing his Ph.D. in the Department of Electronics and Communication Engineering, GLA University,

Mathura, India. His research interest includes spectrum sensing, multiple access techniques for next gen networks, channel estimation techniques and massive MIMO.

 <https://orcid.org/0000-0001-8188-5901>

E-mail:p.bachan@gmail.com

Department of Electronics and Communication Engineering  
GLA University, Mathura  
Mathura-281 406 (U.P.)

# FANET Drone's 4K Data Applications, Mobility Models and Wi-Fi IEEE802.11n Standards

Ghassan A. QasMarrogy

College of Engineering, Department of Communication and Computer Engineering,  
Cihan University-Erbil, Kurdistan Region, Iraq

<https://doi.org/10.26636/jtit.2021.148520>

**Abstract**—With growing popularity of unmanned aerial vehicles (UAVs), the importance of flying ad-hoc networks (FANETs) is enhanced by such applications as 4K video recording, communications in search and rescue missions and goods deliveries, to name just a few. This, in turn, stimulates research on different topologies of networks existing between UAVs, with studies in this field being essential to improving performance of such networks. Several problems must be solved to effectively use UAVs in order to offer stable and reliable massive data transmission capabilities, taking into consideration quickly changing FANET topologies, types of routing, security issues, etc. In this paper, a comprehensive evaluation of FANETs used by UAVs is presented in terms of communication network challenges, data types, mobility models and standards applied in order to achieve best performance. The evaluation presented herein covers such areas as data throughput, retransmission attempts and delay.

**Keywords**—4K data transmission, FANET, mobility models, UAV.

## 1. Introduction

A flying ad-hoc network (FANET) is a combination of fast-flying devices (drones) and infrastructure-less ad hoc networks [1]. Due to a high degree of mobility that quickly changes the topology of the network, different types of highly dynamic technologies for 4K video recording and environment sensing [2] are used, as shown in Fig. 1. In consideration of the above, FANETs operate in challenging environments and rely on powerful equipment to ensure operational multi-tasking capability. Unfortunately, drones are characterized by very limited resources in terms of hardware and power supply, limited wireless radio range, throughput, as well as payload capacity [3], [4].

IEEE 802.11 constitutes a component of the IEEE 802 set of local area network (LAN) protocols and is concerned with media access control (MAC) and physical layer (PHY) solutions relied up to implement wireless local area networks (WLANs) in various frequency bands, including, but not limited to 2.4, 5, 6 and 60 GHz bands [5]. In this paper, the 802.11n standard is analyzed as it is the latest protocol that supports both 2.4 GHz and 5 GHz frequencies [6].

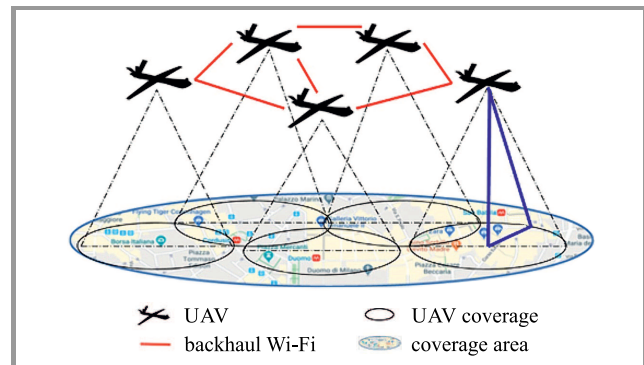


Fig. 1. FANET UAV communications scheme.

In this paper, an evaluation of FANET is presented, focusing on the communication network-related challenges, data types, mobility models and standards. The evaluation is concerned with throughput, retransmission attempts and delay requirements that need to be satisfied to achieve the best 4K video transmission parameters using FANET networks without any fixed infrastructure.

The paper is structured as follows. Section 2 presents the related work. Section 3 offers a brief description of the routing protocols, mobility models and IEEE 802.11n communication standards. Section 4 shows the results of the performance analysis. Finally, in Section 5, conclusions and the future work are presented.

## 2. Related Work

Many authors attempted to solve the most crucial problems affecting FANETs and tried to evaluate different types of technologies to ensure reliable data transmission and good performance.

In [7], a novel scheme was proposed in connection with the adaptive energy efficient hello-interval scheme (EE-Hello). It was based on best distance approximation that was harnessed to send hello messages and identified the number of UAVs required to achieve the task at hand. The proposed scheme saved up to 25% of energy needed. In [8],

a new course-aware opportunistic routing (CORF) protocol was proposed for FANETs to calculate the best neighbor position in order to transfer data efficiently. In comparison with other routing protocols, the proposed solutions offered a significant performance gain, with better message delivery rates and shorter delays.

In [9], an attempt was made to enhance in IEEE 802.11n 5 GHz video streaming in terms of throughput, retransmission attempts and delay. The results show an improvement that is achieved in video streaming by using WNIC parameters of the UAV. In [10], different mobility models were compared and evaluated, such as random waypoint mobility (RWPM), pursue mobility model (PRS), semi-random circular movement (SCRM), and Manhattan grid mobility model (MGM). The results show that MGM exerts the greatest impact on the delay and packet dropping ratios. Paper [11] focuses on data distribution service (DDS) middleware and presents a logic analysis and an evaluation of competing DDS implementations, and thus could serve well as input for deciding which of these solutions is best suited for a given situation, with a practical performance evaluation performed based on several different scenarios to effectively compare the most frequent DDS implementations. The results show that higher delays are obtained when higher memory requirements are present.

### 3. FANET Parameters

There are different types of routing protocols that have been used and evaluated for FANET, but because of the 3D nature of UAVs, it is very difficult to test all these routing protocols simultaneously, under different mobility models and IEEE standards. In [12], the authors classified FANET routing protocols into different categories, such as proactive, reactive, and hybrid protocols (Fig. 2) [12]. Based on this taxonomy, in this paper, two main routing protocols were chosen as best suited for FANET: ad-hoc on-demand vector (AODV) and optimized link state routing protocol (OLSR).

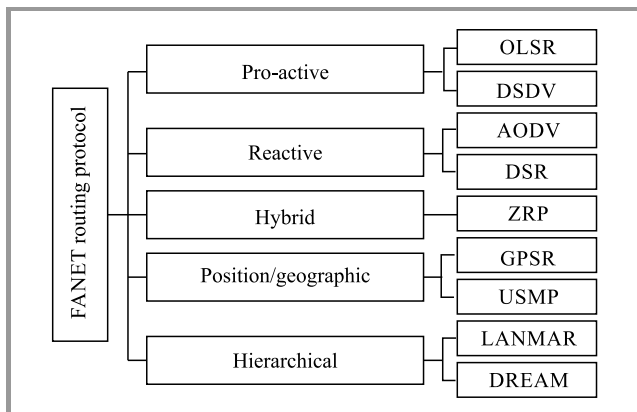


Fig. 2. FANET routing protocol.

Being a reactive type protocol, ad-hoc on-demand distance vector (AODV) uses sequence numbers and the broadcast

discovery mechanism to calculate the best recent fresh route to the final node. The discovery phase starts when a node needs to transmit data packets to the destination node while recording all recent fresh routes in the node routing table until the transmission ends. Thereafter, the main routes will be deleted and the next phase of the path discovery process will commence when another transmission starts. This protocol causes more delay but has lower overhead during the transmission compared to other routing protocols [13].

The proactive optimized link state routing (OLSR) protocol uses multipoint relays (MPR), i.e. groups of selected devices, to exchange their recent information about fresh routes between the nodes, with such an approach offering shorter delays in the route discovery phase. The hello messages are broadcast between neighbor nodes, and the fresh routes are stored at frequent intervals, continuously, without any requests from other nodes. This protocol allows to shorten the delays. Its drawback consists in a higher overhead caused by large amounts of data transmitted to make the routes available all the time [13].

#### 3.1. FANET Mobility Models

Due to the high degree of object mobility in FANETs, data may be dropped, delayed and not received at all [14]. Therefore, it is very important to evaluate the performance of a FANET network based on real-life scenarios. Many researchers use the random waypoint model (RWPM) to analyze and simulate FANET performance. Unfortunately, this model forces all UAVs to fly in random directions, which affects communication links between the nodes and degrades data transmission performance.

In this paper, three types of real mobility models are used and analyzed: RWPM, pathway mobility model (PMM) and semi-random circular movement (SRCM), as shown in Table 1 [14].

Table 1  
Realistic mobility model scenarios

Mobility model	Scenarios	Realistic scenario description
RWPM	Search and rescue	A random search of target zones. Random area scanning.
PPM	Object tracking	Surveillance of city roads. Surveillance over a crash location until rescue services arrive
SRCM	Surveying, patrolling and object tracking	Surveillance of an object

The RWPM model uses different timing for UAV hover and movement scenarios. It calculates the direction and the speed of UAVs based on random values. When the transmission starts, the UAV waits, hovering, for a specific period of time, and then it starts moving to a preselected position at a random speed chosen from range uniformly prescribed for the entire simulation process. This procedure is repeated until the simulation is finished. Due to random variations in speed and directions, this approach corresponds to real-life scenarios, such as search and rescue missions or wireless sensor networks covering extensive areas [15].

The SRCM model uses hexagon shaped routes instead of random tracks with a specified speed value. The UAV is moving within area defined with a specified hexagon. This model may be used in real life conditions for surveying, patrolling and target tracking [16].

The PMM model uses a straight route preference. It specifies the first and the last point between which the UAV moves at a fixed speed. After reaching the last point a new destination will be selected with a new speed and direction, and this procedure will be repeated until the simulation is finished. Such a model is suitable for target tracking, thermal monitoring, as well as for video recording and transmission [17].

Incorporating IEEE 802.11n-based Wi-Fi connectivity relying on 2.4 GHz and 5 GHz bands may decrease interference and delays while simultaneously increasing the speed of data transmission, as shown in Fig. 3 [18].

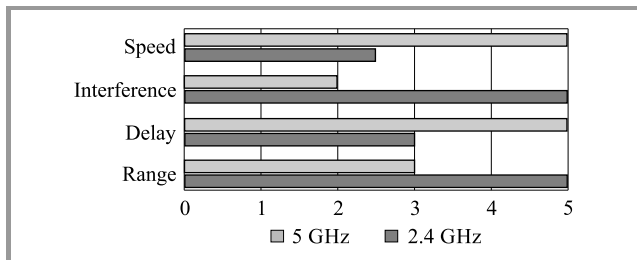


Fig. 3. Dual band IEEE 802.11n feature comparison.

The 5 GHz band offers higher speeds, and is therefore capable of improving performance and throughput of FANETs. The 5 GHz band also supports a higher number of network connections and communication channels than its 2.4 GHz counterpart – a property that is essential for providing 4K video streaming [19]. The shorter range of 5 GHz may be enhanced significantly by increasing the size of the directional antenna [20].

### 4. Simulations and Results

Three routing protocols were analyzed using the NS3 simulator. Three realistic mobility models and two types of IEEE 802.11n standards have been taken into consideration to evaluate such metrics as throughput, delay and retransmission attempts.

4K video streaming was chosen to simulate high data traffic rates.

A 60-second 4K video stream (3840 × 2160) at 30 fps and with 24 bit color means that 427 MB of data need to be transmitted. Other simulation parameters are summarized in Table 2.

Table 2  
Simulation environment parameters

Parameters	Values
Area size	1500 × 1500 m
Number of nodes	40 UAVs
Routing protocols used	AODV, OLSR
Traffic type	4K video streaming
Mobility models	RWPM, PMM, SRCM
Node speed, altitude	20 m/s, 20 m
Simulation time	600 s
IEEE 802.11n standards	2.4, 5 GHz

Figure 4 shows the throughput of FANET for IEEE 802.11n in 2.4 and 5 GHz bands. AODV offers better results in 5 GHz than in 2.4 GHz, while OLSR maintains the same performance, because AODV needs more bandwidth to keep its fresh routes updated and to broadcast control packets all the time. 4K video streaming requires more bandwidth to support large packet transmissions.

The activity of SRCM is limited or non-existent due to the rounded movement of UAVs, resulting in high distances between them (and the range of 5 GHz is shorter than in the case of 2.4 GHz). PMM turns out to be the best mobility model for all types of transmissions and standards. This is because PMM is capable of establishing a direct communication path and of maintaining fresh routes for longer periods than in the case of RWPM.

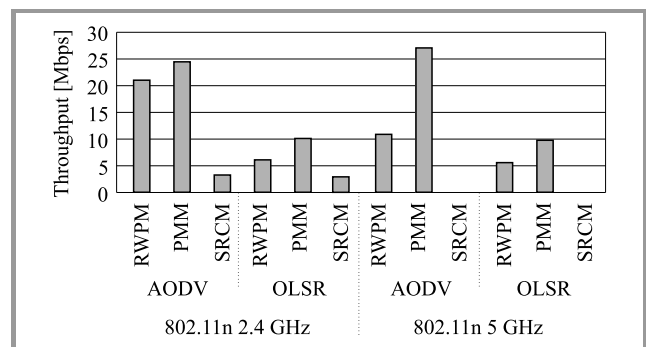


Fig. 4. Data throughput for IEEE 802.11n, mobility models, and routing protocols.

Simulation results shown in Fig. 5 confirm that delays experienced in FANETs are higher when using 2.4 GHz, as 5 GHz relies on higher bandwidth. The results achieved with the use of the PMM mobility model are better in all

scenarios, as it continuously establishes a direct path to the packets. OLSR results remain the same, as in this approach fresh routes are broadcast regularly by control packets.

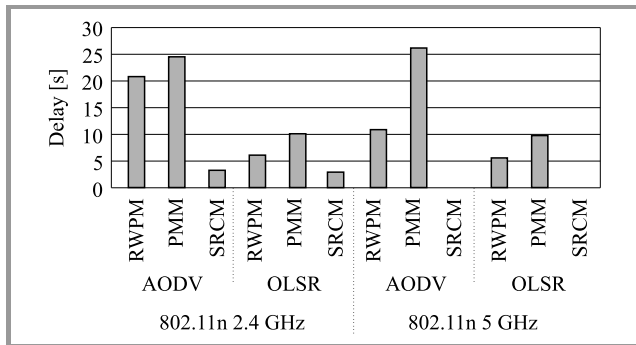


Fig. 5. Delay for both versions of IEEE 802.11n, mobility models, and routing protocols.

The simulation results presented in Fig. 6 show that the number of retransmission attempts undertaken by FANET is higher for 5 GHz, as the range of this band is shorter, which may result in a greater number of route breaks that increase the number of retransmission attempts. AODV renders also better results than OLSR in 5 GHz for the PMM mobility model, resulting in a breakthrough discovery that AODV outperforms OLSR. Better results obtained in 5 GHz may be solved easily by changing the mobility model to a more preferable scenario that makes all UAVs move closer to each other in order to decrease delay and increase network transmission throughput.

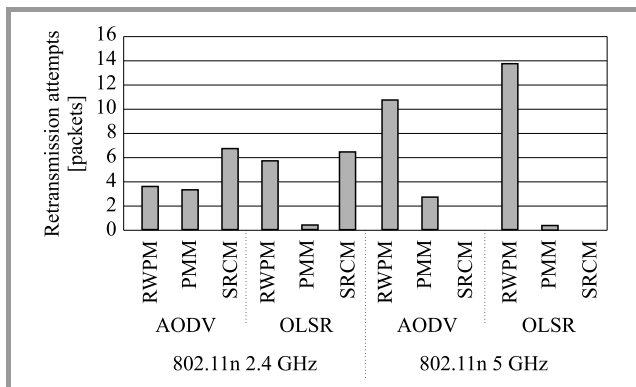


Fig. 6. Retransmission attempts for IEEE 802.11n, mobility models, and routing protocols.

## 5. Conclusion

Simulation results indicate the throughput increases when 5 GHz is used along with PMM mobility models and AODV, while OLSR remains stable in all tested scenarios. AODV is also capable of rendering better performance with shorter delays, as it utilizes the entire capacity of the bandwidth, while 5 GHz suffers from more route breakages during transmission, as its range is shorter than that of the 2.4 GHz band.

## References

- [1] G. A. Qasmarrogy and Y. S. Almashhadani, "Ad hoc on-demand distance vector inherent techniques comparison for detecting and eliminating the black hole attack nodes in mobile ad hoc network", *Cihan University-Erbil Scientific J.*, vol. 4, no. 1, pp. 77–81, 2020 (DOI: 10.24086/issn.2519-6979).
- [2] H. J. Alqaysi and G. A. QasMarrogy, "Performance analysis of video streaming application over MANETs routing protocols", *Int. J. of Research In Comput. Applications And Robotics*, vol. 3, no. 7, pp. 22–28, 2015 [Online]. Available: [https://www.ijrcar.com/Volume\\_3\\_Issue\\_7/v3i707.pdf](https://www.ijrcar.com/Volume_3_Issue_7/v3i707.pdf)
- [3] Z. Zheng, A. K. Sangaiah, and T. Wang, "Adaptive communication protocols in flying ad hoc network", *IEEE Commun. Mag.*, vol. 56, no. 1, pp. 136–142, 2018 (DOI: 10.1109/MCOM.2017.1700323).
- [4] M. A. Khan, A. Safi, I. M. Qureshi, and I. U. Khan, "Flying ad-hoc networks (FANETs): A review of communication architectures, and routing protocols", in *Proc. 2017 First Int. Conf. on Latest trends in Electrical Engin. and Comput. Technol. INTELLECT IEEE*, Karachi, Pakistan, 2017, pp. 1–9 (DOI: 10.1109/INTELLECT.2017.8277614).
- [5] C. Deng *et al.*, "IEEE 802.11be Wi-Fi 7: New Challenges and Opportunities", in *IEEE Commun. Surveys & Tutorials*, vol. 22, no. 4, 2020, pp. 2136–2166 (DOI: 10.1109/COMST.2020.3012715).
- [6] R. Karmakar, S. Chattopadhyay, and S. Chakraborty, "Impact of IEEE 802.11n/ac PHY/MAC high throughput enhancements on transport and application protocols – A survey", in *IEEE Commun. Surveys & Tutorials*, vol. 19, no. 4, 2017, pp. 2050–2091 (DOI: 10.1109/COMST.2017.2745052).
- [7] I. Mahmud and Y. Z. Cho, "Adaptive hello interval in FANET routing protocols for green UAVs", *IEEE Access*, vol. 7, pp. 63004–63015, 2019 (DOI: 10.1109/ACCESS.2019.2917075).
- [8] Y. He *et al.*, "A Course-aware opportunistic routing protocol for FANETs", *IEEE Access*, vol. 17, pp. 144303–144312, 2019 (DOI: 10.1109/ACCESS.2019.2944867).
- [9] G. A. Q. Marrogy, "Enhancing video streaming transmission in 5 GHz FANET drones parameter", *Telecommun. and Radio Engin.*, vol. 79, no. 11, pp. 997–1007, 2020 (DOI: 10.1615/TelecomRadEng.v79.i11.90).
- [10] A. AlKhatieb, E. Felemban, and A. Naseer, "Performance evaluation of ad-hoc routing protocols in (FANETs)", in *IEEE Wireless Commun. and Networking Conf. Workshops WCNW*, Seoul, South Korea, 2020, pp. 1–6 (DOI: 10.1109/WCNW48565.2020.9124761).
- [11] R. Fujdiak *et al.*, "Security and performance trade-offs for data distribution service in flying ad-hoc networks", in *11th Int. Congress on Ultra Modern Telecommun. and Control Systems and Workshops ICUMT*, Dublin, Ireland, 2019, pp. 1–5 (DOI: 10.1109/ICUMT48472.2019.8970670).
- [12] G. A. QasMarrogy, H. J. Alqaysi, and Y. S. Almashhadani, "Comprehensive study of hierarchical routing protocols in MANET using simple clustering", *Cihan University-Erbil Scientific J.*, pp. 142–150, 2017 (DOI: 10.24086/cuesj.si.2017.n1a12).
- [13] G. A. Marrogy, "Performance analysis of routing protocols and TCP variants under HTTP and FTP traffic in MANET's", M.Sc. Thesis, Eastern Mediterranean University (EMU)–Dogu Akdeniz Üniversitesi (DAÜ), 2013.
- [14] A. Chriki, H. Touati, H. Snoussi, and F. Kamoun, "FANET: communication, mobility models and security issues", *Computer Networks*, vol. 163, no. 9, 2019 (DOI: 10.1016/j.comnet.2019.106877).
- [15] P. K. Sharma and D. I. Kim, "Random 3D mobile UAV networks: mobility modeling and coverage probability", *IEEE Transactions on Wireless Communications*, vol. 18, no. 5, pp. 2527–2538, 2019 (DOI: 10.1109/TWC.2019.2904564).
- [16] A. Adya, K. P. Sharma, Nonita, "Energy aware clustering based mobility model for FANETs", in *Proc. of ICETIT*, P. Singh, B. Panigrahi, N. Suryadevara, S. Sharma, and A. Singh, Eds. Cham: Springer, vol. 605, 2019, pp. 36–47 (DOI: 10.1007/978-3-030-30577-2\_3).



- [17] W. Wang, J. Wang, M. Wang, B. Wang, and W. Zhang, "A realistic mobility model with irregular obstacle constraints for mobile ad hoc networks", *Wireless Networks*, vol. 25, pp. 487–506, 2019 (DOI: 10.1007/s11276-017-1569-z).
- [18] I. Dolińska, M. Jakubowski, and A. Masiukiewicz, "Interference comparison in Wi-Fi 2.4 GHz and 5 GHz bands", in *Proc. Int. Conf. on Information and Digital Technol. IDT*, Zilina, Slovakia, 2017, pp. 106–112 (DOI: 10.1109/DT.2017.8024280).
- [19] A. Qaddus, "An evaluation of 2.4 GHz and 5 GHz ISM radio bands utilization in backhaul IP microwave wireless networks", in *Proc. Int. Conf. on Information Science and Communications Technol. ICISCT*, Tashkent, Uzbekistan, 2019, pp. 1–5, (DOI: 10.1109/ICISCT47635.2019.9011923).
- [20] T. A. T. Aziz, M. R. Abd Razak, and N. E. A. Ghani, "The performance of different IEEE802.11 security protocol standard on 2.4 GHz and 5 GHz WLAN networks", in *Proc. Int. Conf. on Engineering Technol. and Technopreneurship ICE2T*, Kuala Lumpur, 2017, pp. 1–7 (DOI: 10.1109/ICE2T.2017.8215954).
- [21] X. Li, M. A. Salehi, M. Bayoumi, and R. Buyya, "CVSS: a cost-efficient and QoS-aware video streaming using cloud services", in *Proc. 16th IEEE/ACM Int. Symp. on Cluster, Cloud and Grid Comput. CCGrid*, Cartagena, 2016, pp. 106–115 (DOI: 10.1109/CCGrid.2016.49).



**Ghassan A. QasMarrogy** received his B.Sc. Degree in Computer and Communication Engineering in 2009, and M.Sc. Degree in Electrical and Electronic Engineering from Eastern Mediterranean University in 2013. He is currently working as a lecturer at the Department of Computer and Communication Engineering. His re-

search interests include data and multimedia communication, wireless and ad-hoc networks, MANET and FANET networks, as well as security and cybersecurity in communication.

E-mail: Ghassan.qasmarrogy@cihanuniversity.edu.iq

College of Engineering

Department of Communication and Computer Engineering

Cihan University-Erbil

Kurdistan Region, Iraq

# Artificial Magnetic Conductor-based Millimeter Wave Microstrip Patch Antenna for Gain Enhancement

Khadidja Belabbas, Djamel Khedrouche, and Abdesselam Hocini

*Laboratoire d'Analyse des Signaux et Systèmes, Department of Electronics,  
Mohamed Boudiaf University of M'sila, BP. 166, Route Ichebilia, M'sila, 28000 Algeria*

<https://doi.org/10.26636/jtit.2021.148320>

**Abstract**—In this paper, a small ( $20 \times 20 \times 2.4$  mm) loaded microstrip patch antenna (MPA) with an asymmetric artificial magnetic conductor (AMC) as a ground plane is designed for millimeter wave applications. Two AMC structures are proposed; one has the property of a  $0^\circ$  reflection phase around 28.4 GHz, with a symmetric geometry, which makes the reflection phase insensitive to variations in both polarization and incident angle. This symmetric AMC structure ensures angular stability which is considered as a major requirement when periodic structures are used as antenna ground planes. The other structure is characterized by an asymmetric geometry and shows an interesting behavior around 28.6 GHz, where a discontinuity in the reflection phase appeared due to the fact that surface impedance nature changed from purely capacitive to purely inductive. This paper studies the effects of the two proposed AMC structures on the performance of MPAs, by using an array of  $8 \times 8$  unit cell elements as an artificial ground plane. Simulation results show that an MPA with a symmetric AMC ground plane offers better impedance matching and a wider bandwidth. Compared with conventional MPAs, gain is enhanced and directivity is improved as well. As far as an MPA with an asymmetric AMC ground plane is concerned, its performance in terms of gain and directivity is higher than that of the conventional solution.

**Keywords**—artificial magnetic conductor, gain enhancement, microstrip patch antenna, millimeter wave, reflection phase.

## 1. Introduction

Millimeter wave frequency bands are receiving much attention today in modern wireless communication systems [1], such as 5G. This part of spectrum covers frequencies from 30 to 300 GHz, which corresponds to wavelengths from 1 to 10 mm. The use of this band for the design of a data transmission system offers a number of advantages, for example high throughput and ability of designing a radio link with high directivity [2]. However, communications at frequencies of approximately 60 GHz suffer from high propagation losses due to RF energy absorption by oxygen in the atmosphere [3].

The microstrip patch antenna has been an attractive choice in mobile and wireless communication, because of its low profile, compact design, low cost, easy fabrication and integration with devices. Microstrip patch antennas are also a crucial part of MIMO array aerial systems [4], [5] widely used in 5G communication applications. Due to such disadvantages as narrow bandwidth, low efficiency and surface wave losses, improved types with big, periodic structures operating at microwave or millimeter wave resonance frequencies are commonly used. These structures are called electromagnetic band-gap (EBG) i.e. are a class of periodic dielectric, metallic, or composite materials that when introduced to an electromagnetic wave, offer a great performance improvement.

A mushroom type EBG has the propriety of a high impedance surface (HIS) and is characterized by in-phase reflections at the resonance frequency [4]–[6]. A uniplanar EBG is a periodic structure with the property of in-phase reflections, just as in the case of the mushroom type EBG, but with no via connection to the ground plane. The absence of via makes its integration with millimeter and microwave circuits easier [7]. The in-phase reflection could be achieved by using the perfect magnetic conductor (PMC) which does not exist in nature. Hopefully, similar characteristics may be achieved by an artificial magnetic conductor (AMC) which is a solution allowing to overcome numerous disadvantages of microstrip antennas operating within the microwave range. It is used as the ground plane to enhance radiation performance, such as uni-directional radiation patterns and the antenna's peak gain [8]–[12]. When the AMC is printed in the same plane as the microstrip antenna, it improves its scattering performance by reducing the radar cross section [13]–[16]. This technique is often used for developing high isolated MIMO antennas [17]. The AMC is also used as a ground plane in textile-based antennas for wearables [18]–[20], in order to suppress back radiation. In [21], a planar circular cross AMC-based ultra-wideband (UWB) antenna is used to enhance the radiation pattern and

gain. The microstrip patch antenna based on an asymmetric AMC ground plane is also studied in [22], where it is used as a reflection plane to achieve both good bandwidth and a low level of cross-polarization.

In this paper, a simple miniature design of AMC unit cells resonating in the millimeter wave band is presented. The presented unit cell and antenna designs are very simple, making them easy to fabricate and integrate in millimeter wave applications. The presented design has a wide bandwidth, which makes this aerial suitable for broadband millimeter wave antenna applications, and by using an  $8 \times 8$  array of unit cells underneath of the conventional microstrip antenna, gain and the directivity are clearly improved as well.

The paper is organized as follows. First, the design and the characteristics of the proposed symmetric and asymmetric AMC are presented in Section 2, where we also analyze their reflection phase and surface impedance properties. In Section 3, the performance of the antenna over an asymmetric AMC ground plane is studied and compared with an MPA with a symmetric AMC ground plane, and with a conventional MPA. Finally, conclusions are presented in Section 4.

## 2. Proposed Asymmetric AMC Design

The AMC material is characterized by two important properties, namely high impedance for transverse electric (TE) and transverse magnetic (TM) wave polarization, and for all propagation directions. Its other peculiar property is the fact that it reflects the impinging waves with a zero-phase shift. It is called AMC, because its tangential magnetic field is zero at the surface.

To study these properties further, we designed a 2D planer asymmetric AMC unit cell. According to [4], the lumped element model describes the AMC structure as an LC resonant circuit. Inductance  $L$  and capacitance  $C$  are determined by the unit cell geometry and its resonance behavior is used to explain the properties of AMC, such as surface impedance and reflection phase, which are defined as [23]:

$$Z_s = \frac{j\omega L}{1 - \omega^2 LC}, \quad (1)$$

$$\omega_0 = \frac{1}{\sqrt{LC}}, \quad (2)$$

$$\text{Phase} = \text{Im} \left[ \ln \frac{Z_s - \eta}{Z_s + \eta} \right], \quad (3)$$

where  $Z_s$  is the impedance surface,  $\omega$  is the angular frequency, and  $\eta$  is the impedance of free space.

The geometry of the asymmetric unit cell consists of a square patch with two slots with the same width  $w = 0.1$  mm. The slotted patch is placed above a ground FR4 epoxy substrate with dielectric constant  $\epsilon_r = 4.4$  and

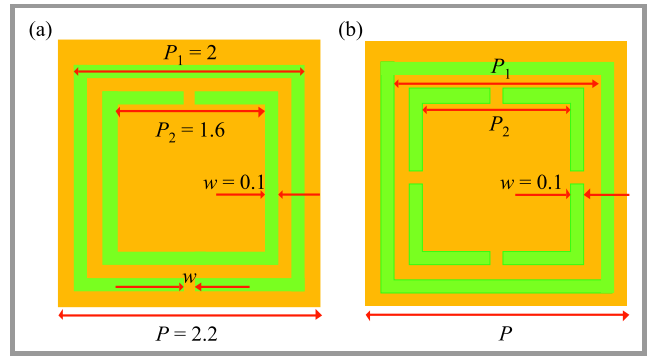


Fig. 1. Top view of the unit cell: (a) asymmetric and (b) symmetric designs.

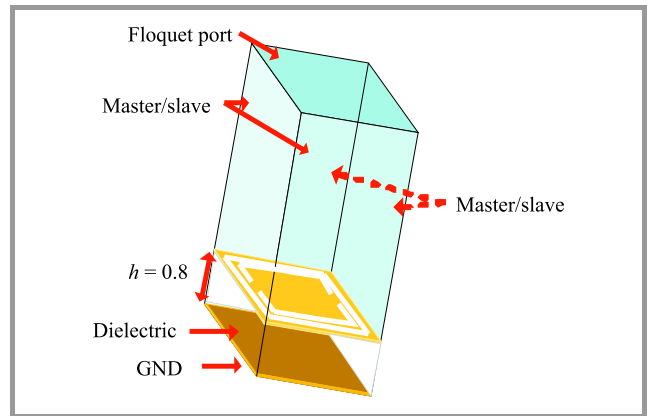


Fig. 2. Simulation model of the unit cell.

$h = 0.8$  mm. The period of the unit cell is  $p$  and the remaining dimensions (in mm) are shown in Fig. 1a. HFSS software was used to simulate the characteristics of the unit cell. Figure 2 shows the unit cell simulation, the master/slave boundaries are defined on the side walls of the air box, and the Floquet port is located on its top face to model an infinite periodic structure. The Floquet port allows to conduct research on the incident plane wave for different incident and polarizations angles.

### 2.1. Reflection Magnitude

Figure 3 shows the magnitude of the reflection coefficient when the polarization angle of the incident wave  $\varphi = 0$  and for different values of incident angle  $\theta$ . Figure 3a shows that the asymmetric AMC structure is fully reflective at two resonance frequencies: 25.41–25.62 GHz and 36.34–37.92 GHz. A slight variation in the resonant frequencies is observed for different  $\theta$  angles, which means that the asymmetric structure is insensitive to variations in the incident oblique angle. We observe also an attenuation in the reflection magnitude at the resonance points. For the lowest resonance frequency, attenuation reaches  $-12.88$  dB and  $-4.09$  dB for the highest resonances at  $\theta = 60^\circ$ .

As far as the symmetric AMC structure is concerned, there is only one resonance frequency and when the incident angle increases, the resonance frequency also increases slightly from 28.6 GHz for normal incidence to 29.1 GHz

for  $\theta = 60^\circ$  as shown in Fig. 3b. The attenuation in the reflection magnitude is observed and reaches  $-3.61$  dB for  $\theta = 60^\circ$ , which is less than for the asymmetric AMC. The magnitude of the reflection coefficient for a TM polarized wave is plotted in Fig. 4 for different  $\theta$  values. There are two resonance frequencies for an asymmetric AMC structure, and one for the symmetric version. The resonance point slightly varies with changes in  $\theta$ . The lowest resonance points are 19.6, 18.24, and 19.13 GHz, and the highest ones are 36.33 GHz, 36.88 GHz, and 36.64 GHz for  $0^\circ$ ,  $30^\circ$ , and  $60^\circ$ , respectively. Note that unlike for the symmetrical AMC structure, the resonance frequencies for TE polarized waves are not identical with those for TM polarized waves, due to the asymmetric geometry of the proposed unit cell. For the sake of clarity, we have only plotted the reflection magnitude of the proposed asymmetric AMC unit cell for  $\varphi = 0^\circ$ , because the results for  $90^\circ$  of the TE polarized wave are equivalent to those of the TM polarized angle for  $0^\circ$ .

**2.2. Reflection Phase**

Here, the reflection phase of the proposed AMC structure for the two polarization states of the impinging plane wave is presented. Figure 5 shows the TE polarization wave and, according to the criterion of the reflection phase being within the range of  $-90^\circ$  to  $+90^\circ$ , two bands shown in the asymmetric AMC structure. The first is centered on 25.4 GHz, and the other on 37.9 GHz unlike in the symmetric geometry, where one band appears around 28 GHz. As shown for both AMC structures, the phase changes are insignificant, which means that the proposed structure is not sensitive to oblique incident angle variations. The phase discontinuity for the asymmetric AMC is observed between low- and high-resonance frequencies, which is the most interesting behavior and the main difference between the two studied geometries.

In the case of a TM polarized incident wave, the reflection phase shows the same pattern but both lower and higher resonant frequency points move toward the lower frequency band, as shown in Fig. 6a, with the first band being around 19.6 GHz, and the other around 36.3 GHz. The point of discontinuity is also shifted downward and centered on 25 GHz. One may notice that the phase reflection of the asymmetric AMC is insensitive to the incident oblique angle. The same behavior is observed for symmetric AMC structures, as illustrated in Fig. 6b.

When comparing TE and TM polarized incident waves, one may notice that the reflection phase of the asymmetric AMC structure does not exhibit the same behavior for TE and TM. For the symmetric AMC structure, the center of the operating band is the same and the bandwidth becomes wider than that for TE.

**2.3. Impedance Surface of the Unit Cell**

The impedance surface versus frequency and the behavior of impedance around frequencies where the disconti-

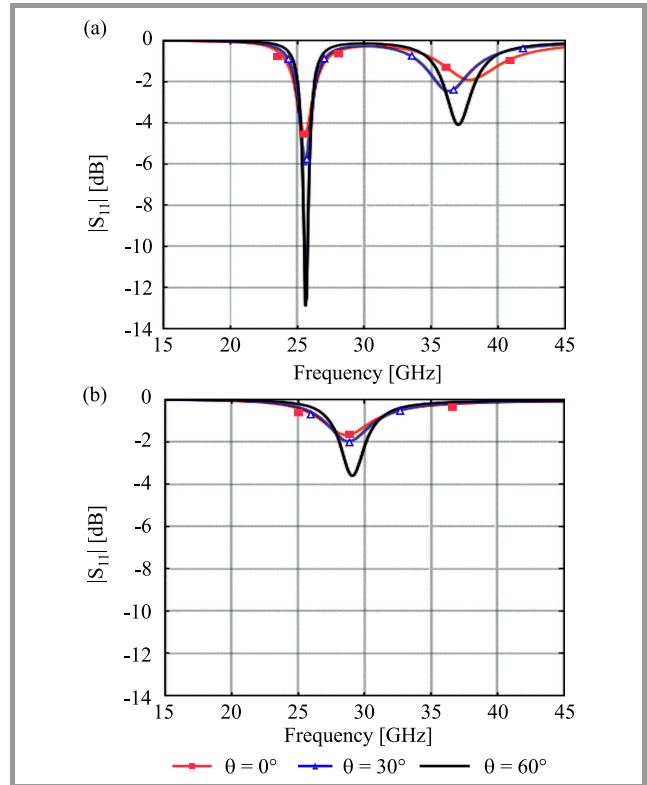


**Fig. 3.** Reflection magnitude for TE polarization wave, three oblique incident angles and polarization angle  $\varphi = 0^\circ$ : (a) asymmetric AMC and (b) symmetric AMC.

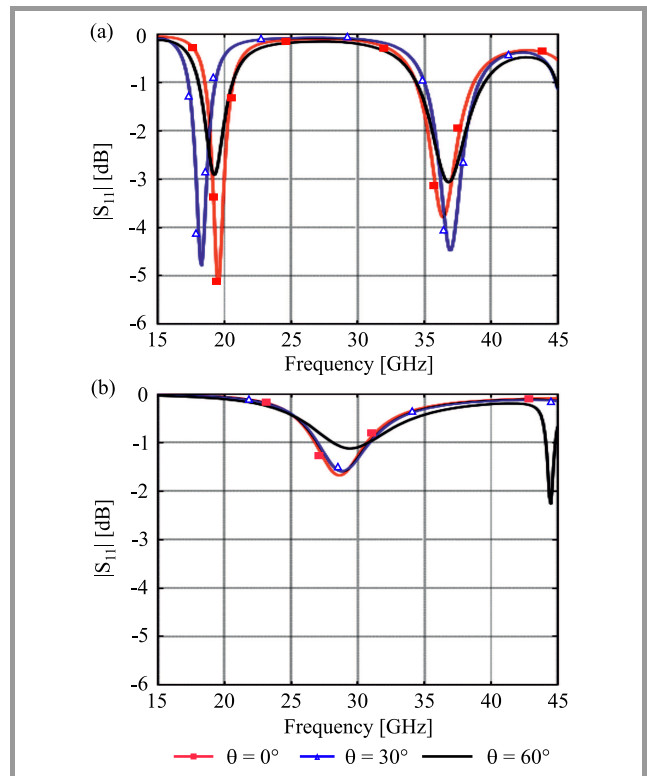


**Fig. 4.** Reflection magnitude for a TM polarization wave for different oblique incident angles and polarization angle  $\varphi = 0^\circ$ : (a) asymmetric AMC and (b) symmetric AMC.

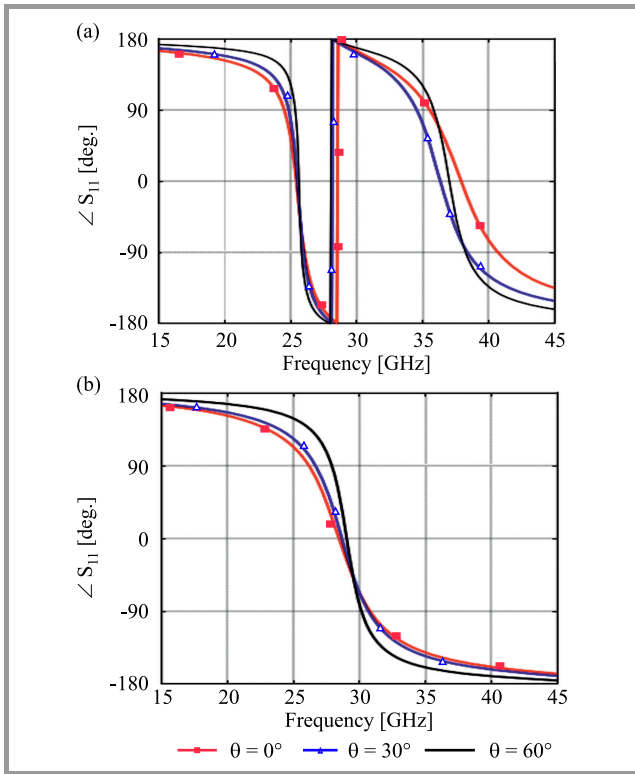


**Fig. 5.** Reflection phase for a TE polarization wave for different oblique incident angles: (a) asymmetric AMC and (b) symmetric AMC.

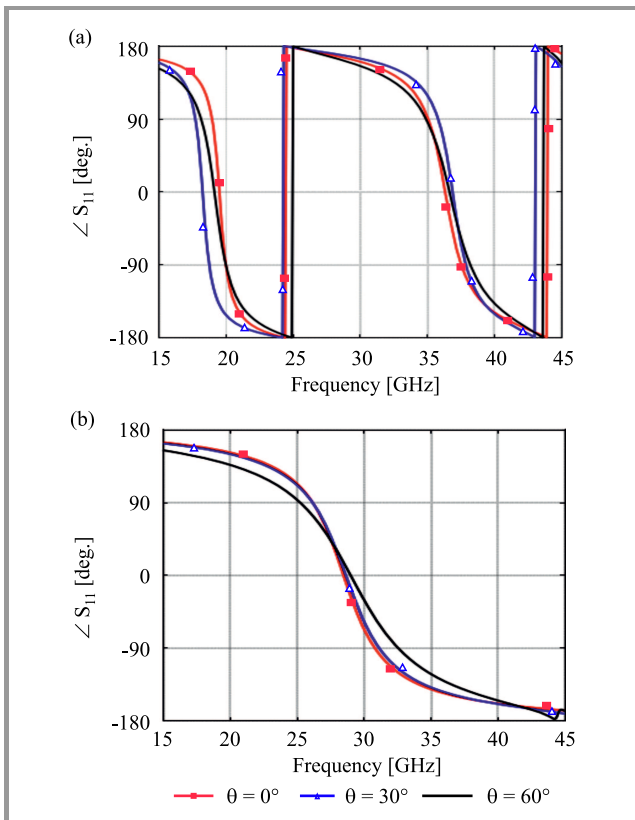


**Fig. 6.** Reflection phase for a TM polarization wave for different oblique incident angles: (a) asymmetric AMC and (b) symmetric AMC.

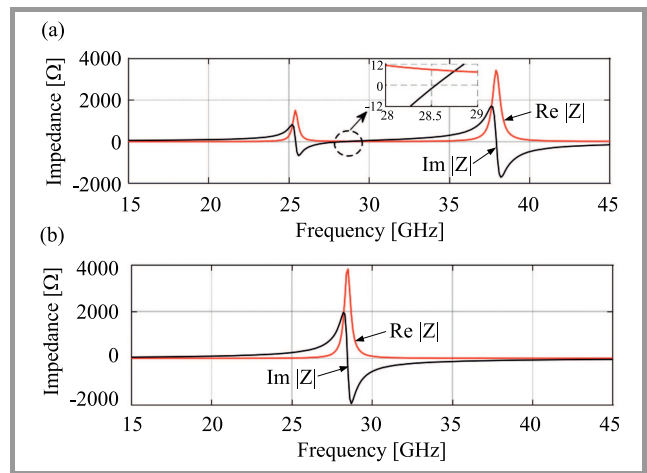


**Fig. 7.** Impedance of the proposed AMC unit cell for normal incidence and for a TE polarized wave: (a) asymmetric AMC and (b) symmetric AMC.

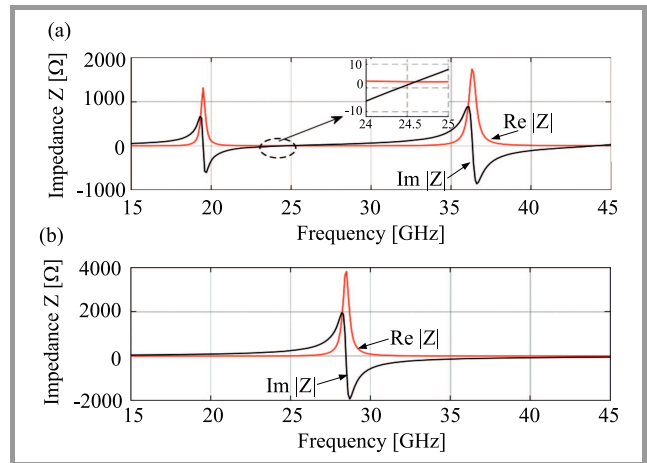


**Fig. 8.** Impedance surface of the proposed AMC unit cell for normal incidence and for a TM polarized wave: (a) asymmetric AMC and (b) symmetric AMC types.

unity of the phase has occurred are shown in Figs. 7–8 both two polarizations. High impedance is observed around 25.4 GHz and 37.9 GHz for the TE polarized wave, and around 19.5 GHz and 36.3 GHz for the TM polarized wave.

These values are identical with the frequencies obtained for the in-phase reflection phase  $\theta = 0^\circ$ . At the discontinuity point observed in the phase, the nature of impedance changes from capacitive to inductive, which leads to phase discontinuity. For clarity, a zoomed view around this point of impedance is inserted in Figs. 7 and 8. As we can see, around 28.54, and 24.45 GHz, impedance type changes from capacitive to inductive, for a TE polarized wave and a TM polarized wave, respectively. For the symmetric AMC, the results are in agreement with the reflection phase in terms of resonance frequency points and bandwidth. All resonance points at the  $0^\circ$  reflection phase are corresponding to those for the maximum value of the real part of impedance.



### 3. Results and Discussion

The geometry of a conventional microstrip patch antenna with and without the proposed AMC ground plane is shown in Fig. 9. A rectangular microstrip patch antenna of dimensions  $W_p \times L_p$ , excited by a 50  $\Omega$  microstrip line, is located on a 20  $\times$  20 mm FR4 epoxy substrate, with relative permittivity of  $\epsilon_r = 4.4$  and thickness of 1.6 mm. The same conventional MPA with no dimensional changes is placed directly above this new ground plane, as illustrated in Fig. 9c–d.

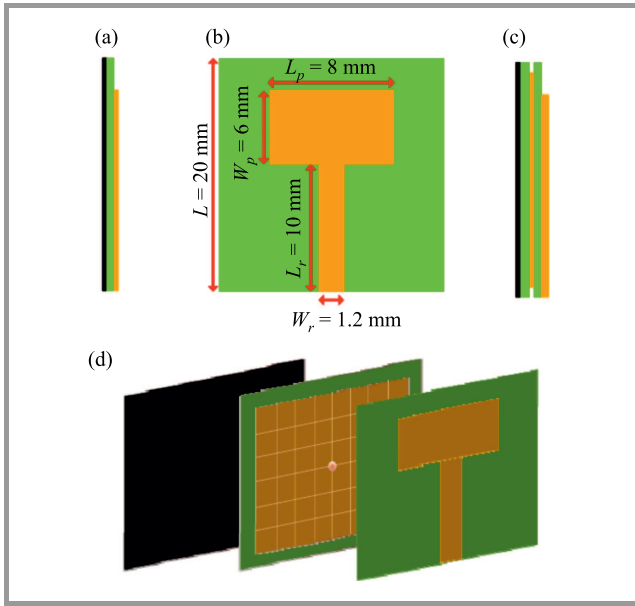


**Fig. 9.** Proposed microstrip patch antenna design: (a) side view without AMC, (b) front view without AMC, (c) side view with AMC, and (d) position of the dielectric layers.

The return loss of the proposed asymmetric AMC structure ground plane-based MPA is compared, in Fig. 10, with that of the conventional MPA and with that of an MPA based on the well-known symmetric AMC ground plane. The results show good impedance matching, with values of  $-46.6$  dB and  $-42$  dB being reached for antennas loaded by symmetric and asymmetric AMC ground planes, respectively. This

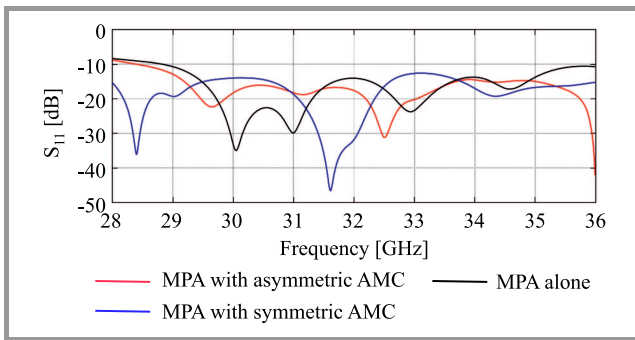


**Fig. 10.** Return loss for the proposed MPA-based on the AMC structure, compared with that for the conventional MPA and well-known AMC structure.

is due to the in-phase reflection between the image currents created by the radiator patch on the AMC ground plane. The lowest frequency is reduced to 28 GHz and to 28.4 GHz for the antenna loaded by symmetric and asymmetric AMC ground plane, respectively. This is due to the capacitance effect of the AMC structures. However, the higher frequency does not change, which leads to an enhancement in bandwidth. Thus, the antenna with the asymmetric ground plane has an impedance bandwidth of 23.75%, while the bandwidth for the antenna with the symmetric ground plane is 25%, and the bandwidth for the conventional aerial is 22.22%, for  $S_{11} < -10$  dB.

Gain is depicted, as a function of frequency, in Fig. 11. It reached the maximum around 31.4 GHz. This is near to the value where the phase of the asymmetric AMC structure shows discontinuity, and the nature of the impedance surface changes from capacitive to inductive, for a TE polarized wave. A considerable enhancement of gain is achieved, and the peak gain around this point reaches 8.6 dBi for the proposed asymmetric AMC ground plane-based MPA, where the gain of the conventional MPA is 2.8 dBi, which means an enhancement of 207.14%. The peak gain for the antenna with the symmetric AMC ground plane is 7 dBi at 31.4 GHz, and an enhancement of 148.2% is achieved. This value of frequency is almost the same as that of the symmetric AMC unit cell which has the property of a  $0^\circ$  reflection

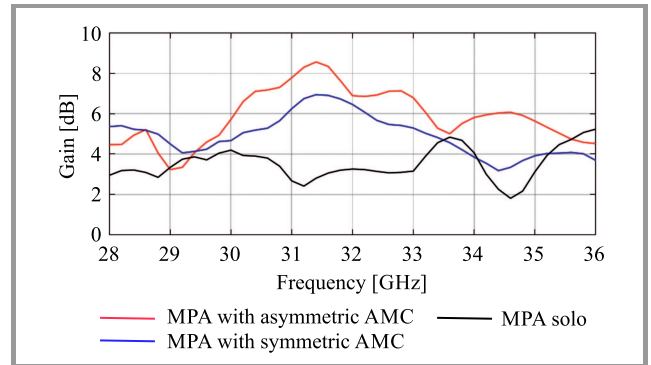


**Fig. 11.** The peak gain versus frequency for proposed MPA based on asymmetric AMC ground plane compared with that for the conventional MPA and well-known AMC.

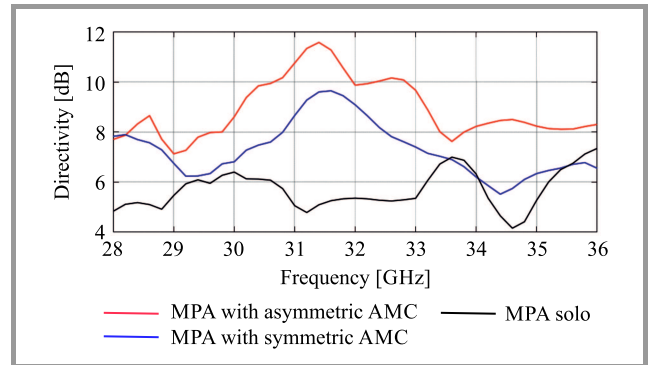


**Fig. 12.** Peak gain vs. frequency for the proposed MPA based on an asymmetric AMC ground plane compared with results for the conventional MPA and well-known AMC structure.



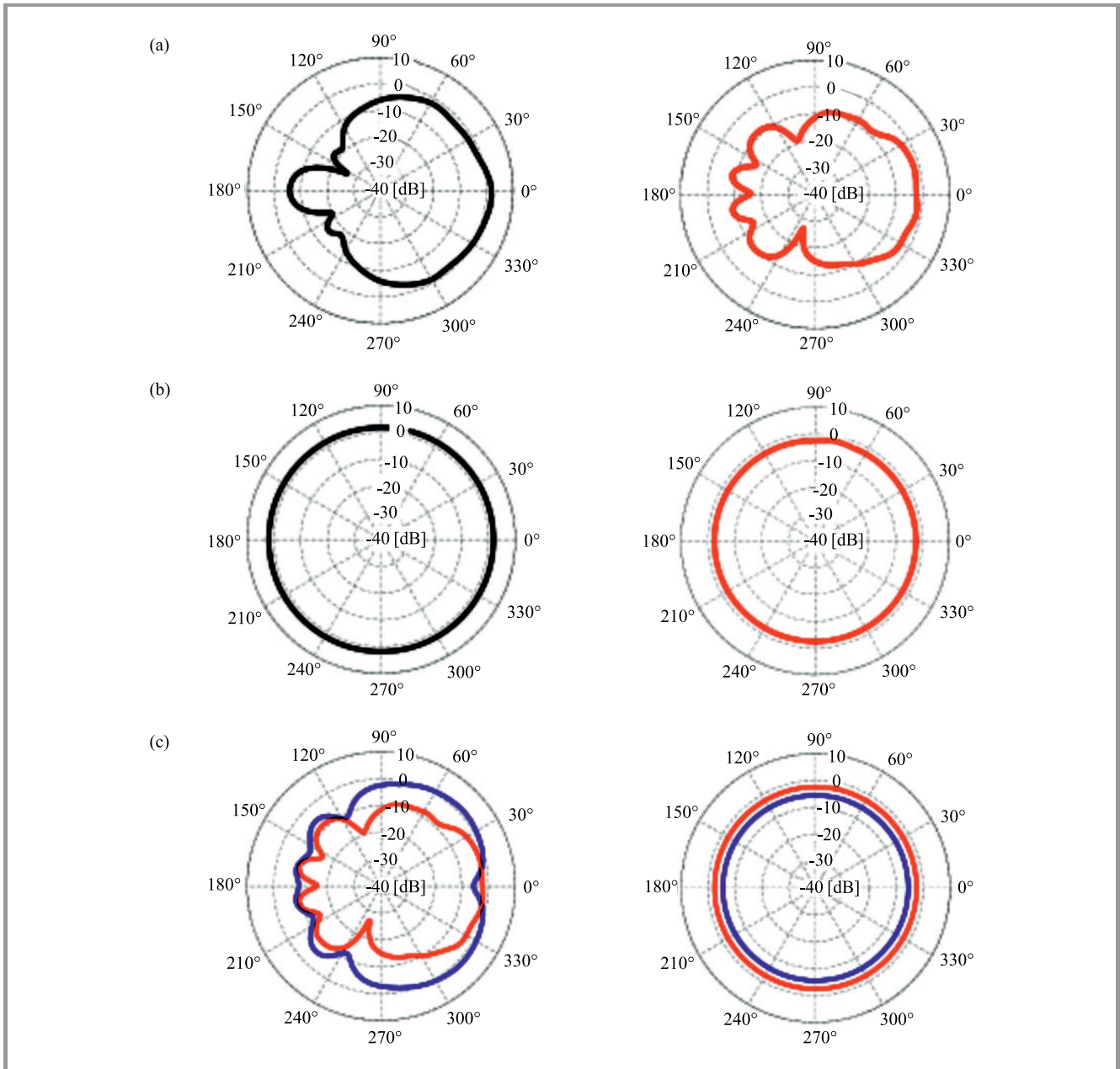


**Fig. 13.** Simulated radiation pattern for asymmetric type (red line), symmetric version (black line), and conventional antenna (blue line): (a) YOZ plane, (b) XOY plane, and (c) comparison between proposed asymmetric and conventional antennas (the left side is YOZ plane, and the right side is the XOY plane). (See digital version on <https://www.itl.waw.pl/en/publications/journal-jtit>)

**Table 1**  
Performance comparison of the proposed antenna based on an asymmetric AMC structure and similar designs from recent works

Antenna	Operating band [GHz]	Gap [mm]	Gain improved by [dBi]	Directivity improved by [dBi]	3 dB bandwidth [%]
Proposed in [21]	2.4–11.2	5	3.5	-	36
From [22]	24.9–32.1	0.127	4	-	-
MPA with symmetric AMC	28–36	No gap	4.15	4	19.94
MPA with proposed asymmetric AMC	28.4–36	No gap	5.8	6	20

phase at 28.46 GHz. The difference between the resonance frequency of the AMC structures and the frequency corresponding to the maximum gain is due to the fact that a finite array is used as the ground plane, instead of its infinite variety. In addition, the 3 dB gain in the bandwidth of the antenna with the symmetric AMC ground plane is 19.94% (28–34.2 GHz) and 20% (29.6–36 GHz) for the antenna loaded by the asymmetric AMC ground plane. This corresponds to the operation band of AMC materials. Furthermore, above 35.4 GHz, the gain of the MPA alone is higher than that of the MPA loaded by AMC ground planes. Therefore, the AMC structures have a destructive effect on the antenna's radiations, because this range is outside the operation band of the AMC.

The curve of directivity for these antennas is presented in Fig. 12 and is higher for the proposed aerial, than for the conventional patch antenna. At 31.4 GHz, peak directivity for an antenna with the asymmetric AMC ground plane is 11.6 dBi, whereas peak directivity for the antenna with the well-known AMC ground plane is 9.6 dBi, so that an improvement of 132% and 92% is achieved, compared with that for the solo antenna, where the directivity has the maximum value of 5 dBi. The enhancement in directivity is caused by the effect of in-phase reflection phase. However, the improvement of directivity for the antenna loaded by the proposed asymmetric AMC ground plane is due to the discontinuity of the reflection phase behavior of the asymmetric AMC, which is higher than that for an MPA based on the well-known AMC ground plane.

For a further understanding of the antennas' performance, the radiation patterns of these antennas are presented in Fig. 13, in both XOY and YOZ planes, at the operating frequency. The omnidirectional radiation pattern is achieved for three antennas in the XOY plane, with a high level of gain for the asymmetric AMC-based microstrip antenna. For the YOZ plane, the radiation pattern for the antenna with the asymmetric AMC exhibits a low level of back lobes and a narrow beam width compared with that for the solo antenna system.

Table 1 shows the performance comparison of the studied antenna and other designs. In terms of peak gain and directivity, the asymmetric AMC ground plane antenna offers better performance. However, the 3 dB bandwidth is wider in [21], because the antenna is designed for UWB outdoor applications. The gap between the antenna and the AMC ground plane is another important criterion – it equaled, 5 mm in [21] and 0.127 mm in [22]. In the proposed design, there is no gap between the antenna and the AMC ground plane, which means that the proposed design is characterized by a lower thickness.

## 4. Conclusion

Conventional microstrip patch antennas with two different AMC ground planes are used to enhance gain and directivity. A symmetric AMC unit cell was designed and placed as the ground plane for a conventional MPA to enhance gain

and directivity of the antenna. The unit cell has a simple symmetric geometry, which leads to an angular stability and makes the reflection phase insensitive to polarization and to the incident angle of the incident plane wave. In addition, the 90° reflection phase bandwidth of 4.8 GHz (19.2%) is achieved. The second AMC unit cell has an asymmetric geometry, and it is characterized by the property of discontinuity in the reflection phase, which changes the nature of the impedance surface from capacitive to inductive. The results showed an enhancement by 207.14% in terms of gain, and by 132% in terms of directivity. This improvement is higher than that for the symmetric AMC structure which is characterized by the property of a 0° reflection phase. Both proposed antenna designs with AMC structures achieved better performance in terms of impedance matching, wider bandwidth, and a significant enhancement in gain and directivity, compared to the conventional MPA without an AMC structure.

## References

- [1] K. Hamaguchi *et al.*, "Development of millimeter-wave video transmission system-system design and performance for indoor BS signals transmission", in *Proc. 2001 Asia-Pacific Microwave Conf.*, vol. 2, Asia-Pacific, Taipei, Taiwan, 2001, pp. 492–497 (DOI: 10.1109/APMC.2001.985420).
- [2] F. K. Schwing, "Millimeter wave antennas", in *Proc. IEEE*, vol. 80, no. 1, 1992, pp. 92–102 (DOI: 10.1109/5.119569).
- [3] A. Elboushi, O. M. Haraz, A. Sebak, and T. Denidni, "A new circularly polarized high gain DRA millimeter-wave antenna", in *Proc. IEEE Antennas and Prop. Society Int. Symp.*, 2010, pp. 1–4 (DOI: 10.1109/APS.2010.5562140).
- [4] B. T. P. Madhav, G. J. Devi, P. Lakshman, and T. Anilkumar, "A CPW-fed sigma-shaped MIMO antenna for Ka band and 5G communication applications", *J. of Telecommun. and Inf. Technol.*, vol. 8, no. 4, pp. 97–106, 2018 (DOI: 10.26636/jtit.2018.123717).
- [5] S. Agarwal and P. Gupta, "High gain linear 1×4 x-slotted microstrip patch antenna array for 5G mobile technology", *J. of Telecommun. and Inf. Technol.*, vol. 1, pp. 50–55, 2020 (DOI: 10.26636/jtit.2020.137319).
- [6] D. Sievenpiper, L. Zhang, R. F. J. Broas, N. G. Alexopolous, and E. Yablonovitch, "High-impedance electromagnetic surfaces with a forbidden frequency band", *IEEE Trans. Microw. Theory Technol.*, vol. 47, no. 11, pp. 2059–2074, 1999 (DOI: 10.1109/22.798001).
- [7] R. Coccioli, F.-R. Yang, K.-P. Ma, and T. Itoh, "Aperture-coupled patch antenna on UC-PBG substrate", *IEEE Trans. Microw. Theory Technol.*, vol. 47, no. 11, pp. 2123–2130, 1999 (DOI: 10.1109/22.798008).
- [8] H. Malekpoor and S. Jam, "Improved radiation performance of low profile printed slot antenna using wideband planar AMC surface", *IEEE Trans. Antennas Propag.*, vol. 64, no. 11, pp. 4626–4638, 2016 (DOI: 10.1109/TAP.2016.2607761).
- [9] A. P. Feresidis, G. Goussetis, Shenhong Wang, and J. C. Vardaxoglou, "Artificial magnetic conductor surfaces and their application to low-profile high-gain planar antennas", *IEEE Trans. Antennas Propag.*, vol. 53, no. 1, pp. 209–215, 2005 (DOI: 10.1109/TAP.2004.840528).
- [10] M. A. Meriche, H. Attia, A. Messai, and T. A. Denidni, "Gain improvement of a wideband monopole antenna with novel artificial magnetic conductor", in *Proc. 17th Int. Symp. on Antenna Technol. and Applied Electromagnetics (ANTEM)*, 2016, pp. 1–2 (DOI: 10.1109/ANTEM.2016.7550150).

- [11] Y.-W. Zhong, G.-M. Yang, and L.-R. Zhong, "Gain enhancement of bow-tie antenna using fractal wideband artificial magnetic conductor ground", *Electron. Lett.*, vol. 51, no. 4, pp. 315–317, 2015 (DOI: 10.1049/el.2014.4017).
- [12] A. Ghosh, V. Kumar, G. Sen, and S. Das, "Gain enhancement of triple-band patch antenna by using triple-band artificial magnetic conductor", *IET Microw. Antennas Amp Propag.*, vol. 12, no. 8, pp. 1400–1406, 2018 (DOI: 10.1049/iet-map.2017.0815).
- [13] P. Yao, B. Zhang, J. Duan, and Q. Bai, "A novel low-scattering and wideband monopole antenna based on artificial magnetic conductor", *J. Phys. Conf. Ser.*, vol. 887, no. 1, pp. 12–37, 2017 (DOI: 10.1088/1742-6596/887/1/012037).
- [14] Y. Zheng, J. Gao, X. Cao, Z. Yuan, and H. Yang, "Wideband RCS reduction of a microstrip antenna using artificial magnetic conductor structures", *IEEE Antennas Wirel. Propag. Lett.*, vol. 14, pp. 1582–1585, 2015 (DOI: 10.1109/LAWP.2015.2413456).
- [15] P. Yao, B. Zhang, and J. Duan, "A broadband artificial magnetic conductor reflecting screen and application in microstrip antenna for radar cross-section reduction", *IEEE Antennas Wirel. Propag. Lett.*, vol. 17, no. 3, pp. 405–409, 2018 (DOI: 10.1109/LAWP.2018.2791662).
- [16] D. Sang, Q. Chen, L. Ding, M. Guo, and Y. Fu, "Design of checkerboard AMC structure for wideband RCS reduction", *IEEE Trans. Antennas Propag.*, vol. 67, no. 4, pp. 2604–2612, 2019 (DOI: 10.1109/TAP.2019.2891657).
- [17] J. Zhu, S. Li, S. Liao, and Q. Xue, "Wideband Low-Profile Highly Isolated MIMO Antenna With Artificial Magnetic Conductor", *IEEE Antennas Wirel. Propag. Lett.*, vol. 17, no. 3, pp. 458–462, 2018 (DOI: 10.1109/LAWP.2018.2795018).
- [18] S. Yan, P. J. Soh, and G. A. E. Vandenbosch, "Low-profile dual-band textile antenna with artificial magnetic conductor plane", *IEEE Trans. Antennas Propag.*, vol. 62, no. 12, pp. 6487–6490, 2014 (DOI: 10.1109/TAP.2014.2359194).
- [19] S. Lal, K. Subramanya, and R. Abhari, "Miniaturized EBG-backed textile microstrip patch antenna for Bluetooth wearable sensor applications", in *Proc. IEEE Int. Symp. on Antennas and Propag. (AP-SURSI)*, 2016, pp. 285–286 (DOI: 10.1109/APS.2016.7695851).
- [20] S. Zhu and R. Langley, "Dual-band wearable textile antenna on an EBG substrate", *IEEE Trans. Antennas Propag.*, vol. 57, no. 4, pp. 926–935, 2009 (DOI: 10.1109/TAP.2009.2014527).
- [21] R. P. Dwivedi, Md. Z. Khan, and U. K. Kommuri, "UWB circular cross slot AMC design for radiation improvement of UWB antenna", *AEU-Int. J. Electron. Commun.*, vol. 117, 2020 (DOI: 10.1016/j.aeue.2020.153092).
- [22] M. Xue, W. Wan, Q. Wang, and L. Cao, "Wideband low-profile Ka-band microstrip antenna with low cross polarization using asymmetry AMC structure", in *Proc. IEEE 69th Electronic Components and Technol. Conf. (ECTC)*, 2019, pp. 2318–2323 (DOI: 10.1109/ECTC.2019.00319).
- [23] D. F. Sievenpiper, "High-Impedance Electromagnetic Surfaces", Ph.D. Thesis, University of California, Los Angeles, California, 1999 [Online]. Available: <http://optoelectronics.eecs.berkeley.edu/ThesisDan.pdf>

**Khadija Belabbas** is currently pursuing the Ph.D. in Telecommunication and Microwave at Mohamed Boudiaf University, M'sila, Algeria. Her research interests include microstrip patch antennas, EBG-based antennas, and millimeter-wave antennas.

E-mail: khadija.belabbas@univ-msila.dz  
University of Mohamed Boudiaf M'sila  
BP.166, Route Ichebilia  
M'sila, Algeria



**Djamel Khedrouche** received his Ph.D. in Electronics Telecommunication in 2009 from Constantine University, Algeria. He is currently professor in Department of Electronics at University of Mohamed Boudiaf of M'sila, Algeria. His research interests include the modeling and characterization in electromagnetic and microwave devices. Recently, his research concerns microstrip antennas, UWB antennas and realizing advanced functional metamaterial devices.

University of Mohamed Boudiaf M'sila  
BP.166, Route Ichebilia  
M'sila, Algeria



**Abdesselam Hocini** received his Ph.D. in Electronics Instrumentation in 2008 from Constantine University, Algeria. He is currently professor in Department of Electronics at University of Mohamed Boudiaf of M'sila, Algeria. His research interests include the design and characterization

of photonic devices. In particular, his research concerns sensing, solar cells and realizing advanced functional photonic crystal devices.

University of Mohamed Boudiaf M'sila  
BP.166, Route Ichebilia  
M'sila, Algeria

# Orthogonal Harmonic Signals of the Generalized Class

Vitaliy Balashov, Vasyl Oreshkov, Iryna Barba, and Olena Iegupova

*O. S. Popov Odessa National Academy of Telecommunications, Odessa, Ukraine*

<https://doi.org/10.26636/jtit.2021.146720>

**Abstract**—Telecommunications transmission technologies with OFDM rely on orthogonal harmonic signal (OHS) systems. The criteria applicable to synthesizing OHS systems of the generalized class, including both classical signals and signals whose duration exceeds the orthogonality interval, have been considered. The problems of minimizing the effective width of the spectrum of the generalized class OHS have been solved. Estimates of the efficiency of the generalized class OHS have been given.

**Keywords**—Fourier transformation, OFDM, orthogonal harmonic signals, orthogonality interval, signal envelope.

## 1. Introduction

In recent years, thanks to the success of digital signal processing, orthogonal frequency division multiplexing (OFDM) transmission technologies have become increasingly popular in telecommunications and have been relied upon to transmit broadband orthogonal harmonic signal (OHS) systems [1]–[3]. Today, digital subscriber line (xDSL) transmission technologies are, in accordance with recommendations of the International Telecommunication Union (ITU-T) G.992 and G.993, the most common solutions used to offer broadband access via well-developed subscriber networks [4], [5]. In 2014, ITU adopted Recommendation G.9701 defining the characteristics of the G.fast transmission technology. It relies on the OHS and provides signals through a multi-pair telephone cable, with the speed of up to 1 Gbit/s and in the frequency band of up to 106 MHz [6].

Various OHS systems are used in modern radio access systems, including Wi-Fi (IEEE 802.11), WiMAX (IEEE 802.16), and LTE. They are also relied upon in high-quality digital radio and television broadcasting systems [7]–[10]. The transmission of signals through optical cables is a new area of telecommunications, where OFDM technologies have begun to be used intensively. OHS allows to increase the efficiency of optical transmission technologies relying on dense wavelength division multiplexing (DWDM) [11]–[14].

## 2. Problem Statement

The widespread use of transmission systems (TSs) with OHS in communication networks results from the fact that these technologies ensure high efficiency of transmitting

information via communication channels with abnormal and unstable frequencies, as well as with noise characteristics over time.

OHS systems are described by real trigonometric functions which are orthogonal by interval  $\tau_0$ :

$$\{\cos(l\omega_0 t), \sin(l\omega_0 t)\}, \quad l = 0, 1, 2, \dots, N-1, \\ \omega_0 = 2\pi f_0 = \frac{2\pi}{\tau_0}, \quad -\frac{\tau_0}{2} \leq t < \frac{\tau_0}{2}, \quad (1)$$

where  $N$  is the total number of orthogonal functions in the  $0 - \omega_B$  frequency band,  $\omega_B = N \cdot \omega_0$  is the upper frequency of the transmission channel bandwidth,  $\omega_0$  is the frequency of the first OHS system harmonic,  $\tau_0$  is the orthogonality interval.

Examples of orthogonal harmonic signals from Eq. (1) for  $l = 4, 5, 6, 22$  are given in Fig. 1.

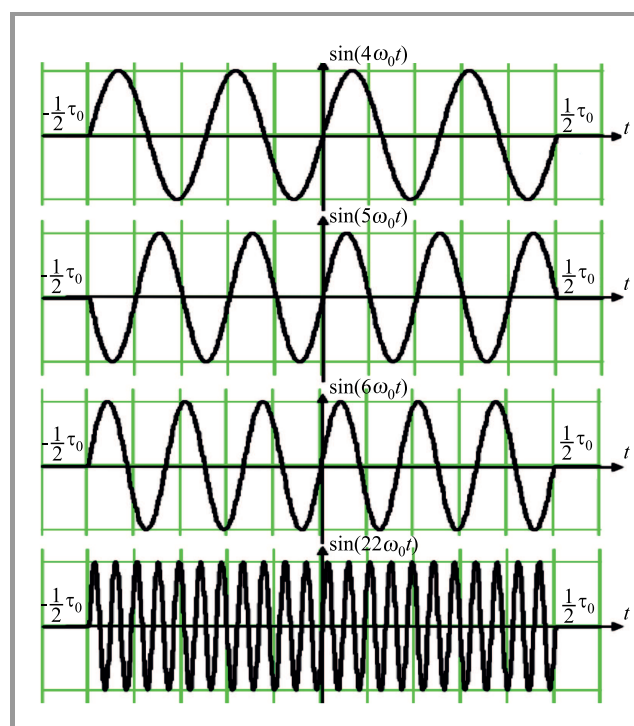


**Fig. 1.** Orthogonal harmonic signal graphs.

Functions from Eq. (1) are related by the Euler relation:

$$e^{il\omega_0 t} = \cos(l\omega_0 t) + i \sin(l\omega_0 t), \quad (2)$$



with exponential time functions:

$$\{e^{il\omega_0 t}\}_{l=0}^{N-1}, -\frac{\tau_0}{2} \leq t < \frac{\tau_0}{2}. \quad (3)$$

Signal spectra of Eq. (1) have a sufficiently high concentration of energy in the frequency domain (see Fig. 2) and there are effective algorithms for digital processing of OHS systems using Fourier transformation algorithms and providing an acceptable computational complexity of signal modulation-demodulation algorithms in TS with a significant number of signals.

The transformation (spectrum) of Fourier functions given by Eq. (3) is described by the following formula:

$$\begin{aligned} S(\omega - l\omega_0) &= \int_{-\frac{\tau_0}{2}}^{\frac{\tau_0}{2}} e^{il\omega_0 t} e^{-i\omega t} dt \\ &= \frac{\sin(\omega - l\omega_0)\frac{\tau_0}{2}}{(\omega - l\omega_0)}, -\infty < \omega < \infty. \end{aligned} \quad (4)$$

Examples of envelope spectrum graphs defined by Eq. (4) for  $l = 4, 5, 6, 22$  are shown in Fig. 2.

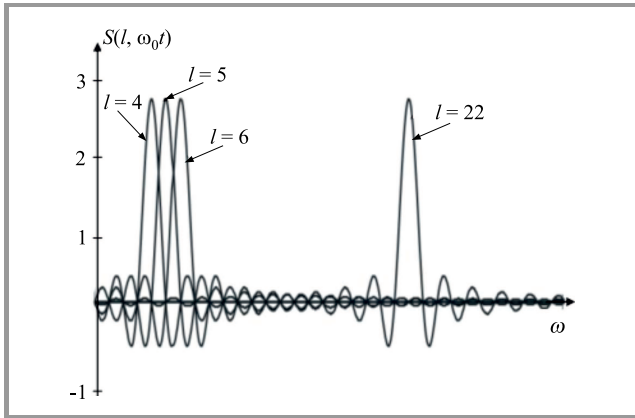


Fig. 2. Example of OHS envelope spectra.

The signal spectra are theoretically infinite and decreases in frequency at a rate proportional to  $1/\omega$ . When OHS signals pass through a communication channel with a limited bandwidth, their spectra are truncated. As a result, the orthogonality of the received signals is damaged, and, therefore inter-symbol and inter-channel interference noises are generated. Based on Eq. (1), it is possible to design systems of orthogonal signals with a higher concentration of energy in the frequency domain than with classical OHS. These signals pass through a communication channel with a distorting transmission function. They are less distorted, offer lower interference levels and are more immune to frequency characteristics variations in the communication channel than traditional OHS.

Let us formulate the following OHS synthesis task with energy concentration in the frequency domain that is higher than in the classical OHS, in order to determine the conditions when the system of functions is:

$$\begin{aligned} \left\{ \sqrt{u(t)} e^{il\omega_0 t} \right\}_{l=0}^{N-1}, -\frac{T}{2} \leq t < \frac{T}{2}, \\ \omega_0 = 2\pi f_0, \tau_0 = \frac{1}{f_0}, \end{aligned} \quad (5)$$

with orthogonal by interval  $T$ , such as:

$$\begin{aligned} \int_{-\frac{T}{2}}^{\frac{T}{2}} \sqrt{u(t)} e^{il\omega_0 t} \sqrt{u(t)} e^{-ik\omega_0 t} dt \\ = \begin{cases} 1, & l = k, \\ 0, & l \neq k, \end{cases} \quad T \geq \tau_0, \end{aligned} \quad (6)$$

where  $\sqrt{u(t)}$  is the function describing the envelope of signals and  $T$  is the duration of functions.

Signals from Eq. (5) that satisfied Eq. (6) will be referred to OHS of the generalized class.

Based on the Parseval-Plancherel equality and the filtering property of the  $\delta$ -function, the condition in Eq. (6) can be transformed as:

$$\begin{aligned} \int_{-\frac{T}{2}}^{\frac{T}{2}} \sqrt{u(t)} e^{il\omega_0 t} \sqrt{u(t)} e^{-ik\omega_0 t} dt \\ = \frac{1}{2\pi} \int_{-\infty}^{\infty} U(i\omega) 2\pi \delta[\omega - (k-l)\omega_0] d\omega \\ = U[(k-l)\omega_0] = \begin{cases} 1, & l = k, \\ 0, & l \neq k, \end{cases} \end{aligned} \quad (7)$$

where  $U(\omega)$  is the Fourier transformation (spectrum) of the function (envelope)  $u(t)$ ,  $2\pi\delta[\omega - (k-l)\omega_0]$  is the spectrum of exponential signal.

For the discrete frequency function defined by Eq. (7), the Fourier transformation is:

$$U(k\omega_0) = \int_{-\infty}^{\infty} u(t) e^{-ik\omega_0 t} dt = \begin{cases} 1, & k = 1 \\ 0, & k \neq 0 \end{cases}. \quad (8)$$

Let us convert the last expression using parameters  $T$  and  $\tau_0$ :

$$U(k\omega_0) = \sum_{n=-\infty}^{\infty} \int_{-\frac{T}{2}+n\tau_0}^{\frac{T}{2}+n\tau_0} u(t-n\tau_0) e^{-ik\omega_0 t} dt, \quad (9)$$

and replace the variables  $\tau = t - n\tau_0$ :

$$\begin{aligned} U(k\omega_0) &= \sum_{n=-\infty}^{\infty} \int_{-\frac{T}{2}}^{\frac{T}{2}} u(\tau) e^{-ik\omega_0(\tau+n\tau_0)} d\tau \\ &= \sum_{n=-\infty}^{\infty} e^{-ik\omega_0 n\tau_0} \int_{-\frac{T}{2}}^{\frac{T}{2}} u(\tau) e^{-ik\omega_0 \tau} d\tau. \end{aligned} \quad (10)$$

Under the sum sign is the product of the spectrum of the function  $u(\tau)$  per exponent. It corresponds to the spectrum of the function delayed by  $n\tau_0$ :

$$\begin{aligned} U(k\omega_0) &= \sum_{n=-\infty}^{\infty} \int_{-\frac{T}{2}}^{\frac{T}{2}} u(\tau - n\tau_0) e^{-ik\omega_0 \tau} d\tau \\ &= \int_{-\frac{T}{2}}^{\frac{T}{2}} \sum_{n=-\infty}^{\infty} u(\tau - n\tau_0) e^{-ik\omega_0 \tau} d\tau = \begin{cases} 1, & k = 0 \\ 0, & k \neq 0 \end{cases}. \end{aligned} \quad (11)$$

A function spectrum containing a constant component only corresponds to a function which is constant over time. Therefore:

$$\sum_{n=-\infty}^{\infty} u(\tau - n\tau_0) = \text{const} . \quad (12)$$

Thus, the following statement has been proved. In order for the signal system from Eq. (5) to be orthogonal, it is necessary for the sum of the shifts of function  $u(t)$  (the square of the envelope) by  $n\tau_0$ ,  $n = \pm 0, \pm 1, \pm 2, \dots$  be a constant value (see Fig. 3, where dotted lines are the functions  $u(t)$  shifted by  $\tau_0$ ).

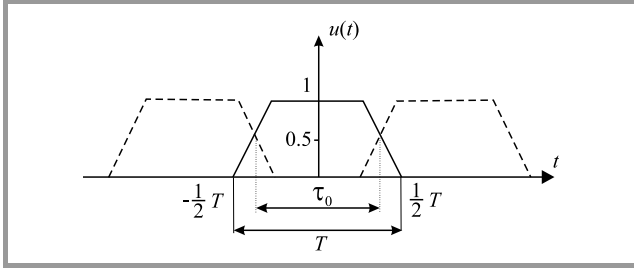


Fig. 3. Graph illustrating criterion.

Note that the condition, defined by Eq. (6), of signal orthogonality from Eq. (5) also describes the rule for correlation reception of OHS signals in the OFDM transmission technology. In this case, it follows from Eq. (6) that the resulting frequency characteristics when receiving signals are determined not by the envelope function  $\sqrt{u(t)}$ , but by the function  $u(t)$  itself. On this basis, further attention will be paid to the synthesis and characteristics of the functions  $u(t)$ .

### 3. Method for Synthesizing OHS Envelope of the Generalized Class

Here, the method for synthesizing signals  $u(t)$ , according to the criterion shown in Eq. (12), is presented. Signal  $u(t)$  is considered to be the convolution of signal  $p(t) = 1, -\tau_0/2 \leq t < \tau_0/2$  of a rectangular shape and symmetrical (second order symmetry) in the middle of signal  $\varphi(t), -\tau/2 \leq t < \tau/2$ , where  $\tau = T - \tau_0$ . The resulting signal has edges that are symmetric to the boundaries of the interval  $(-\tau_0/2, \tau_0/2)$ , and it meets condition (12).

Signal spectrum  $u(t)$  is equal to the product of signal spectra  $p(t) - P(\omega)$  and  $\varphi(t) - \phi(\omega)$ :

$$U(i\omega) = P(i\omega) \times \phi(i\omega) . \quad (13)$$

The following optimization problem defines if  $u(t)$  signals synthesized using the proposed method have the minimum effective spectrum width. Obviously, with the same  $T$  and  $\tau_0$  parameters, the spectral characteristics of  $u(t)$  signals will be determined by the spectrum of the  $\varphi(t)$  signal. Thus, the problem is to find  $\varphi(t), -\tau/2 \leq t < \tau/2$  with the minimum permissible effective spectrum width.

The formulated rule is a classical optimization problem and has a number of solutions depending on additional optimization conditions [15].

One of the solutions consists in using the pulse described by [15]:

$$\varphi(t) = \sqrt{\frac{2}{\tau}} \cos \frac{\pi}{\tau} t, \quad -\frac{\tau}{2} \leq t < \frac{\tau}{2} . \quad (14)$$

A graph of  $\varphi(t)$  signal with the minimum effective spectrum is shown in Fig. 4.

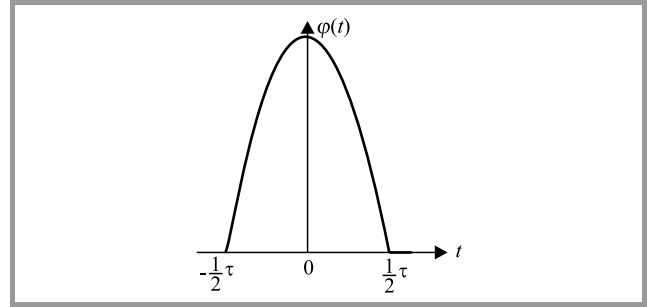


Fig. 4. Pulse of duration  $\tau$  with minimum effective spectrum width.

Figure 5 illustrates the given synthesis method of function  $u(t)$  in the form of convolution of signal  $p(t) = 1, -\tau_0/2 \leq t < \tau_0/2$ , with signal  $\varphi(t), -\tau/2 \leq t < \tau/2$ , described by the function from Eq. (14).

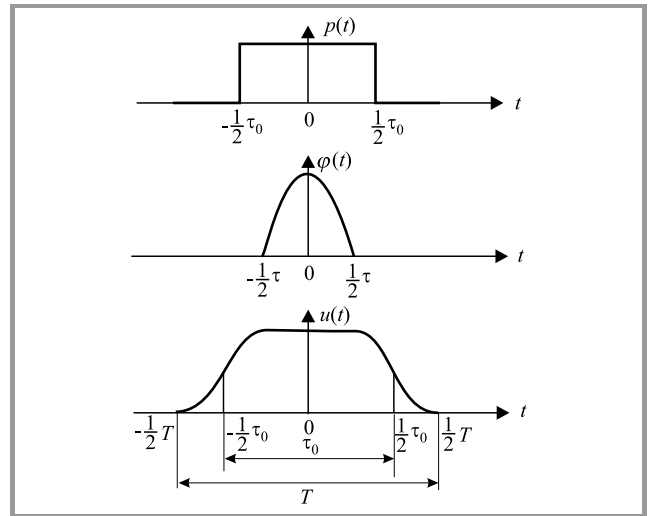


Fig. 5. Convolution of function  $\varphi(t)$  with function  $p(t) = 1$ .

Taking into account the corresponding normalization, the optimal function  $u(t)$  is described by:

$$u(t) = \begin{cases} 1, & \text{at } |t| \leq (1-\alpha)\frac{\tau_0}{2} \\ \cos^2 \frac{\pi}{4\alpha} [2f_0|t| + \alpha - 1], & \text{at } (1-\alpha)\frac{\tau_0}{2} \leq |t| < (1+\alpha)\frac{\tau_0}{2} , \\ 0, & \text{in all other cases} \end{cases} , \quad (15)$$

where  $\alpha = (T - \tau_0)/\tau_0$  is a signal expansion coefficient.



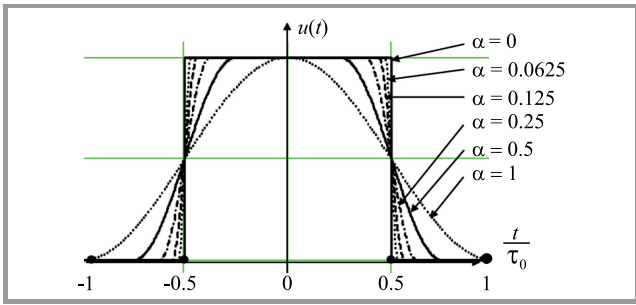


Fig. 6. Optimal  $u(t)$  functions.

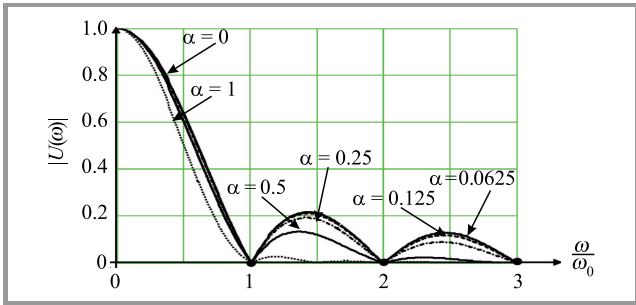


Fig. 7. Spectra module graph  $U(\omega)$ .

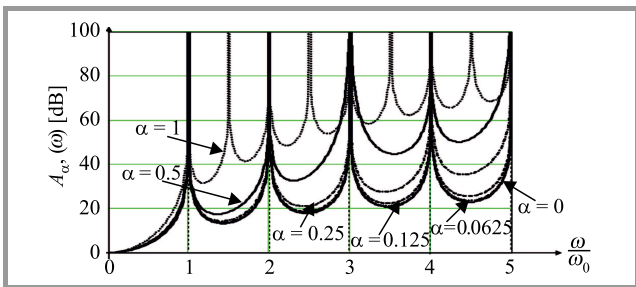


Fig. 8. Graphs of function  $A_\alpha(\omega)$  of optimal generalized class OHS.

Equation (15) describes a function with cosine quadratic edges. Graph  $u(t)$  with signal expansion coefficient values

of  $\alpha = 0, 0.0625, 0.125, 0.25, 0.5$  and  $1$  is given in Fig. 6. Figure 7 shows the spectra module graphs  $U(\omega)$  of optimal functions  $u(t)$ .

To illustrate the positive energy concentration effect of the spectra generalized class OHS, provided by the optimal functions  $u(t)$ , let us normalize the energy at frequency  $\omega = 0$  in decibels:

$$A_\alpha(\omega) = 10 \log \frac{U^2(0)}{U^2(\omega)}. \quad (16)$$

Graphs  $A_\alpha(\omega)$  depicting spectral energy concentration calculated by Eq. (16) with signal expansion coefficient values of  $\alpha = 0, 0.0625, 0.125, 0.25, 0.5$  and  $1$  are shown in Fig. 8. Figure 9 shows examples of orthogonal signals  $s_1(t) = u(t) \sin(\omega_0 t)$  and  $s_2(t) = u(t) \sin(2\omega_0 t)$  of the generalized class OHS system with functions  $u(t)$  being optimal if values of the signal expansion coefficient are  $\alpha = 0, 0.25, 0.5$  and  $1$ .

### 4. Extension of the Class of Orthogonal Signals

The above-described method used for synthesizing generalized class OHS types may be used for synthesis of other OHS systems as well.

It is easy to verify the hypothesis that the temporary function  $u_1(t), -\tau_0 \leq t < \tau_0$  shown as an example in Fig. 10a, consisting of intervals:

$$\begin{aligned} u_{1-1}(t), & \quad -\tau_0 \leq t < -\frac{7}{8}\tau_0, \\ u_{1-2}(t), & \quad -\frac{3}{4}\tau_0 \leq t < -\frac{1}{2}\tau_0, \\ u_{1-3}(t), & \quad -\frac{1}{4}\tau_0 \leq t < -\frac{1}{8}\tau_0, \\ u_{1-4}(t), & \quad \frac{1}{8}\tau_0 \leq t < \frac{1}{4}\tau_0, \\ u_{1-5}(t), & \quad \frac{1}{2}\tau_0 \leq t < \frac{3}{4}\tau_0, \text{ and} \\ u_{1-6}(t), & \quad \frac{7}{8}\tau_0 \leq t < \tau_0 \end{aligned}$$

satisfies condition (12) with displacement if  $n\tau_0$  for  $n = \pm 0, \pm 1, \pm 2$ .

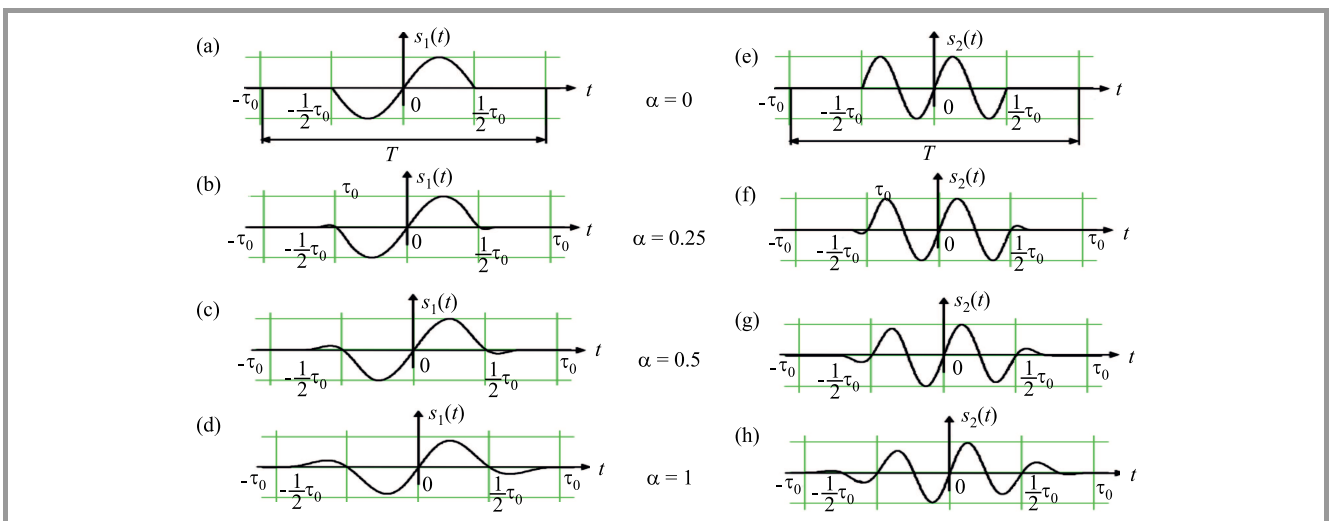
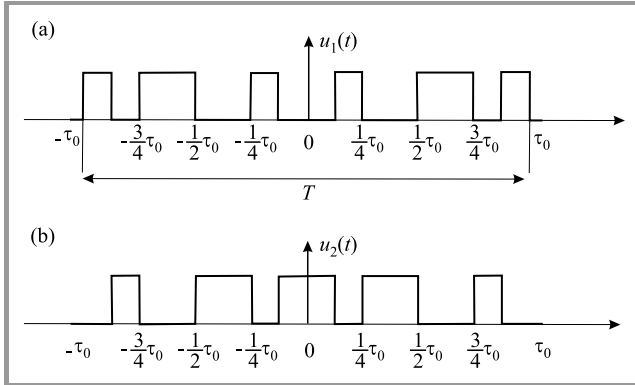


Fig. 9. Examples of the generalized class OHS  $s_1(t)$  and  $s_2(t)$  with optimal functions  $u(t)$  if  $\alpha = 0, 0.25, 0.5$  and  $1$ .

Figure 10b shows another function,  $u_2(t)$ ,  $-\tau_0 \leq t < \tau_0$ , also satisfying condition (12). From the graphs of functions  $u_1(t)$  and  $u_2(t)$ , it is obvious that the given functions are orthogonal.



**Fig. 10.** Example of a piecewise constant functions for the criterion (12).

Hence, it has been justified that the criterion of OHS orthogonality in Eq. (12), at a certain level of  $\tau_0$  and with the uninterrupted envelopes  $u(t)$  considered, also meets the plurality of piecewise-constant functions  $u(t)$ . Their application allows to synthesize the corresponding OHS systems of the generalized class.

Figure 11 shows examples of the given signals  $s_1(t)$  and  $s_2(t)$  of the OHS system with the piecewise constant envelope function  $u_1(t)$ , see Fig. 10a.

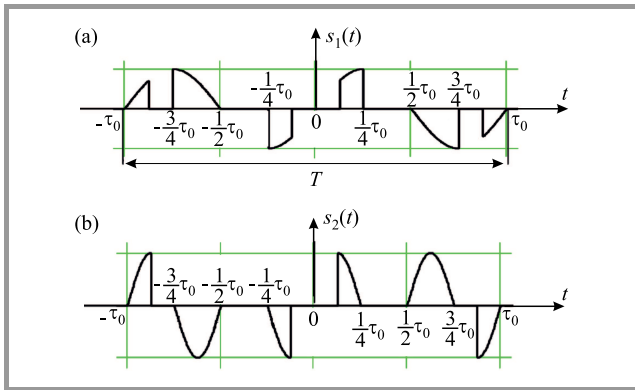


**Fig. 11.** Examples of OHS  $s(t)$  with piecewise constant envelopes with criterion (12).

For the OHS of the generalized class using piecewise-constant functions  $u(t)$ , the orthogonality criterion from Eq. (6) should be added with the following conditions:

- signals  $u(t)$  are symmetrical along axis  $u(0)$ ,
- interval  $\tau_0 = \sum_i \Delta\tau_i$ , where  $\Delta\tau_i$  is the duration of  $i$ -th interval of function  $u(t)$ ,  $-\frac{T}{2} \leq t < \frac{T}{2}$ ,
- the interval of function  $u(t)$  satisfies the condition  $T \geq 2\tau_0$ .

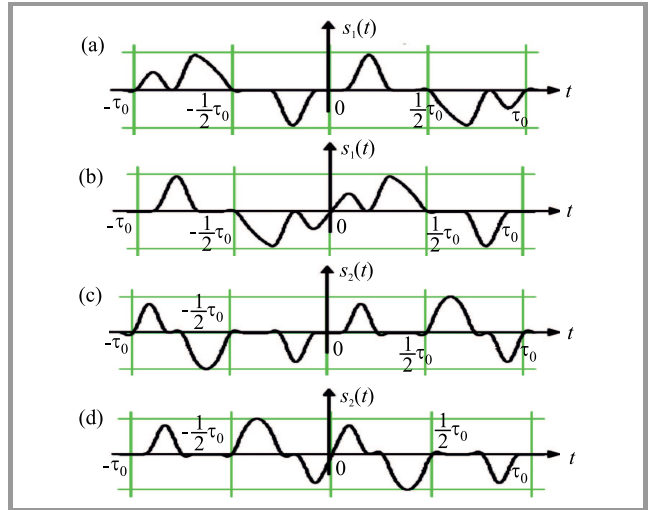


**Fig. 12.** Examples of OHS  $s(t)$  with piecewise constant envelopes with cosine-quadratic fronts ( $\alpha = 0.0625$ ).

It is also easy to verify compliance the criterion (12) of piecewise-constant envelope functions  $u(t)$  with fronts having the second-order symmetry. Figure 12 shows examples of such functions  $u_1(t)$  and  $u_2(t)$  with cosine-quadratic fronts corresponding to piecewise constant envelope functions  $u_1(t)$  and  $u_2(t)$ , with the signal expansion coefficient of  $\alpha = 0.0625$ .

## 5. Conclusions

The article defines a generalized class of orthogonal harmonic signals (OHS) and the following results are obtained.

1. The synthesis problem for OHSs that are orthogonal with the interval of  $T$ ,  $\tau_0 \leq T < 2\tau_0$  is presented.
2. Criteria for the synthesis of functions  $u(t)$  of the generalized class OHS are defined.
3. Function  $u(t)$  is proposed to be synthesized as a convolution of the  $p(t) = 1, -\frac{1}{2}\tau_0 \leq t < \frac{1}{2}\tau_0$  rectangular signal, symmetrical along the middle of the  $\varphi(t), -\frac{1}{2}\tau \leq t < \frac{1}{2}\tau$ , signal, where  $\tau = T - \tau_0$ . The edges of the resulting signal are symmetrical relative to the boundaries of the  $[-\frac{1}{2}\tau_0, \frac{1}{2}\tau_0]$  interval and satisfy condition (12).
4. The problem of optimizing the synthesis for  $u(t)$  functions with the minimum effective spectrum width  $U(\omega)$  at given  $T$  and  $\tau_0$  parameters is solved. The solution to the problem is a function with cosine-square fronts, known in theory, which is a convincing proof of the correctness (validity) of the authors' proposals presented in the article.


5. To estimate the energy concentration gain, provided by the optimal  $u(t)$  functions,  $U(\omega)$  spectra were calculated for different values of the signal expansion coefficient  $\alpha$ .
6. It has been demonstrated that the OHS orthogonality criterion for a certain selection of  $\tau_0$ , along with the considered  $u(t)$  continuous functions, also corresponds to the set of piecewise constant functions  $u(t)$ , the application of which allows to synthesize the corresponding OHS systems of the generalized class.

## References

- [1] V. A. Balashov, P. P. Vorobienko, and L. M. Liakhovetskyi, *Systemi Peredachi Ortogonalnimi Garmonicheskimi Signalami*. Eko-trendz, 2012 (ISBN: 978-5-88405-096-9) (in Ukrainian).
- [2] V. Oreshkov, O. Iegupova, and I. Barba, "Efficiency of generalized class orthogonal harmonic signals application in G.fast transmission systems", in *Proc. 14th Int. Conf. on Adv. Trends in Radioelec., Telecommun. and Comp. Engin. TCSET*, Slavske, Ukraine, 2018, pp. 987–990 (DOI: 10.1109/TCSET.2018.8336360).
- [3] V. Oreshkov, I. Barba, and V. Balashov, "Compensation of crosstalk in the parallel operation of G.fast systems over TPP type multi-bundle telephone cables", in *Proc. Int. Conf. on Inform. and Telecommun. Technol. and Radio Electronics UkrMiCo*, Odessa, Ukraine, 2018, pp. 1–5 (DOI: 10.1109/UkrMiCo43733.2018.9047517).
- [4] Recommendation ITU-T G.992.5, "Asymmetric digital subscriber line 2 transceivers (ADSL2) – Extended bandwidth ADSL2 (ADSL2plus)" [Online]. Available: <https://www.itu.int/rec/T-REC-G.992.5-200901-I/en>
- [5] Recommendation ITU-T G.993.2, "Very high speed digital subscriber line transceivers 2 (VDSL2)" [Online]. Available: <https://www.itu.int/rec/T-REC-G.993.2-201902-I/en>
- [6] Recommendation G.9701, "Fast access to subscriber terminals (G.fast) – Physical layer specification" [Online]. Available: <https://www.itu.int/rec/T-REC-G.9701-201903-I/en>
- [7] "Standard for Information Technology – Telecommunications and Information Exchange Between Systems Local and Metropolitan Area Networks – Specific Requirements – Part 11: Wireless LAN Medium Access Control (MAC) and Physical Layer (PHY) Specifications Amendment: Light Communications", IEEE Std 802.11-2016, 2016, pp. 1–3534 (DOI: 10.1109/IEEESTD.2016.7786995).
- [8] "Standard for Local and metropolitan area networks Part 16: Air Interface for Broadband Wireless Access Systems", IEEE Std 802.16-2004, 2019, pp. 1–2080 (DOI: 10.1109/IEEESTD.2009.5062485).
- [9] "Radio broadcasting systems; digital audio broadcasting (DAB) to mobile, portable and fixed receivers", ETSI EN 300 401, vol. 2, 2016 [Online]. Available: [https://www.etsi.org/deliver/etsi\\_en/300400\\_300499/300401/02.01.01\\_20/en\\_300401v020101a.pdf](https://www.etsi.org/deliver/etsi_en/300400_300499/300401/02.01.01_20/en_300401v020101a.pdf)
- [10] "Digital Video Broadcasting (DVB); Framing structure, channel coding and modulation for digital terrestrial television", ETSI EN 300 744, 2015 [Online]. Available: [https://www.etsi.org/deliver/etsi\\_en/300700\\_300799/300744/01.06.02\\_60/en\\_300744v010602p.pdf](https://www.etsi.org/deliver/etsi_en/300700_300799/300744/01.06.02_60/en_300744v010602p.pdf)
- [11] D. J. F. Barros and J. M. Kahn, "Optimized dispersion compensation using orthogonal frequency-division multiplexing", *J. of Lightwave Technol.* vol. 26, no. 16, pp. 2889–2898, 2008 [Online]. Available: <https://www.osapublishing.org/jlt/viewmedia.cfm?uri=jlt-26-16-2889&seq=0>
- [12] X. Zhang, J. Li, and Z. Li, "SSBI cancellation method for IMDD-OFDM system with a single photodiode", in *Proc. PIERS*, 2014, pp. 2719–2722 (ISBN: 9781510815605).
- [13] P. Torres-Ferrera, S. O. Vázquez, and R. Gutiérrez-Castrejón, "4×100 Gb/s WDM DD-OFDM using EAM for next generation Ethernet transceivers over SMF", *Optics Commun.*, vol. 365, pp. 86–92, 2016 (DOI: 10.1016/j.optcom.2015.11.063).
- [14] V. A. Vardanyan, "Estimation and compensation of signal-signal beating interference in direct detection fiber-optical transmission systems of OFDM signals", *Proc. Optoelectron., Instrument. and Data*, vol. 54, no. 3, 2018, pp. 292–300 (DOI: 3103/S8756699018030123).
- [15] R. Kurant and D. Gilbert, *Methods of Mathematical Physics*. Wiley Eastern Limited, 1953 (ISBN: 9780852261316).



**Vitaliy Balashov** has a Ph.D. degree in Technical Sciences and is a Professor at the O. S. Popov Odessa National Academy of Telecommunications, Odessa, Ukraine. He is the author of 170 scientific and educational works, has earned 24 patents for invention, and has published 7 monographs. His research interests include the telecommunication theory and the OFDM system telecommunication theory.


 <https://orcid.org/0000-0001-6122-4647>

E-mail: [bvaoniis@gmail.com](mailto:bvaoniis@gmail.com)

O. S. Popov Odessa National Academy of Telecommunications  
Kuznechnaya, 1,  
65029 Odessa, Ukraine



**Vasyl Oreshkov** holds a Ph.D. in Technical Sciences. He is a Senior Lecturer at the O. S. Popov Odessa National Academy of Telecommunications, Odessa, Ukraine. He is the author of more than 102 scientific and educational works, including 78 scientific articles and conference abstracts, has earned 2 patents for invention, and has published 7 monographs, as well as 15 educational and methodical manuals. His research interests include the theory of transmission systems with orthogonal harmonic signals, electromagnetic compatibility of transmission systems and development of broadband access networks.

 <https://orcid.org/0000-0001-9796-0216>


E-mail: [Oreshkov.VI@ukr.net](mailto:Oreshkov.VI@ukr.net)

O. S. Popov Odessa National Academy of Telecommunications  
Kuznechnaya, 1,  
65029 Odessa, Ukraine



**Iryna Barba** holds a Ph.D. in Technical Sciences and is a Senior Lecturer at the O.S. Popov Odessa National Academy of Telecommunications, Odessa, Ukraine. She is the author of more than 50 scientific publications, including 30 conference abstracts, 9 of which are indexed in the Scopus scientific-metric

database, 18 articles, 1 patent and 2 monographs.

 <https://orcid.org/0000-0002-6751-0086>

E-mail: [ibarba@onat.edu.ua](mailto:ibarba@onat.edu.ua)


O. S. Popov Odessa National Academy of Telecommunications

Kuznechnaya 1,  
65029 Odessa, Ukraine



**Olena Iegupova** is a graduate student of the O.S. Popov Odessa National Academy of Telecommunications, Odessa, Ukraine. She is the author of 18 scientific and educational works, including 5 scientific articles, 12 conference abstracts and 1 monograph. Her research interests include improving the efficiency of broadband signal

transmission technologies over telephone networks.

 <https://orcid.org/0000-0003-1540-2988>

E-mail: [elena.iegupova@gmail.com](mailto:elena.iegupova@gmail.com)

O. S. Popov Odessa National Academy of Telecommunications

Kuznechnaya, 1,  
65029 Odessa, Ukraine

# Optimization of Gyrotron Resonator's Dimensions

Kacper Nowak<sup>1</sup> and Olgierd Dumbrajs<sup>2</sup>

<sup>1</sup> Faculty of Electronics, Wrocław University of Science and Technology, Wrocław, Poland

<sup>2</sup> Institute of Solid State Physics, University of Latvia, Riga, Latvia

<https://doi.org/10.26636/jtit.2021.147120>

**Abstract**— This paper explains the procedure of determining the initial dimensions of a gyrotron resonator. In particular, the paper discusses which geometrical parameters impact the wave properties of the resonator. The solution is implemented using Matlab software and estimations are performed with the use of the SMath Studio spreadsheet.

**Keywords**—gyrotron design, cold cavity, Matlab code.

## 1. Introduction

Gyrotron-related theory and equations have been known since the 1960s [1]–[4]. Numerical computation methods and computer technologies have evolved significantly since that time. Simulation software, such as CST Microwave Studio, is capable of performing EM field calculations pertaining to any structure. However, due to fact that every computer simulation consists of input data and produces some output data, two questions are always valid: “what are the proper input data?” and “are the output results in agreement with the laws of physics?”. In this paper, we will provide a Matlab numerical solution based on the cold cavity approach in order to obtain the initial dimensions of a gyrotron resonator. The proposed approach may be justified by the simplifications introduced to the equations, which, in turn, make computer-based implementation not excessively complicated. Further geometry optimizations may be performed using commercial, full-wave, microwave simulation software, but a starting point needs to be defined that is close to the optimal solution. The results obtained using CST Microwave Studio are much closer to actual experiment outcomes than those offered by simplified mathematical models, but are more computationally expensive. Therefore, the cold cavity approach and full-wave simulation are two complementary methods that are relied upon jointly.

## 2. Cold Cavity Formalism

In the presented approach, the cold cavity model is used to obtain the initial geometry of the resonator's microwave structure.

The formula is developed from the string equation (stationary Schrodinger equation):

$$\begin{cases} \frac{d^2 f}{dz^2} + k_z^2(\omega, z) f = 0 \\ k_z^2(\omega, z) = \left(\frac{k}{c}\right)^2 - k_{\perp}^2(z), \quad k_{\perp} = \frac{v_{m,k}}{R(z)}, \quad k = \omega \sqrt{\left(1 + \frac{i}{Q}\right)} \end{cases} \quad (1)$$

When substituting  $k$  and  $k_{\perp}$  with  $k_z$  followed by substituting  $k_z$  in Eq. (1), a differential formula for the cold cavity model is obtained:

$$\frac{d^2 f}{dz^2} + \left[ \left(\frac{\omega}{c}\right)^2 \left(1 + \frac{i}{Q_{diff}}\right) - \left(\frac{v_{m,k}}{R(z)}\right)^2 \right] f = 0. \quad (2)$$

This describes the RF field profile as a function of the  $z$  dimension of the resonator. The longitudinal field profile  $f$  is important for a few reasons. It is desired for the EM field to create a stationary wave that fulfills the boundary conditions and suffers from small diffraction losses, so that the overall microwave efficiency is high. There is also a second very important factor that requires knowledge of the EM field profile – electron cyclotron resonance. This is the mechanism for transferring energy from electrons to the EM field. It is desired that electron orbits and speeds of their travel in the  $z$  direction be chosen in such a way that most electrons transfer as much energy as possible to the microwave field, and then leave the resonator. To optimize these two factors which have a direct impact on gyrotron efficiency, Eq. (2) is crucial.

The boundary conditions for the stationary state are expressed as:

$$\begin{cases} \left. \frac{df}{dz} \right|_{z_{in}} - ik_z(z_{in})f(z_{in}) = 0 \\ \left. \frac{df}{dz} \right|_{z_{out}} + ik_z(z_{out})f(z_{out}) = 0 \end{cases} \quad (3)$$

The first part ( $z_{in}$ ) of Eq. (3) describes the input boundary condition for the left-hand side of Fig. 1. This boundary condition represents the total internal reflection of the EM wave. Moreover, electric field energy is not propagating in the  $-z$  direction and, therefore, this boundary condition is that of an evanescent wave. The input boundary condition is used to define  $\left. \frac{df}{dz} \right|_{z_{in}}$  – starting point for integration of the model Eq. (2). The second part ( $z_{out}$ ) describes



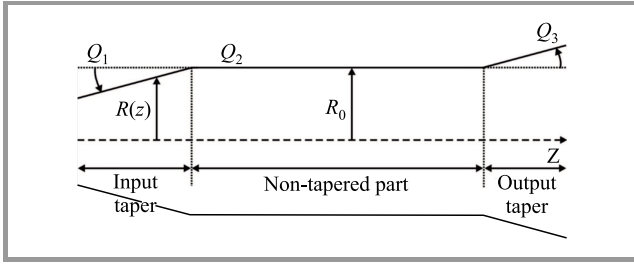


Fig. 1. Longitudinal profile of the resonator (along  $z$  axis).

the minimum reflection boundary conditions that are required for the EM wave to leave the resonator. The output boundary condition may be expressed as Eq. (4).  $|R|$  may be referred to as the reflection coefficient.

$$|R| = \left| \frac{\frac{df}{dz} + ik_z f}{\frac{df}{dz} - ik_z f} \right|_{z=z_{out}} = \text{minimum}. \quad (4)$$

The solution is found by optimizing Eq. (2). To achieve this goal, minimalization of Eq. (4) in the two-dimensional space of  $\omega$  and  $Q$  is performed. In this model, the first harmonic and the single mode scenario are considered. The presented formalism was chosen for consideration because of its simplicity which, in turn, leads to a shorter implementation time and makes it more computationally efficient. Moreover, higher accuracy is not required at this step of the gyrotron design process, due to the fact that a precise final geometry is obtained using commercial full-wave microwave simulation software.

### 3. The Solution

This chapter explains all the definitions and steps necessary to find the solution. Physical constant values are included in the source code in the “PhysicalConstants.m” file. Readers should pay particular attention to the units used, as the constants are shown in gigahertz, millimeters and nanoseconds. The source code for the sample gyrotron cavity design is attached to this paper and may be downloaded. The code is written using the Matlab package.

To solve the second order differential equation, the ode45 Matlab solver is used. In this model, the second order equation is simplified to the first order differential equation system, and therefore the ode45 Matlab solver is used. It makes the problem much simpler and, more importantly, the Dormand Prince ode4 algorithm with fifth order verification is well documented in the literature [5].

In order to start the calculations, the working frequency needs to be assumed arbitrarily. In this paper, the gyrotron being designed will work with the frequency of approx. 24 GHz, which is common for technological applications. When designing a gyrotron, other restricting factors have to be considered, e.g. limitations due to the availability of components, such as the magnet, electron gun and fabricating technology. The most important factor that has to be taken into account at this stage is the magnet. The length

and value of the magnetic field will limit the maximum working frequency, resonator length and radius. In the calculations, it is assumed that magnetic field  $B_0$  is constant in the parallel part  $L_2$  of the cavity. It is desired to choose a magnet and resonator in order to fulfill this requirement as accurately as possible. The distance between the electron gun and the resonator is determined by the magnetic field profile, which is expressed as the  $B_0/B_c$  compression ratio. The magnetic field at the interaction part of the resonator over the magnetic field at the electron gun cathode. All factors mentioned above must be kept in mind when determining the size of the resonator. It is an iterative process. Once a solution is found, it is required to reconsider all the limitations and to repeat the calculation steps, if necessary. In this paper, the gyrotron under consideration will work at the first harmonic. The purpose of this paper is to show how to understand the physical meaning and to solve cold cavity model equations in order for the chosen working mode to be arbitrary to  $TE_{0,1}$ . A higher order mode would require that mode competition analysis [6] need to be performed, but this task is not considered in this paper.

#### 3.1. Cold Cavity Model Input Data

Calculations are performed for the initial frequency of 24 GHz. To estimate the input parameters for the cold cavity model “InputDataEstimation.sm”, the SMATH Studio spreadsheet is used. The following input data were estimated and assumed:

- $freq_{init} = 24$  GHz desired design frequency;
- $m, k$  – chosen azimuthal and radial mode numbers. It is assumed that the harmonic number is equal to 1. In this case  $M = 0, K = 1$  is chosen;
- $R_0$  – resonator radius in the non-tapered part. In this region, electrons interact with the RF field. The radius has to be chosen in such a way that the cut-off frequency is slightly lower than the desired working frequency. The initial guess would be:

$$R_{0init} = \frac{c \cdot V_{m,k}}{2\pi freq_{init}}$$

This value is rounded off reasonably. Here, it would be a tenth of a millimeter, which boils down to  $R_0 = 7,5 \approx R_{0init}$  mm;

- $L = [L_1, L_2, L_3]$  mm – resonator length vector, proposed initial value for:

$$L_2 \approx L_{2init} = 6 \cdot \frac{c}{freq_{init}},$$

which is approximately six wavelengths.  $L_2 = 75$  mm in this case.  $L_1$  and  $L_3$  are supposed to be shorter than  $L_2$ . It is assumed that  $L_1 = L_3 = 30$  mm;

- $\phi = [\phi_1; \phi_2; \phi_3]$  deg – resonator’s taper angle vector.  $\phi_2 = 0$  (always) and  $\phi_1$  and  $\phi_3$  are typically in



the range 0–6 degrees and are described in the literature as “slightly” tapered [7]. A sharp angle would cause a sudden impedance change, which has to be avoided. It is desired to extract maximum radiation from the resonator, and reflections at the output are not desired. It is assumed that  $\phi_1 = 2.3$  and  $\phi_3 = 3.0$  deg;

- $z_{step}$  –  $z$  axis step – 0.05 mm is a good initial choice for good accuracy of the calculation.

### 3.2. Solving the Cold Cavity Model Equation

The following theory is implemented in the “ColdCavityApproachFunction.m” Matlab script. Before it is possible to solve the differential equation, auxiliary variables need to be calculated. The resonator's geometry is described by vector  $R(z)$ . This parameter is the resonator's radius along the longitudinal direction of the gyrotron – Fig. 1. The wall profile includes the tapered part and is calculated using a tangent function and input variables  $L = [L_1, L_2, L_3]$  mm and  $\phi = [\phi_1; \phi_2; \phi_3]$  deg. The characteristic value is the  $K$ -th solution to the  $M$ -th order of the first kind Bessel function derivative  $J'_m(v_{m,k}) = 0$ . In other words, it is the  $x$  axis value of the Bessel first kind  $M$ -th order function derivative at the location where it crosses the  $x$  axis the  $K$ -th time. The characteristic value is presented in Fig. 2 together with the electric field profile that is calculated using the “RadialDistributionOfEMfieldBesselFunction.m” script. The electric field of mode TE has component  $E_z = 0$ , while  $E_r \neq 0$  and  $E_\theta \neq 0$  [8]–[10]. Moreover,  $E_\theta(R_0) = 0$ . This is implied by the physical fact that the electric field in the conductor and at its surface (components parallel to the surface) is equal to 0. This is due to the fact that a perfect conductor has the same potential inside its entire volume and on its surface. The electric field is a property of space that expresses the potential difference between two points within that space. This phenomenon

implies that boundary conditions exist at the resonator's wall, which are applied to the general EM field equations and, therefore, the field profile in the  $r, \theta$  plane may be calculated. For the TE mode, the following time-dependent formulations are obtained:

$$\begin{cases} E_r = -B_0 m \omega R_0 \left(\frac{1}{v_{m,k}}\right)^2 J_m(v_{m,k} \frac{r}{R_0}) \cos(m\theta + k_z z - \omega t) \\ E_\theta = B_0 \omega R_0 \frac{1}{v_{m,k}} J'_m(v_{m,k} \frac{r}{R_0}) \sin(m\theta + k_z z - \omega t) \\ E_z = 0 \end{cases} \quad (5)$$

where:  $B_0$  – magnetic field in the resonator,  $\omega = 2E\pi \cdot freq$  E wave angular frequency,  $k_z$  wave number in the  $z$  direction,  $t$  – time.

The electric field profile in the  $r, \theta$  plane, for mode  $TE_{0,1}$ , is presented in Fig. 2. The TE modes in the cylindrical cavity are linearly polarized, but in the gyrotron resonator, polarization is spinning with time and space ( $z$  axis), while in a cylindrical waveguide mode, it is not rotating in time. Modes with  $m \neq 0$  have two potential polarizations [10] which may be obtained from Eq. (5) by replacing sine with cosine, and cosine with sine, and they will appear as:

$$\begin{cases} E_r = B_0 m \omega R_0 \left(\frac{1}{v_{m,k}}\right)^2 J_m(v_{m,k} \frac{r}{R_0}) \sin(m\theta + k_z z - \omega t) \\ E_\theta = B_0 \omega R_0 \frac{1}{v_{m,k}} J'_m(v_{m,k} \frac{r}{R_0}) \cos(m\theta + k_z z - \omega t) \\ E_z = 0 \end{cases} \quad (6)$$

The solution of the cold cavity task consists of two steps. It is first required to choose the sweep range of the optimization variables  $freq$  (E field frequency) and  $Q_{diff}$  (cavity diffractive quality). The differential Eq. (2) has to be then solved iteratively for a different  $freq$  and  $Q_{diff}$  pair to find the values that will result in the minimal Eq. (4) value. This becomes a typical optimization problem. To find the optimal solution, the frequency and quality search space

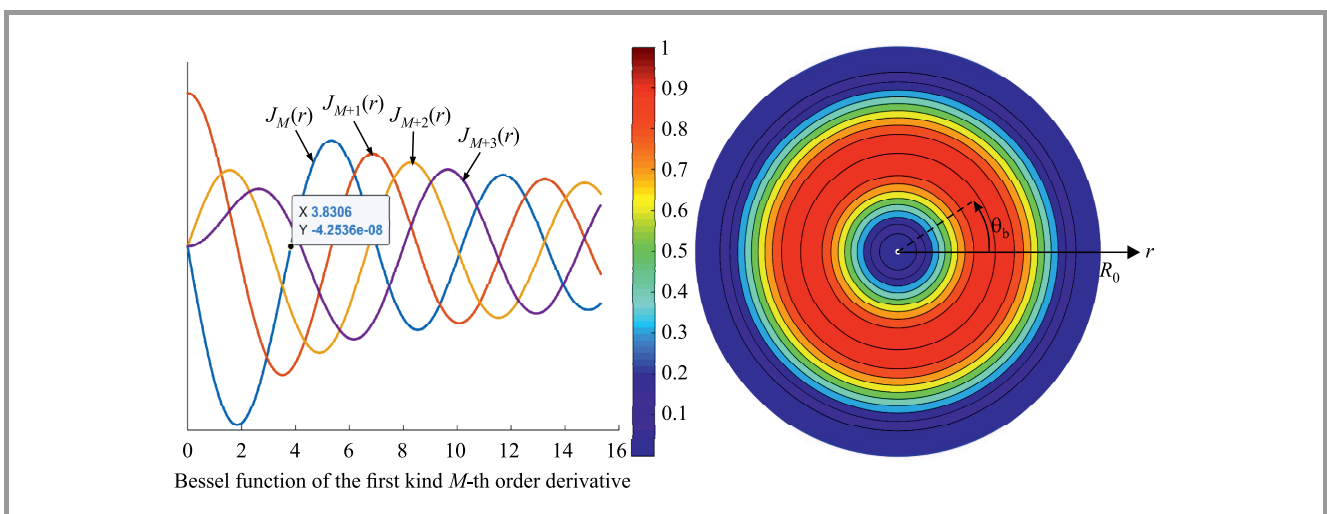


Fig. 2. Bessel function derivative and electric field in the resonator's cross-section for mode  $TE_{01}$  at  $z = 0$  and  $t = 0$ . (For color pictures see the digital version of the paper.)

must be defined. The frequency search range proposed in this paper [11] is:

$$\begin{cases} freq_{min} = \frac{c}{2\pi} \sqrt{\left(\frac{v_{m,k}}{R_0}\right)^2 + \left(\frac{\pi}{L_1+L_2+L_3}\right)^2} \\ freq_{max} = \frac{c}{2\pi} \sqrt{\left(\frac{v_{m,k}}{R_0}\right)^2 + \left(\frac{\pi}{L_2}\right)^2} \end{cases}, \quad (7)$$

where:  $c$  – light velocity,  $v_{m,k}$  – characteristic value for mode  $TE_{m,k}$ .

The proposed search range for the resonator's quality factor [12] is:

$$\begin{cases} Q_{diff_{min}} = 4\pi \left(\frac{L_2}{\lambda}\right)^2 \\ Q_{diff_{max}} = 4\pi \left(\frac{L_1+L_2+L_3}{\lambda}\right)^2 \cdot 4 \end{cases}, \quad (8)$$

where:  $\lambda = \frac{c}{0.5 \cdot (freq_{min} + freq_{max})}$ .

The proposed range for frequency is found in the literature [11], but the range for the quality factor's maximum values are the author's ideas and are based on the literature and observation of the RF field profile function in the domain of the  $freq$ ,  $Q_{diff}$  sweep. The formulation for the  $Q_{min}$  value found in the literature is correct [4], but the  $Q_{max}$  value cannot be estimated from the maximum resonator length, because it appears to be too narrow and does not always include the final solution within the optimization range.

One way to determine whether the search range was properly chosen is to check if the best solution does not lie at the edge of the search space. If it does, the optimization variable range needs to be expanded in this direction.

### 3.3. Solving the Equation System

To solve Eq. (2), the second order problem is rewritten as a first order equation system. To do this, new variables  $y_1 = f$  and  $y_2 = \frac{df}{dz}$  are introduced. It is then possible to deduce that  $\frac{dy_2}{dz} = \frac{d^2f}{dz^2}$ , but from Eq. 2 it is known that  $\frac{d^2f}{dz^2} = -k_z^2(\omega, z)f$ , and, therefore, the computationally friendly first order form is:

$$\begin{cases} \frac{dy_1}{dz} = y_2 \\ \frac{dy_2}{dz} = -k_z^2(\omega, z)y_1 \end{cases}, \quad (9)$$

where  $y_1$  and  $y_2$  are two variables in the equation system.

The first order differential equation system may be solved using the Runge-Kutta routine [7] implemented in the ode45 algorithm. From the Matlab manual, it is known that to run a solver, the following representation of the problem must be presented as:  $[z, f] = \text{ode45}(\text{odefun}(z, f), z_{span}, f_0)$ , where:

- `odefun` – defines the function that returns the first derivative  $\frac{df}{dz}$ . For the equation system, the function receives  $f$  as a vector and returns a vector

that contains one derivative for each equation in the system;

- $z_{span}$  – the vector that defines the  $z$  values for the algorithm;
- $f_0$  – the initial value for function  $f$ . It is a vector containing the starting values.

In the ode45 solver manual, there is a sample solution to the problem that is very similar to this case. The `odefun` for the Matlab solver is implemented in the “`OdeEqColdCavityField`” function as part of the “`EqColdCavityField.m`” script. Technical realization of the second-to-first order differential equation reduction requires function values  $y_1$  and  $y_2$  to be passed into the `odefun` at each iteration. It might be confusing, but  $y_1 = f$  and  $y_2 = \frac{df}{dz}$ . The return values are the first derivatives of  $y_1$  and  $y_2$  calculated inside the ode function using the following formulation:

$$\begin{cases} \frac{df}{dz} = \frac{d^2y}{dz^2} \\ \frac{d^2f}{dz^2} = -k_z^2(\omega, z) \frac{dy}{dz} \end{cases}. \quad (10)$$

It might be confusing, but in the case under consideration, the return values of the `odefun` are in fact  $\frac{y_1}{dz} = \frac{df}{dz}$  and  $\frac{y_2}{dz} = \frac{d^2f}{dz^2}$ . To solve the differential equation system, the initial conditions must be supplied. In this model, the following equations define the initial conditions [13] for the ode45 solver:

$$\begin{cases} f_{init} = e^{ik_z} \\ \frac{df_{init}}{dz} = e^{ik_z} \cdot f_{init} \end{cases}. \quad (11)$$

### 3.4. Solving the Optimization Task

It is necessary to consider if the optimized function is monotonous. If it has one minimum, then the Matlab “`patternsearch`” function can be used. The pattern search algorithm group is capable of finding the local minimum, but it does not guarantee that a global solution will be found, as the algorithm requires a starting point [14]. Success in finding the global minimum depends on the assumed starting point, unless the function has one minimum. In the considered case, there is only one minimum (Fig. 3), so it is possible to simply start searching from the middle of the assumed range of  $\omega$  and  $Q$ , as there is only one minimal solution within the entire search range.

For each pair of the  $\omega$  and  $Q$ , the RF field profile along the  $z$  axis is found using Eq. (2). The boundary conditions on the left- and right-hand side of the resonator are then checked – Eq. (4). The best solution will have a minimal value of  $|R|$  for  $\omega_{optimal}$  and  $Q_{optimal}$ . This is done using the “`EqColdCavityField.m`” script. In this way, the optimal solution for the chosen  $TE$  mode and fixed dimension is found.

To find the best geometry for the resonator, a parameter sweep is proposed. The 7th parameters have an influence

## 4. Results

As a result of the calculations, the following output variables are obtained:

- $f(z)$  – RF field profile along the  $z$  axis – Fig. 4,
- $f_{optimal} = \frac{\omega_{optimal}}{2\pi}$  – optimal value of frequency,
- $Q_{optimal}$  – optimal value for the diffractive quality factor.

for certain resonator:  $L = [L_1, L_2, L_3]$  mm,  $\phi = [\phi_1; \phi_2; \phi_3]$  deg and  $R_0$  mm.

The optimal value is the lowest  $|R|$  value, which is equivalent to the minimal reflection at the output taper.

## 5. Conclusion

In this work, the first step of the gyrotron resonator design process is presented. Due to the fact that the device has so many variables and factors that need to be considered, it is not obvious how to start the calculations. This work presents which variables have to be assumed and what initial values or value ranges may be relied upon to commence the design process. It is worth noting that, if a frequency below cutoff is chosen, the mode will not propagate, which will cause the code to crash, as  $k_z$  will be imaginary. It is also worth keeping in mind that choosing a low value of  $m$  and  $k$  will cause the Brillouin angle to be low, and therefore microwave power will have to be extracted in the direction parallel to the  $z$  axis. If perpendicular power output is desired, it is advised to use a high order mode so that the launcher component in the form of an oversize waveguide will have a reasonable length. It is possible to use GPU (graphic card processor) computing for this problem. The reason for this is that it may be turned into a parallel algorithm, due to fact that every solution is independent from the other. The main problem, causing implementation to be time consuming is, the requirement to implement the ode45 solver in the GPU. This could be the next step in the development of this code. However, the presented model is solved efficiently using CPU, and this was the main reason for choosing this approach.

## Supplementary Materials

Supplementary materials: source code and animations may be downloaded from: <http://sci.vberrry.net>.

## References

- [1] M. I. Airila, O. Dumbrajs, A. Reinfelds, and U. Strautins "Nonstationary oscillations in gyrotrons," *Phys. of Plasmas*, vol. 8, no. 10, pp. 4608–4612, 2001 (DOI: 10.1063/1.1402173).
- [2] J. Cepitis, O. Dumbrajs, H. Kalis, A. Reinfelds, and U. Strautins, "Analysis of equations arising in gyrotron theory", *Nonlinear Analysis: Modeling and Control*, vol. 17, no. 2, pp. 139–152, 2012 (DOI: 10.15388/NA.17.2.14064).

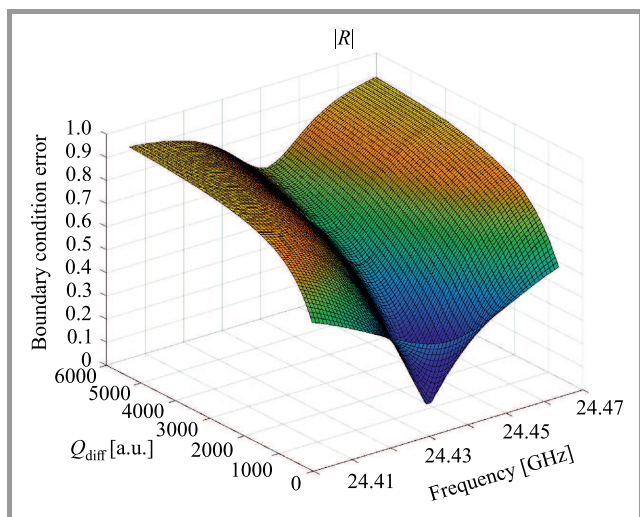


Fig. 3.  $|R| = f(\omega, Q)$  boundary condition minimized function.

on the RF field, which are  $L = [L_1, L_2, L_3]$ ,  $\phi = [\phi_1; \phi_2; \phi_3]$  and  $R_0$ . Two main factors influence the solution –  $R_0$  and  $L_2$ .  $R_0$  is fixed and estimated from the cutoff frequency dependency for a certain mode (see “SMath studio” sheet). Therefore,  $L_2$  is a geometrical dimension that is the best candidate to be optimized. For each value of  $L_2$ , it is required to repeat the procedure of  $\omega$  and  $Q$  optimization. All values of  $|R|$  for the different dimension have to be collected and compared in order to find the optimal  $L_2$  value. This step is implemented in the “RunFindBasicSolution.m” script. Because the cold cavity model does not consider the electron current flow (and other factors), it is important to know that the final solution might be slightly different from the one chosen to be the best. Therefore, it is actually advised to consider 10 or 20 of the best solutions found by this method and to investigate them using a full-wave software package, or a more accurate but more time-consuming model.

Intermediate variables are not described here due to the fact that formulations may be found in the code. Moreover, they are self-explanatory.

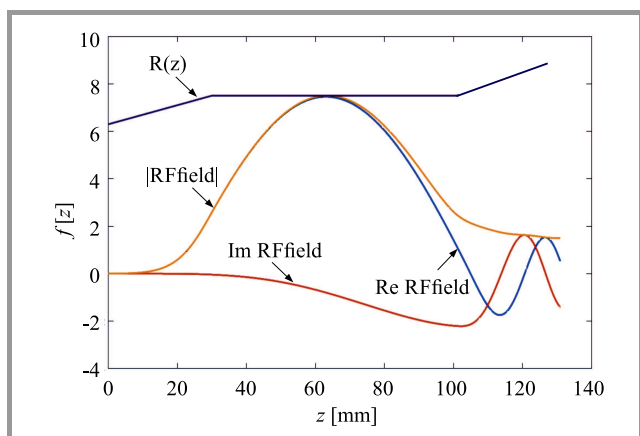


Fig. 4. Electric field intensity longitudinal profile  $f(z)$ .

[3] N. S. Ginzburg, N. A. Zavolskii, G. S. Husinovich, and A. S. Sergeev, "Onset of self-oscillations in electronic microwave oscillators with diffraction radiation output", *Radiofizika*, vol. 29, no. 1, pp. 106–114, 1986 (ISSN 0021-3462) [in Russian].

[4] G. S. Nusinovich, *Introduction to the Physics of Gyrotrons*. Johns Hopkins University Press, 2004 (ISBN: 9780801879210).

[5] L. Zhang, "Studying and Comparing Numerical Methods for Ordinary Differential Equations", 2015. [Online]. Available: <http://rgdoi.net/10.13140/RG.2.2.33806.56645>

[6] O. Dumbrajs and G. S. Nusinovich, "Cold-cavity and self-consistent approaches in the theory of mode competition in gyrotrons", *IEEE Trans. on Plasma Sci.*, vol. 20, no. 3, pp. 133–138, 1992 (DOI: 10.1109/27.142812).

[7] E. Borie, "Review of Gyrotron Theory", Karlsruhe Institut für Technologie, Karlsruhe, 1991 [Online]. Available: <https://publikationen.bibliothek.kit.edu/270031114/3813439> (DOI: 10.5445/IR/270031114).

[8] L. F. Chen, C. K. Ong, C. P. Neo, V. V. Varadan, and V. K. Varadan, *Microwave Electronics: Measurement and Materials Characterization*. Wiley, 2004 (ISBN: 9780470844922).

[9] C. A. Balanis and E. Holzman, "Circular Waveguides", in *Encyclopedia of RF and Microwave Engineering*. Wiley, 2005, p. 75 (DOI: 10.1002/0471654507).

[10] P. Tenenbaum, "Fields in Waveguides – A Guide for Pedestrians", 2003 [Online]. Available: [https://www.desy.de/~njwalker/uspas/coursemat/notes/unit\\_2\\_notes.pdf](https://www.desy.de/~njwalker/uspas/coursemat/notes/unit_2_notes.pdf)

[11] D. M. Pozar, *Microwave Engineering*, 4th ed. Hoboken, NJ: Wiley, 2012 (ISBN: 9780470631553).

[12] H. Saito, K. Kreisler, B. G. Danly, T. M. Tran, and R. J. Temkin, "A gyrotron with a minimum  $Q$  cavity", *Int. J. of Electron.*, vol. 61, no. 6, pp. 757–770, 1986 (DOI: 10.1080/00207218608920921).

[13] C. Edgecombe, *Gyrotron Oscillators*. London: CRC Press, 1993 (ISBN: 978-0748400195).

[14] D. Xue and Y. Chen, *Scientific Computing with MATLAB*. Boca Raton: Chapman and Hall/CRC, 2016 (DOI: 10.1201/9781315367859).



**Kacper Nowak** received his Ph.D. from Wrocław University of Science and Technology in 2012. He is currently an Assistant Professor at the Electronics and Telecommunications Department, Faculty of Electronics, Wrocław University of Science and Technology. His research interests include: terahertz spectroscopy, gyrotron

technology, industrial automation, networking and programming.

 <https://orcid.org/0000-0002-5980-8237>

E-mail: [kacper.nowak@pwr.edu.pl](mailto:kacper.nowak@pwr.edu.pl)

Faculty of Electronic


Wrocław University of Science and Technology

Wybrzeże Wyspiańskiego 27

50-370 Wrocław, Poland



**Olgierd Dumbrajs** received the M.Sc. degree in Physics from Latvian State University, Riga, in 1965, and the Ph.D. degree in Physics from Moscow State University, Moscow, Russia, in 1971. He was a Research Worker with the Joint Institute for Nuclear Research, Dubna, Russia, from 1971 to 1977, the University of Helsinki, Helsinki, Finland, from 1977 to 1978, and the Institutes for Nuclear Research in Zürich, Switzerland, Geneva, Switzerland, and Paris, France, from 1978 to 1979. He was a Research Professor with the University of Aarhus, Aarhus, Denmark, from 1978 to 1979. He was a Research Worker with the Karlsruhe Institute of Technology, Karlsruhe, Germany, from 1979 to 1983. He was a Group Leader with the Technische Universität Hamburg-Harburg, Harburg, Germany, from 1983 to 1992. He was a Special Research Worker with the Academy of Finland, Helsinki, and the Helsinki University of Technology, Espoo, Finland, from 1992 to 2008. He has been a Leading Research Scientist with the Institute of Solid State Physics, University of Latvia, since 2006.

 <https://orcid.org/0000-0003-2938-1196>

E-mail: [olgertsd@cfi.lu.lv](mailto:olgertsd@cfi.lu.lv)

Institute of Solid State Physics  
University of Latvia  
Kengaraga Street 8  
LV-1063 Riga, Latvia



# Information for Authors

*Journal of Telecommunications and Information Technology (JTIT)* is published quarterly. It comprises original contributions, dealing with a wide range of topics related to telecommunications and information technology. **All papers are subject to peer review.** Topics presented in the JTIT report primary and/or experimental research results, which advance the base of scientific and technological knowledge about telecommunications and information technology.

JTIT is dedicated to publishing research results which advance the level of current research or add to the understanding of problems related to modulation and signal design, wireless communications, optical communications and photonic systems, voice communications devices, image and signal processing, transmission systems, network architecture, coding and communication theory, as well as information technology.

Suitable research-related papers should hold the potential to advance the technological base of telecommunications and information technology. Tutorial and review papers are published only by invitation.

**Manuscript.** TEX and LATEX are preferable, standard Microsoft Word format (.doc) is acceptable. The authors JTIT LATEX style file is available:

<https://www.itl.waw.pl/en/jtit-for-authors>

Papers published should contain up to 10 printed pages in LATEX authors style (Word processor one printed page corresponds approximately to 6000 characters).

The manuscript should include an abstract about 150–200 words long and the relevant keywords. The abstract should contain statement of the problem, assumptions and methodology, results and conclusion or discussion on the importance of the results. Abstracts must not include mathematical expressions or bibliographic references.

Keywords should not repeat the title of the manuscript. About four keywords or phrases in alphabetical order should be used, separated by commas.

The original files accompanied with pdf file should be submitted by e-mail: [redakcja@itl.waw.pl](mailto:redakcja@itl.waw.pl)

**Figures, tables and photographs.** Original figures should be submitted. Drawings in Corel Draw and PostScript formats are preferred. Figure captions should be placed below the figures and can not be included as a part of the figure. Each figure should be submitted as a separated graphic file, in .cdr, .eps, .ps, .png or .tif format. Tables and figures should be numbered consecutively with Arabic numerals.

Each photograph with minimum 300 dpi resolution should be delivered in electronic formats (TIFF, JPG or PNG) as a separated file.

**References.** All references should be marked in the text by Arabic numerals in square brackets and listed at the end of the paper in order of their appearance in the text, including exclusively publications cited inside. Samples of correct formats for various types of references are presented below:

- [1] Y. Namiyama, Relationship between nonlinear effective area and mode field diameter for dispersion shifted fibres, *Electron. Lett.*, vol. 30, no. 3, pp. 262–264, 1994.
- [2] C. Kittel, *Introduction to Solid State Physics*. New York: Wiley, 1986.
- [3] S. Demri and E. Orłowska, Informational representability: Abstract models versus concrete models, in *Fuzzy Sets, Logics and Knowledge-Based Reasoning*, D. Dubois and H. Prade, Eds. Dordrecht: Kluwer, 1999, pp. 301–314

**Biographies and photographs of authors.** A brief professional authors biography of up to 200 words and a photo of each author should be included with the manuscript.

**Galley proofs.** Authors should return proofs as a list of corrections as soon as possible. In other cases, the article will be proof-read against manuscript by the editor and printed without the author's corrections. Remarks to the errata should be provided within one week after receiving the offprint.

**Copyright.** Manuscript submitted to JTIT should not be published or simultaneously submitted for publication elsewhere. By submitting a manuscript, the author(s) agree to automatically transfer the copyright for their article to the publisher, if and when the article is accepted for publication. The copyright comprises the exclusive rights to reproduce and distribute the article, including reprints and all translation rights. No part of the present JTIT should not be reproduced in any form nor transmitted or translated into a machine language without prior written consent of the publisher.

For copyright form see:

<https://www.itl.waw.pl/en/jtit-for-authors>

---

*Journal of Telecommunications and Information Technology* has entered into an electronic licencing relationship with EBSCO Publishing, the worlds most prolific aggregator of full text journals, magazines and other sources. The text of *Journal of Telecommunications and Information Technology* can be found on EBSCO Publishings databases. For more information on EBSCO Publishing, please visit [www.epnet.com](http://www.epnet.com).

*(Contents Continued from Front Cover)*

**Orthogonal Harmonic Signals of the Generalized Class**

*V. Balashov, V. Oreshkov, I. Barba, and O. Iegupova*

*Paper*

64

**Optimization of Gyrotron Resonator's Dimensions**

*K. Nowak and O. Dumbrajs*

*Paper*

71

**Editorial Office**

National Institute  
of Telecommunications  
Szachowa st 1  
04-894 Warsaw, Poland

tel. +48 22 512 81 83  
fax: +48 22 512 84 00  
e-mail: [redakcja@itl.waw.pl](mailto:redakcja@itl.waw.pl)  
<http://www.nit.eu>